UNIVERSITÉ DE NANTES
FACULTÉ DES SCIENCES ET DES TECHNIQUES

ÉCOLE DOCTORALE MOLÉCULES, MATIÈRES ET MATÉRIAUX EN PAYS DE LOIRE

Année 201 3

N° attribué par la bibliothèque

Effets de la perte d'énergie partonique sur la suppression nucléaire de quarkonium

THÈSE DE DOCTORAT
Discipline : Physique Nucléaire
Spécialité : Physique des particules -Théorie

Présentée
et soutenue publiquement par

Maryam RUSTAMOVA

Le 22 Octobre 2013, devant le jury ci-dessous

Président et rapporteur	M. Patrick Aurenche , Directeur de Recherche CNRS, LAPTH Annecy
Rapporteur	M. Paul Hoyer, Professeur, Université d'Helsinki (Finlande)
Examinateurs	M. François Arleo, Chargé de Recherche CNRS , Ecole Polytechnique Palaiseau
	M . Gines Martinez, Directeur de Recherche CNRS, Subatech Nantes
	M. Stephane Peigné , Chargé de Recherche CNRS, Subatech Nantes

Directeur de thèse : M . Gines Martinez

Co-Directeur de thèse:M . Stephane Peigné

Contents

Introduction

The current understanding of elementary particles and their interactions is described within the Standard Model of Particle Physics. The elementary constituents of matter consist of six types (flavors) of quark (d, u, s, c, b, t) and six leptons consisting of the electron, the muon, and the tau, each of them accompanied by a neutrino of the corresponding flavor. Quarks and leptons are organized in three "generations" or "families" based on their masses, and are all spin-$\frac{1}{2}$ particles. Spin-$\frac{1}{2}$ particles interact with each other via the mediation of gauge bosons, which are spin-1 particles. For each quark and lepton there is a corresponding antiquark and antilepton.

The Standard Model describes three out of the four forces existing in Nature, namely the electromagnetic, weak and strong interactions. The fourth force, gravity, is described by general relativity, and is too weak to be of any consequence at the experimentally accessible energies that are relevant to Particle Physics. The Standard Model is a gauge field theory based on the group $SU(2)_L \times U(1)_Y \times SU(3)_C$. The electroweak theory $SU(2)_L \times U(1)_Y$, proposed by Glashow, Salam and Weinberg, describes the weak and electromagnetic interactions. $SU(2)_L$ stands for the non-abelian, weak isospin symmetry, the index L stating that the corresponding gauge fields (the $W^{\pm}$ and Z^0) only couple to left-handed fermions. $U(1)_Y$ denotes the abelian hypercharge symmetry, acting on left-handed and right-handed fermions differently. Finally, $SU(3)_C$ is the non-abelian *color* symmetry group of Quantum Chromodynamics (QCD) describing the strong force. The strong interaction is mediated by eight gluons – the gauge bosons of $SU(3)_C$ – and acts on quarks and gluons.

In the past decades, the Standard Model has been verified with great precision by numerous experiments. It predicted the existence of the W and Z bosons, the gluon, and the charm and top quarks before their experimental observation. Quantum Electrodynamics in particular is the most precisely tested theory in Physics. A crucial element of the Standard Model is the Higgs Boson. It is essential to explain the origin of the mass of elementary particles, as a result of the spontaneous breaking of the electroweak symmetry. The Large Hadron Collider (LHC) at CERN has recently produced some evidence for a Higgs-like particle with a mass of order $126\,\mathrm{GeV/c^2}$. However, there are phenomena which cannot be explained within the Standard Model, such as neutrino oscillations, the phenomenon of dark matter, and the baryon asymmetry of the Universe.

Although it is now clear that QCD is the correct theory of the strong interaction, it should be stressed that QCD is tested to an accuracy which is not as good as for the electroweak interaction. Experimental data on hadron production rates are less precise than on electroweak processes, and theoretical QCD calculations have large uncertainties, due to the fact that at present energies the QCD coupling α_s is not very small compared to unity, and to the fact that confinement (or more specifically the hadronization process) is not understood yet. However, improving the accuracy of QCD is crucial. It is important for our understanding of the fundamental laws of Nature, but also to control the QCD backgrounds which appear in electroweak phenomena (e.g., Higgs production).

QCD is characterized by two essential features: *asymptotic freedom* and *confinement*. Asymptotic freedom is the fact that at high energy quarks within a hadron behave like free particles, which is revealed by deep-inelastic experiments. It can be derived from first principles of QCD. Confinement means that quarks and gluons cannot be isolated in normal conditions: they always appear as constituents of color neutral hadrons.

Shortly after the discovery of asymptotic freedom, it was realized that common nuclear matter consisting of protons and neutrons might be transformed at high temperature and density into a deconfined phase, called Quark Gluon Plasma (QGP). In the 1990s, the drastic change of the number of degrees of freedom at a temperature around 175 MeV was predicted by lattice QCD. It is believed that the QGP was the state of the Universe during the first hundred microseconds after the Big Bang, and that it currently exists in the core of neutron stars. The QGP can be created in the laboratory by colliding two large nuclei at a sufficiently high collision energy. After the beginning of the Relativistic Heavy Ion Collider (RHIC) program during the summer 2000, more and more evidence hinted to the discovery of the QGP.

Knowing more about the precise nature of the QGP (viscosity, entropy...) would yield crucial information on QCD itself. At high temperature T, we believe that the QGP can be addressed perturbatively, since we expect the strong coupling $\sim \alpha_s(T)$ to be small, thanks to asymptotic freedom. Quite recently, using intuition from a certain theoretical framework (AdS/CFT), it was argued that the QGP might be strongly coupled, showing that QGP studies trigger many new theoretical developments.

In heavy-ion (A-A) collisions, the QGP can be observed only via indirect signals, simply because only colorless hadrons are detected. One of the prominent QGP signals is *jet-quenching*. In A-A collisions the hard scatterings of the incoming quarks and gluons create energetic partons with large transverse momentum. These fast partons fragment into a bunch of collimated hadrons forming what is called a jet. Before fragmenting into hadrons, an energetic parton has to travel through the hot medium formed after the collision. The latter induces some *parton energy loss* ΔE, which leads to a modification of the jet or hadron production rate at a given p_T. One of the most exciting observations at RHIC was the strong suppression of high p_T hadrons in central gold-gold collisions compared with the scaled results from p-p collisions. The observed suppression agrees qualitatively with the expectation of parton energy loss through the QGP.

Nuclear attenuation is not specific to A-A collisions where we expect the formation of a QGP. Spectacular nuclear suppression effects are also seen in p-A collisions, where a priori no QGP is created. Studying nuclear suppression in p-A collisions, i.e., in standard cold nuclear matter – a better controlled medium –, is a prerequisite to fully understand the phenomenon of jet-quenching in A-A collisions.

Nuclear suppression in p-A collisions is observed for various observables and in various kinematical domains, in particular in domains where perturbative QCD can be used. During my work I focused on J/ψ nuclear suppression in p-A collisions. Various effects have been proposed to explain J/ψ nuclear suppression (shadowing, bound state nuclear absorption, comover rescattering, parton energy loss) but with no consensus yet. The goal of my study is to show that parton energy loss, *when properly evaluated*, might be the main effect responsible for J/ψ nuclear suppression in p-A collisions. There are indeed confusing results in the literature concerning the parametric dependence of ΔE, and it is important to revisit the effect of energy loss on nuclear suppression. I developed a phenomenological model to predict the kinematical (x_F and p_T) dependence of quarkonium nuclear suppression arising from parton energy loss.

The thesis is organized as follows. Chapter 1 presents a very brief introduction on Quantum Chromodynamics. In Chapter 2 the currently used J/ψ production models (CEM, COM, CSM,...) are discussed. Chapter 3 is devoted to some experimental facts on J/ψ suppression in cold nuclear matter, as well as on various cold nuclear effects (nuclear absorption, shadowing, comover rescattering, relative momentum broadening of the $c\bar{c}$ pair, parton energy loss), which have been proposed as possible explanations for J/ψ suppression. Chapter 4 reviews the parametric dependence of radiative parton energy loss in various kinematical situations, comparing the cases of parton energy loss induced in small and large angle scattering. In Chapter 5, we discuss a phenomenological model, where parton energy loss is used as the main effect responsible for J/ψ suppression. Both the rapidity (or x_F) and p_T dependence of the suppression is addressed. The comparison between the model predictions and the existing data, as well as predictions for LHC are presented.

CHAPTER 1

Quantum Chromodynamics: Basic Notions

Contents

1.1 A very brief introduction to QCD

During the 1950s and 1960s physicists were searching for alternative approaches in quantum field theory (QFT). In the 50's Yang and Mills introduced the idea of non-abelian gauge invariance. They considered the isospin $SU(2)$ symmetry in $n - p$ space (introduced in 1932 by Heisenberg [1]) which they generalized to local isotopic transformations. This lead to the formulation of the isotopic gauge invariance [2].

In 1964, Gell-Mann and Zweig independently from each other, assumed the existence of three "quark" flavours u, d and s, which are the elementary "bricks" that build the hadron. The triplet $Q = (u, d, s)$ was assumed to belong to the fundamental representation of $SU(3)_{flavor}$. It was then possible to explain the presence of hadron multiplets in the hadron spectrum as representants of different representations of global $SU(3)$. Later in the sixties, the idea of color quantum number arised after the observation of the Δ^{++}. It was interpreted as a uuu bound state, which in the case where the three u quarks have aligned spins, must be totally symmetric under the exchange of two quarks . This contradicts the Pauli principle. The problem was resolved by proposing the additional $SU(3)$ gauge degree of freedom of a quark [3], which was later called a color charge. It was established that quarks interact with each other via strong force by exchanging gluons.

This was followed by the parton model proposed by Bjorken, which showed a good agreement with the SLAC experiment in 1969. All the mentioned above discoveries led to the birth of the Quantum Chromodynamics (QCD) in the early 70's.

Similarly to the "isospin" space of Yang-Mills, QCD was based on gauge symmetry in color space. The gauge invariant QCD Lagrangian is :

$$L_{QCD} = \bar{\psi}_i(i(\gamma^\mu D_\mu)_{ij} - m\delta_{ij})\psi_j - \frac{1}{4}G^a_{\mu\nu}G^{\mu\nu}_a \tag{1.1}$$

where $\psi_i(x)$ is the quark field, belonging to the fundamental representation of $SU(3)_{color}$, $G^a_{\mu\nu}$ represents the gluon field strength tensor. It is defined as

$$G^a_{\mu\nu} = \partial_\mu G^a_\nu - \partial_\nu G^a_\mu - gf^{abc}G^b_\mu G^c_\nu \tag{1.2}$$

where G^a_μ is the gluon field belonging to the adjoint representation of $SU(3)_{color}$, f^{abc} are the structure constants of $SU(3)$, and g is the coupling constant of the theory, which determines the strength of interaction. In QCD one also defines the dimensionless coupling constant $\alpha_s = \frac{g^2}{4\pi}$.

QCD is a very rich theory with many aspects but with two main properties:

- Confinement: The colored particles (such as quarks) cannot be isolated and therefore cannot be directly observed. This phenomenon is called color confinement. To illustrate it one can look at the interaction potential of a quarkonium state (colorless meson whose constituents are a quark and its anti-quark) and its dependence on the distance between the heavy quarks. The heavy quark potential is parametrized as,

$$V_{Q\bar{Q}} \sim -\frac{4\alpha_s}{3r} + Kr \tag{1.3}$$

The first term of the potential is the Coulomb term which dominates at short distance. The second term is linear (see Fig 1.1). Since the potential is linear at large distances the force between quarks is constant (the force is being the derivative of the potential).

One can compare to the case of electric charges; when two electric charges became distant, the force between them diminishes very quickly, as $1/r^2$, and the charges can be easily separated. However if we try to separate two *color* charges, gluon fields form a narrow string which tends to keep them with a constant force, leading to increasing potential energy. As a consequence it is more favorable energetically for a new quark anti-quark pair to appear than to allow the string to extend further. As a result, in particle accelarators we never observe quarks separately; what physicists actually see are "jets" of many colorless particles arising from hadronization of the many $q\bar{q}$ pairs created during the "string breaking" stage of the process.

Confinement is not fully understood from the first principles, i.e., from the structure of the QCD Lagrangian.

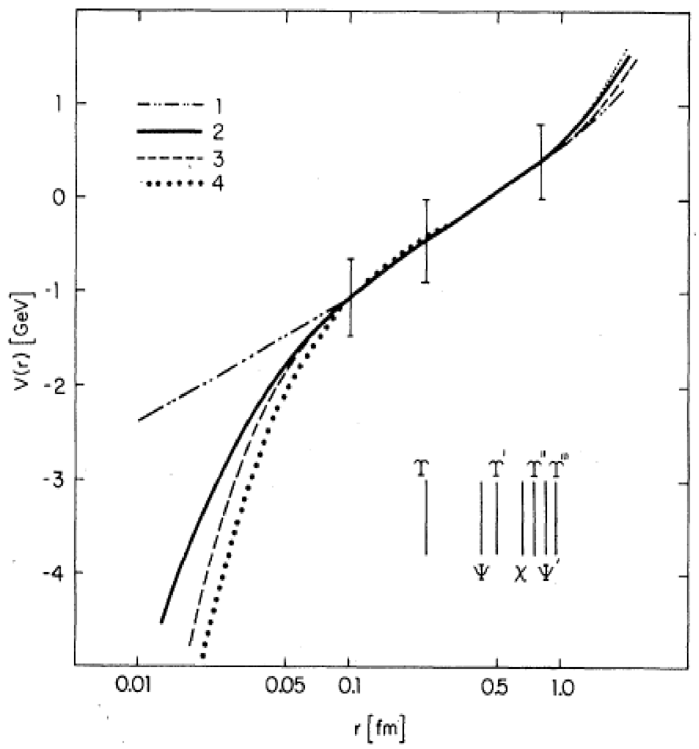

Figure 1.1: Heavy quark potential of the bound state [4]

- Asymptotic freedom: as energy gets higher the interaction coupling α_s becomes weaker. It can be derived by calculating the QCD beta function which describes the variation of the coupling constant with the energy scale Q. The beta function in QCD is negative,

$$\beta(\alpha_s) \equiv \frac{d\alpha_s}{d\log Q^2} = -\frac{b}{4\pi}\alpha_s^2 < 0 \tag{1.4}$$

where $b = \frac{11}{3}N - \frac{2}{3}n_f$ (With N the number of colors and n_f the number of quarks flavors). Solving the differential equation (1.4), we obtain the following expression for α_s:

$$\alpha_s(Q^2) = \frac{\alpha_s(Q_0^2)}{1+\alpha_s(Q_0^2)\frac{b}{4\pi}\log(\frac{Q^2}{Q_0^2})} = \frac{4\pi}{b\log(\frac{Q^2}{\Lambda_{IR}^2})} \tag{1.5}$$

where

$$\Lambda_{IR} = Q_0^2 exp[-\frac{4\pi}{b\alpha_s(Q_0^2)}] \tag{1.6}$$

The experimental data gives $\Lambda_{IR} \simeq 200$ MeV. Since (1.5) relies on (1.4) which was derived perturbatively (i.e. assuming $\alpha_s << 1$), only large values of Q must be used in (1.6), for instance $Q^2 \gg 1$ GeV^2.

Equation (1.5) illustrates the crucial property of asymptotic freedom in QCD: when Q increases the coupling α_s decreases (as $1/\ln(Q^2)$) and tends to zero when $Q \to \infty$. This behaviour can arise only in non-abelian gauge theories, where the β-function can be negative. In QED, $\beta_{QED} > 0$ and an opposite behaviour is obtained.

The different behaviour of the coupling in QED and QCD is shown in Fig 1.2. In spite of the fact that α_s at low Q *might* be of order 1 [1], thanks to asymptotic freedom one can apply perturbation theory at high enough energy.

Finally, let us stress that asymptotic freedom does not mean that the strong force becomes weak at high Q. This can be seen from (1.3). At large energies (or equivalently at small distances), the first term of this potential is dominant, and the associated force is $\propto 1/r^2$, and thus very large.

[1] Some studies indicate that the effective strong coupling might remain smaller than 1 even in the infrared domain [5].

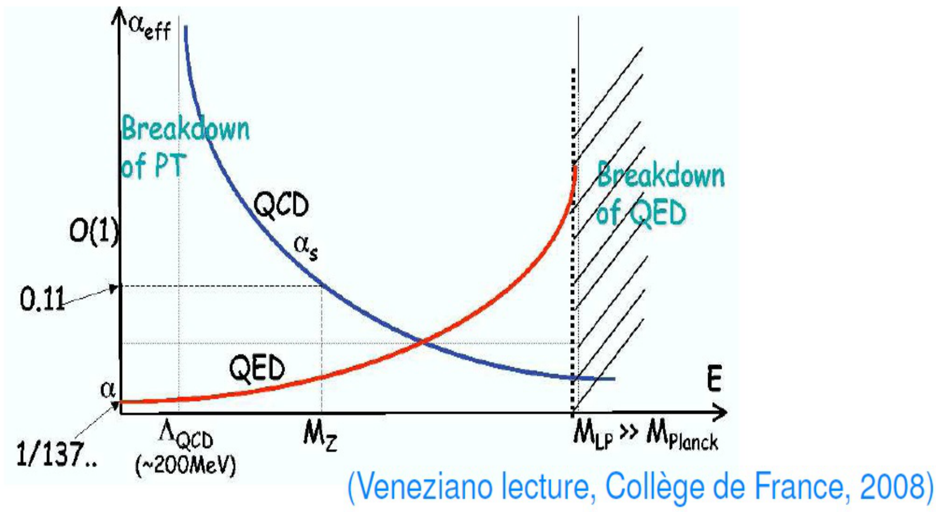

Figure 1.2: Evolution of the coupling constant with energy: QED vs QCD

1.2 QCD factorization

1.2.1 Parton Model

The main assumption of the parton model is to neglect the interaction between partons. A hadron is thus considered like a loosely bound system of partons.

Let us consider Deep Inelastic Scattering (DIS) in the parton model approximation (Fig.1.3). As one can see from the Figure, the process consists in the interaction of an electron with a proton. Since we imgaine the reaction to happen at very high energies, we will ignore all masses.

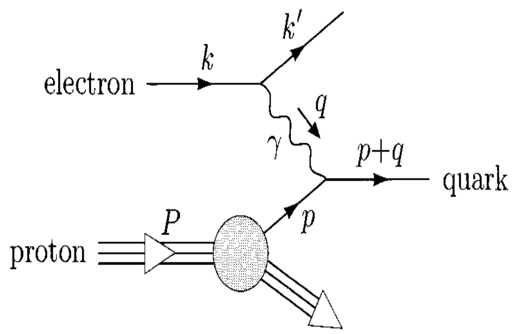

Figure 1.3: Deep Inelastic Scattering in the parton model.

The cross section of the $e^-q \to e^-q$ process, which can be found in most of textbooks [6] is:

$$\frac{d\sigma}{d\hat{t}} = \frac{2\pi\alpha^2 Q_i^2}{\hat{s}^2}\left(\frac{\hat{s}^2 + (\hat{s}+\hat{t})^2}{\hat{t}^2}\right) \tag{1.7}$$

Here $\hat{s}$ and $\hat{t}$ are Mandelstam variables, that have to be related to the quantities measured in the experiment, Q_i is the electric charge of the quark in units of $|e|$. By definition, $\hat{t} = (k' - k)^2 = q^2$. This quantity can be extracted by measuring the final momentum and energy of the electron. Usually one defines $Q^2 \equiv -q^2$. Then the invariant $\hat{t}$ is simply $-Q^2$.

To relate $\hat{s}$ to the experimental observables one defines a new variable ξ. If the collision is viewed in the electron-proton center of mass frame, and we visualize the proton as a loosely bound system of partons (and ignore their masses), we can characterize a given parton by the momentum fraction it carries: for each parton i, there will be a function $f_i(\xi)$ that expresses the probability that the proton contains a parton i with a longitudinal momentum fraction ξ. Naturally, in the infinite momentum frame $0 < \xi < 1$. The expression for the total cross section will then contain an integral over ξ. The 4-momentum of the parton is $p = \xi$P (P-the 4-momentum of the proton). Then

$$\hat{s} = (p+k)^2 = 2pk = 2\xi Pk = \xi s, \tag{1.8}$$

where $s = (P+k)^2 \simeq 2Pk$ is the square of the proton-electron center of mass energy.

Taking into account the "on-shellness" of the outgoing quark and neglecting the quark mass:

$$0 \approx (p+q)^2 = 2pq + q^2 = 2\xi Pq - Q^2 \Rightarrow \xi = \frac{Q^2}{2Pq} \equiv x \tag{1.9}$$

where x is known as the Bjorken variable.

In the parton model one can predict the event distribution in the $Q^2 - x$ plane. Using distribution functions $f_i(\xi)$ evaluated at given $\xi = x$, the estimations for Mandelstam variables done above and the cross section for the DIS subprocess, we find the following distribution:

$$\frac{d^2\sigma}{dxdQ^2} = \sum f_i(x) Q_i^2 \frac{2\pi\alpha^2}{Q^4}\left[1 + (1 - \frac{Q^2}{xs})^2\right] \tag{1.10}$$

In the latter equation the factor $1/Q^4$ arises from the partonic subprocess, and the factor $f_i(x)$ from the proton "partonic structure". Within the parton model, the rescaled cross section $Q^4 d^2\sigma/dxdQ^2$ is Q^2 independent. This property is known as Bjorken scaling.

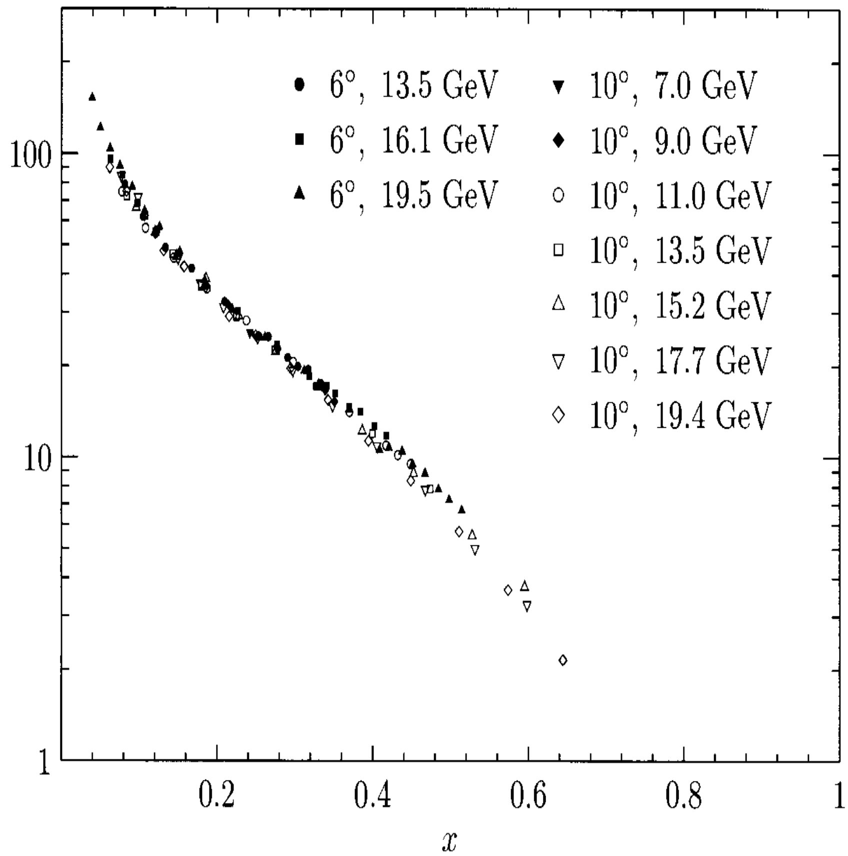

Figure 1.4: Test of Bjorken Scaling using e^-p deep inelastic scattering [7]. The plot of total cross section $d^2\sigma/dxdQ^2$ is rescaled by the factor $[1 + (1 - Q^2/xs)^2/Q^4]$, for the various initial electron energies and scattering angles. The data span the the range $1\text{GeV}^2 < Q^2 < 8\text{GeV}^2$

SLAC-MIT exhibited Bjorken scaling to about 10 percent accuracy, for Q above 1 GeV (See Fig. 1.4) [7].

Finally, let us mention that in the parton model, the DIS cross section trivially factorizes as the product between $f_i(x)$ and the cross section for $\gamma^* q \to q$.

1.2.2 QCD Factorization theorems

In the parton model description of DIS, only electrically charged partons (i.e., quarks) play a role, and their mutual interactions (strong and a fortiori electromagnetic) are neglected. With the advent of QCD in the 70's, it became possible to improve the accuracy of the parton model by including the effect of gluons and systematically taking into account the mutual strong interactions between partons. Although the latter corrections are formally small (thanks to asymptotic freedom, $\alpha_s(Q^2) \ll 1$ at large enough Q^2), they can be sizeable at available collision energies. In the same time, factorization becomes less obvious, and very delicate to prove.

Factorization theorems [8] are one of the most important successes of QCD. Suppose that we have the following hadronic process

$$A + B \rightarrow H + X \tag{1.11}$$

According to factorization theorems, at high energy the production cross section can be written as :

$$d\sigma_{AB\rightarrow H+X} = f_{a_1/A}(x_1, Q^2) \otimes f_{a_2/B}(x_2, Q^2) \otimes \hat{\sigma}(a_1 a_2 \rightarrow bc \cdots) D_{c\rightarrow h}(z, Q^2) \tag{1.12}$$

Here $\hat{\sigma}(a_1 a_2 \rightarrow bc)$ is a partonic cross section, in principle computable to a given order in α_s in pQCD, $f_{a/A}$, $f_{b/B}$ are parton distribution functions expressing the probability to find a parton $a(b)$ in hadron $A(B)$, $D_{c\rightarrow h}$ is a fragmentation function expressing the probability that the outgoing parton c fragments into a final hadron H. f and D are not calculable in pQCD.

Schematically the factorization will look like as in Fig. 1.5.

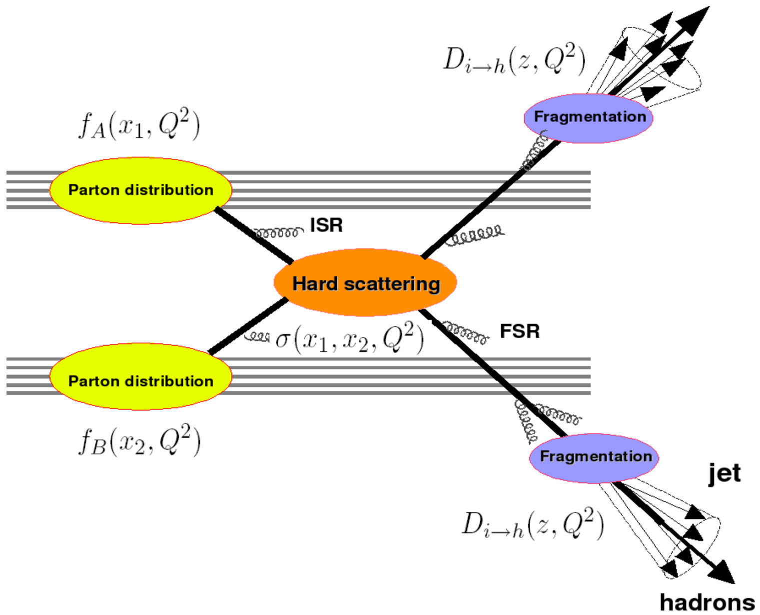

Figure 1.5: sketch of pQCD factorization

The equation (1.12) is valid due to the fact that it is possible to separate long and short distance effects with independent time (length) scales: the partonic process has a short time scale of order $\tau_{hard} \sim 1/Q$, whereas $f_{a/A}$, $D_{c\rightarrow H}$

resum collinear radiation (see next section) with characteristic formation time $\tau_{DGLAP} \sim \frac{1}{\Lambda}$. Thus one can understand why factorization may work in some cases.

A few remarks:

- Factorization theorems are very difficult to prove.
- Present consensus:
  - Factorization in DIS $\frac{d\sigma}{dxdQ^2}$ is rigorously proven [6]
  - Factorization in DY is also proven [10]
  - Hadron/jet production at large p_T: much more difficult to prove but confrontation with data suggests factorization to a good accuracy
  - Quarkonium production at large p_T [11]: problematic.

It is now accepted that factorization can be violated in many cases:

- For less inclusive observables, for example $\frac{d\sigma}{dp_T d\phi}$, $\frac{d\sigma}{dp_T dy}$
- When there are several energy scales($\sqrt{s}, p_T, M..$).
- In general for observables sensitive to late and soft rescatterings (on hadronic or partonic comovers for instance), see Fig. 1.6.

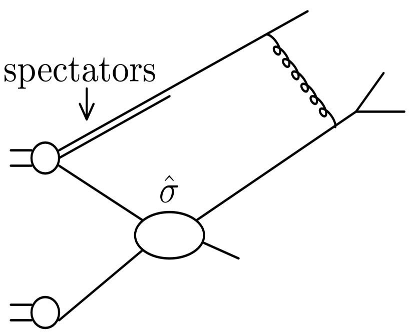

Figure 1.6: Late rescattering potentially breaking factorization.

1.2.3 DGLAP equations

In QCD the quantities of interest are those which are free of collinear and soft divergencies. In this section I will briefly explain the notion of collinear factorization in the simplest case of DIS, and how the presence of this singularities leads to the differential equations that describe parton evolution. First I will try to explain the origin of collinear logarithms, then I show that these singularities can be resummed in parton distribution functions.

In DIS collinear divergencies appear for instance when considering initial parton radiation (See Fig.1.7). The DIS cross section with single gluon ra-

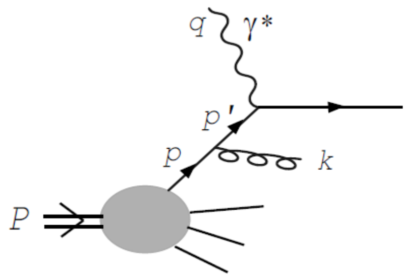

Figure 1.7: Initial parton radiation.

diation in the limit where the gluon is soft compared to the radiating quark ($|\vec{k}| \ll |\vec{p}\,|$) reads:

$$d\sigma_{rad} = \sigma_0 \frac{C_F \alpha_s}{\pi} \frac{d|\vec{k}|}{\omega} \frac{\theta^2 d\theta^2}{[\theta^2 + \frac{m^2}{|\vec{p}|^2} + \frac{\lambda^2}{\omega^2} - \frac{v^2}{\omega|\vec{p}|}]^2} \tag{1.13}$$

where σ_0 stands for the DIS cross section without gluon radiation, θ is the angle between $\vec{p}$ and $\vec{k}$, m is the quark mass, $v^2 = p^2 - m^2$ the radiating quark virtuality, λ the "gluon mass" and $\omega = \sqrt{\vec{k}^2 + \lambda^2}$ the on-shell gluon energy.

In the soft gluon limit ($\omega \ll| \vec{p}\,|$), (1.13) is simply obtained as follows. The amplitude for gluon radiation is:

$$M_{rad} \simeq T^a_{ji} \frac{2g(\mathrm{p}\varepsilon^*)}{(p-k)^2 - m^2} M_{el} \tag{1.14}$$

where $\varepsilon = (0, \vec{\varepsilon})$ that corresponds to a Coulomb gauge. Here M_{el} is the DIS amplitude without radiation.The denominator can be re-written as:

$$(p-k)^2 - m^2 = p^2 - 2pk + k^2 - m^2 \tag{1.15}$$

With $\lambda^2 = k^2$ the gluon virtuality, and $p^2 - m^2 = v^2$, then

$$M_{rad} \simeq (\frac{2g\mathrm{p}\varepsilon^*}{v^2 + \lambda^2 - 2pk}) M_{el} \tag{1.16}$$

In the high energy limit,

$$E_p = \sqrt{\vec{p}^2 + m^2 + v^2} \simeq |\vec{p}\,| + \frac{m^2 + v^2}{2|\vec{p}|} \tag{1.17}$$

$$E_k \equiv \omega = \sqrt{\vec{k}^2 + \lambda^2} \simeq |\vec{k}\,| + \frac{\lambda^2}{2|\vec{k}|} \tag{1.18}$$

Let us assume that the angle θ between $\vec{p}$ and $\vec{k}$ is small, then we have $|\vec{p}\vec{\varepsilon}| \simeq |\vec{p}|\theta$ since $\vec{\varepsilon}$ is perpendicular to $\vec{k}$. We get the following expression for the amplitude (1.16):

$$|M_{rad}|^2 \simeq C_F \frac{1}{|\vec{k}^2|} \left(\frac{2g\theta}{\theta^2 + \frac{m^2}{|\vec{p}|^2} + \frac{\lambda^2}{\omega^2} - \frac{v^2}{\omega|\vec{p}|}} \right)^2 |M_{el}|^2 \tag{1.19}$$

Here, m^2, λ^2 and v^2 play the role of regulators for potential divergencies.

In the above equation (1.19) the summation over color indices. The cross section to radiate a gluon is

$$d\sigma_{rad} = \sigma_0 \frac{M_{rad}^2}{M_{el}^2} \frac{d^3\vec{k}}{(2\pi)^2 2\omega} \tag{1.20}$$

By setting all of IR regulators to zero in (1.13) and performing the integration in the limit where $\theta \ll 1$, one can see that the θ integral in (1.13) is divergent. To make this integral well-defined, the cut-off needs to be imposed. Once the integral is well defined, the integration gives what is called a collinear log.

It can be shown that (1.13) gives:

$$\sigma_{rad}^{QCD} \propto \alpha_s \log\left(\frac{|\vec{p}|^2}{|v^2|}\right) \log\left(\frac{|\vec{p}|^2}{\lambda^2}\right) \sigma_0 \tag{1.21}$$

Here, the second log is called a "soft" log. It is calculated in the limit where $|\vec{k}| \to 0$. The first log is a "collinear logarithm", made finite thanks to the quark virtuality v^2.

A complete derivation requires adding all Feynman diagrams contributing to the same order in α_s. In particular we should add the contributions corresponding to the radiation of the outgoing quark and to the virtual corrections. Once we sum all contributions, the soft divergencies at $|\vec{k}| \to 0$ cancel out in the DIS cross section. On the other hand "collinear" logs remain [12].

One now shows that successive collinear emissions obey strong $k_\perp$-ordering (See Fig. 1.8).

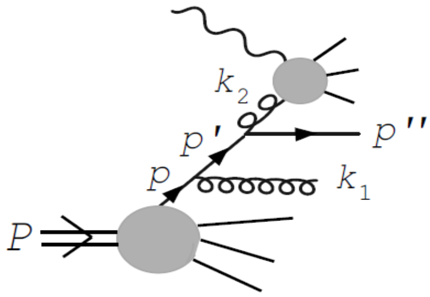

Figure 1.8: Multiple parton branching

In case of a single gluon emission (as in Fig.1.7), the collinear divergence appears when $p^2 = 0$ and $p'^2 \to 0$. This gives a factor

$$\int \frac{d^2\vec{k}_{1\perp}}{k^2_{1\perp}} \sim \log\left(\frac{Q^2}{\Lambda^2}\right) \tag{1.22}$$

If we take the limit $k_2^2 \to 0$, one can get another log which is $\sim \int d^2\vec{k}_{2\perp}/k^2_{2\perp}$, provided that $p'^2 \sim k^2_{1\perp}$ is neglected, i.e., $k_{1\perp} \ll k_{2\perp}$.

In general, in case of multiple emissions, the leading collinear singularity originates from the kinematical region where the intermediate parton virtualities are strongly ordered,

$$\Lambda \ll k_{1\perp} \ll k_{2\perp} \ll \ldots \ll k_{n\perp} \ll Q \tag{1.23}$$

this gives a factor

$$\int_{\Lambda^2}^{Q^2} \frac{dk^2_{n\perp}}{k^2_{n\perp}} \int \ldots \int_{\Lambda^2}^{k^2_{3\perp}} \frac{dk^2_{2\perp}}{k^2_{2\perp}} \int_{\Lambda^2}^{k^2_{2\perp}} \frac{dk^2_{1\perp}}{k^2_{1\perp}} \propto \left[\log\left(\frac{Q^2}{\Lambda^2}\right)\right]^n \tag{1.24}$$

As far as the leading collinear singularity is concerned, the last emission originates from a parton with a negligible $k_\perp$, i.e., it is almost collinear to the radiating parton.

We define $f_{g/p}(x, Q)$ (and $f_{q/p}(x, Q)$) the probability to find in the proton a gluon (quark) with longitudinal momentum fraction x and virtuality less than Q^2 [6]. The quantity $f_{g/p}(x, Q)$ takes into account all collinear radiation at $k_\perp < Q$. A gluon with x and virtuality up to $Q + dQ$ can arise from a gluon with x and virtuality up to Q which has not radiated or from a parent parton with $x' > x$ (and virtuality up to Q) which has splitted collinearly into the gluon. Analytically it can be expressed as follows:

$$f_{g/p}(x, Q+dQ) = f_{g/p}(x, Q) + \int_0^1 dx' f_{q/p}(x', Q) \frac{\alpha_s(Q^2)}{2\pi} \frac{dQ^2}{Q^2} \int_0^1 dz P_{gq}(z)\delta(x - x'z) \tag{1.25}$$

Here $P_{gq}(z)$ is called a splitting function. This function is interpreted as the probability to find a parton of type g in a parton of type q with a fraction z of the longitudinal momentum of the parent parton. In (1.25) Q naturally gives the scale of the coupling. We get the following integro-differential equation:

$$\frac{\partial f_{g/p}(x,Q)}{\partial \log(Q^2)} = \frac{\alpha_s(Q^2)}{2\pi} \int_x^1 \frac{dz}{z} P_{gq}(z) f_{q/p}(\frac{x}{z}, Q) \tag{1.26}$$

To make the latter equation complete we must add the contributions corresponding to the splittings $\bar{q} \to g$ and $g \to g$. We obtain the DGLAP equation for the evolution of $f_{g/p}$ as a function of Q,

$$\frac{\partial f_{g/p}(x,Q)}{\partial \log(Q^2)} = \frac{\alpha_s(Q^2)}{2\pi} \int_x^1 \frac{dz}{z} \left\{ P_{gq}(z) \sum [f_{q_f/p}\left(\frac{x}{z}, Q\right) + f_{\bar{q}_f/p}\left(\frac{x}{z}, Q\right)] + P_{gg}(z) f_{g/p}(\frac{x}{z}, Q) \right\} \tag{1.27}$$

where we included a sum over the light quark flavours $q_f = u, d, s$ [13], [14]. The complete DGLAP equations are obtained by combining (1.27) with a similar equation for $\partial f_{q/p}/\partial \log(Q^2)$.

1.3 Tests of pQCD

Since the early 1970s, QCD has been tested in many experiments using various projectiles and targets, at various collision energies $\sqrt{s}$, and for many different observables. In this section I briefly review those where QCD have been tested with great success [15].

1.3.1 DGLAP equations

The DGLAP equations are a fundamental result of pQCD. The solutions $f(x, Q)$ of the first order differential equations will depend on some initial conditions $f(x, Q_0)$, which cannot be predicted from first principles. Those initial conditions must be taken from the experiment. Roughly speaking, by measuring the DIS cross section at Q_0 for different values of x, one can access the structure functions $F_1(x, Q_0^2)$ and $F_2(x, Q_0^2)$ which are related to the parton distributions $f(x, Q_0)$. The structure functions $F_i(x, Q^2)$ at $Q > Q_0$ can be then predicted by applying the DGLAP evolution equations. The experimental measurements show a spectacular agreement with theoretical predictions (Fig.1.9).

The test of DGLAP equations showed that Bjorken scaling can be violated and that the parton model is not fully accurate, especially at large x and Q^2.

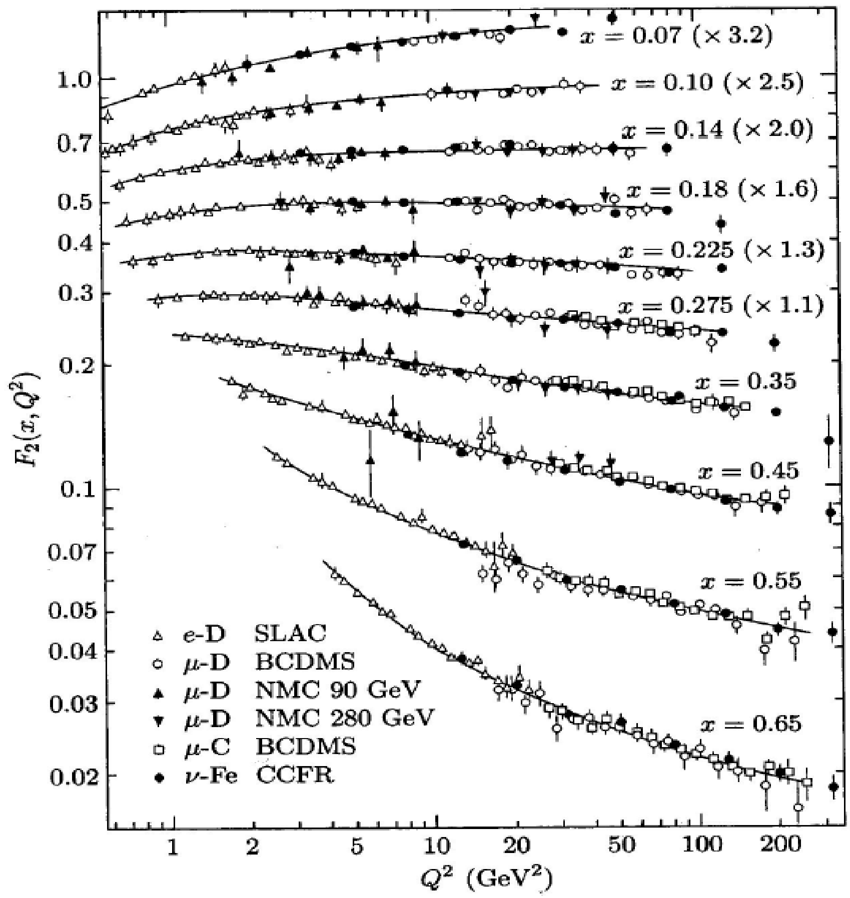

Figure 1.9: Q^2 dependence of the combination of quark distribution functions F_2 measured in DIS [17]

1.3.2 Deep Inelastic Scattering

Many studies were done concerning the experimental measurement of the structure functions $F_i(x, Q^2)$ whose relation to parton distribution functions was mentioned above. Here I briefly mention a few features of this extensive field.

The most striking feature of the SLAC DIS data [16] was scaling: the approximate independence of the measured structure function $F_i(x, Q^2)$ in Q^2, which was an indication of the scattering from the point-like constituents, named partons. The basic idea of the parton model was confirmed after this experimental observation.

QCD predicted the violation of scaling, a subtle effect since it depends on $\ln Q^2$. This was confirmed by later experiments.

The structure function $F_2^l(x, Q^2)$ measured in neutral current (virtual) γ

exchange processes ($l = e, \mu$) and in charged current ($W^{\pm}$ exchange) is in principle different (Fig.1.10). According to the parton model, they are related to the same PDFs, but multiplied by the appropriate coupling constant and weak isospin matrix element. After summing over all parton distribution functions the theory predicts $F_2^{eA}(x, Q^2)/F_2^{\nu A - \bar{\nu} A}(x, Q^2) = 5/18$. This "charge ratio" has been verified to great accuracy in all DIS experiment [18].

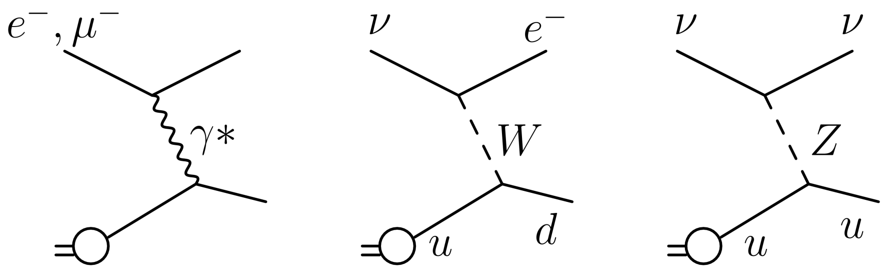

Figure 1.10: Various DIS processes of interest with γ, W, Z exchange

1.3.3 Electron-Positron Annihilation into Hadrons

In experiments done in PETRA, PEP, CELLO (see Fig.1.11) [19] the emergence of jet-like hadronic final states was observed, which is the direct evidence for the existence of partons. The dominance of these events gave the first visual evidence of the parton-anti-parton final state previously inferred indirectly from the total cross section measurements and DIS.

One can assume that the measured angular distribution of 2-jets gives direct evidence on the angular distribution of parton-anti-parton pair, which is parametrized as $(1 + \cos^2 \theta)$. Indeed, measured distribution coincides with the distribution calculated theoretically in the parton model approximation(Fig.1.12).

1.3.4 QCD in hadron-hadron collisions

Another important process to consider is lepton pair production in hadron-hadron collisions ($A + B \to l^+ l^- + X$), the so-called Drell-Yan (DY) process. In the parton model the lepton pair is created through the basic quark-anti-quark annihilation $q\bar{q} \to l^+ l^-$, and the parton model cross section at fixed center-of-mass pair rapidity ($y = (1/2)\ln(x_1/x_2)$) is given by,

$$Q^4 \frac{d^2\sigma}{dy dQ^2} = \left[\frac{4\pi\alpha^2}{9} x_1 x_2\right] \sum_q e_q^2 (f_{q/A}(x_1) f_{\bar{q}/B}(x_2) + f_{\bar{q}/A}(x_1) f_{q/B}(x_2)) \quad (1.28)$$

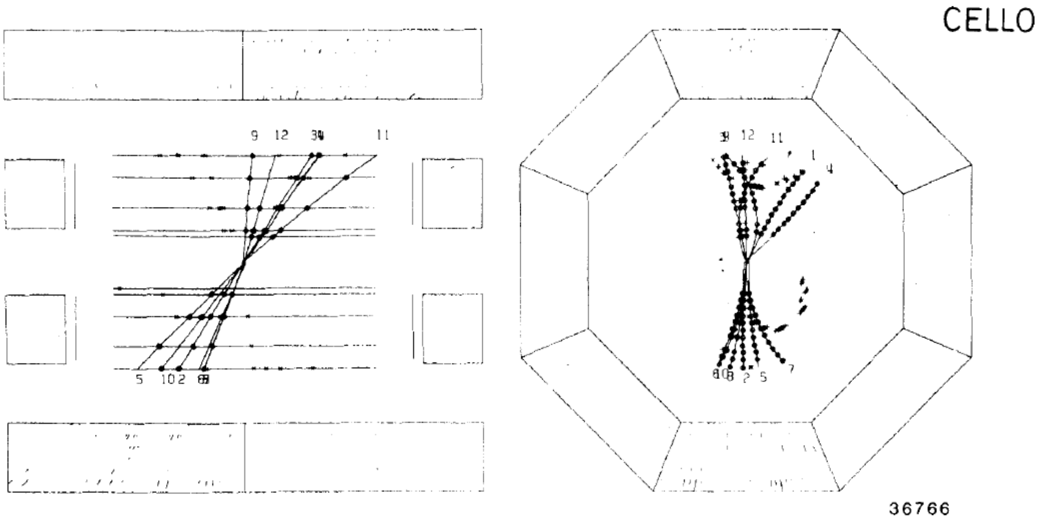

Figure 1.11: 2-jet events observed in CELLO experiment [19]

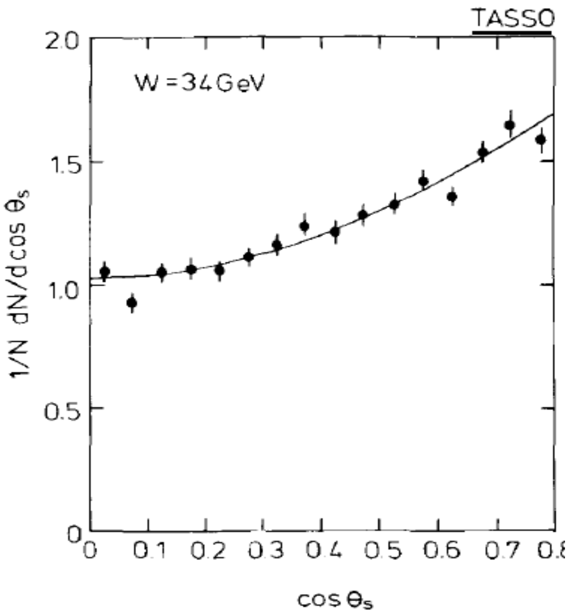

Figure 1.12: Angular distribution. The curve is proportional to $1 + \cos^2\theta$ [19].

where $x_{1,2} = (Q/\sqrt{s})e^{\pm y}$. The main features of this formula are:

- Scaling: The fact that the right-hand side of this equation is independent of Q means that the cross-section satisfies *scaling*. This is another evidence for point-like interaction. Scaling allows one to predict the cross-section at higher energies from low energy measurements [20].

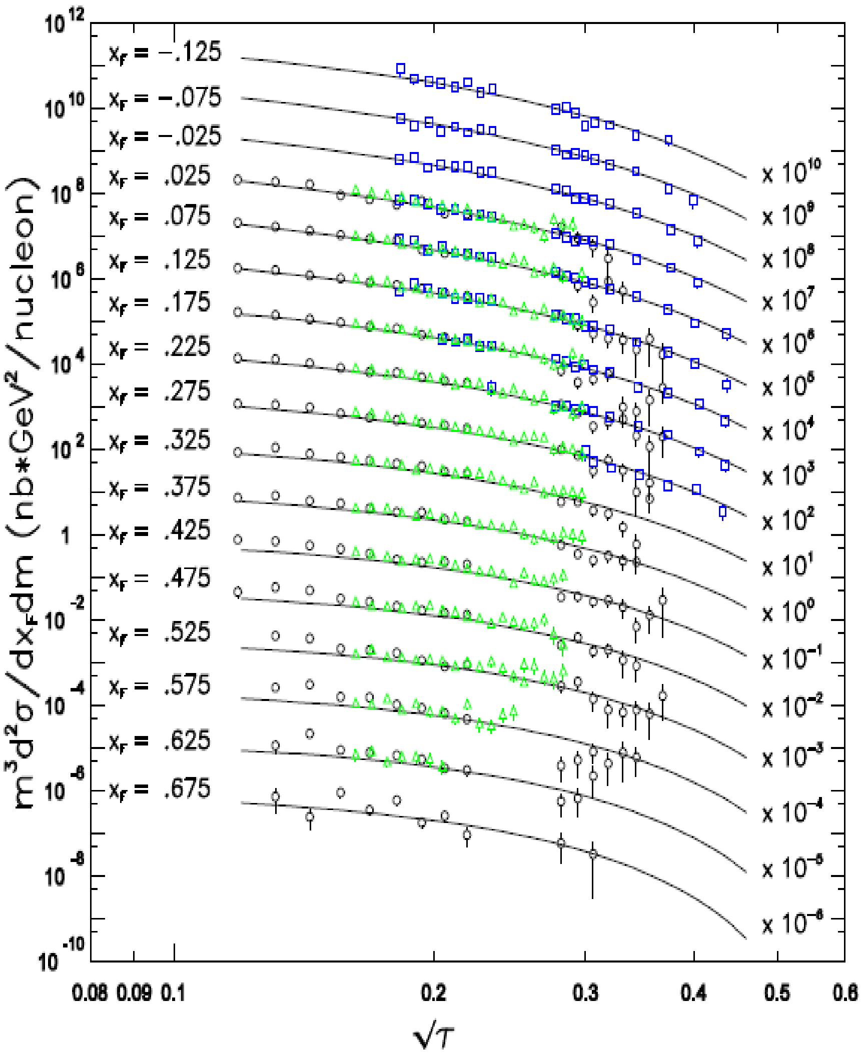

Figure 1.13: Comparison of DY data with NLO calculation using MRST structure function [20]. Here $\tau = x_1 x_2$, E772, E603, NA3 data points are shown as circles, squares, triangles respectively.

- Color factor: The overall factor in this formula contains a "color factor" 3 in the denominator. This factor played an important role in determining *Quantum Chromodynamics* to be the underlying fundamental theory of strong interactions when parton distribution functions measured in DIS experiments were used in the above formula to predict the lepton-pair production cross-sections.

- Cross section ratios: The formula for the DY cross section (1.28) leads to many simple predictions on cross-section ratios which agree well with experiment and were used in establishing the credibility of the parton model during its early stage of developement. For instance:

$$\frac{\sigma(\pi^+ N \to \mu^+\mu^-)}{\sigma(\pi^- N \to \mu^+\mu^-)} \to \left(\frac{e_d}{e_u}\right)^2 = \left(-\frac{1}{3}\right)^2 : \left(\frac{2}{3}\right)^2 = \frac{1}{4} \tag{1.29}$$

  as $\tau = Q^2/S \to 1$, i.e., in the region where the valence quark is presumed to be dominating. When $\tau \to 0$, pions contain equal amounts of $\bar{u}$ and $\bar{d}$ quarks, and the ratio (1.29) tends to 1.

- Angular distribution of the leptons: Since the underlying process for lepton pair production $q\bar{q} \to l^+l^-$ is very similar to $e^+e^- \to \mu^+\mu^-$, the angular distribution of these 2 processes should be similar. The angular distribution of the outgoing leptons in their center-of-mass frame is expected to be $\sim (1 + \cos^2\theta)$, and if the parton model is a good approximation, the angular distribution of the DY pair should be the same. Experimental data confirmed this fact [21].

1.4 Lattice QCD

In the framework of pQCD applied at hard scales $Q \gg \Lambda$, the coupling constant is small. On the contrary at large distances ($Q \sim \Lambda$) the coupling becomes large. In this regime perturbation theory is not valid. In this section we briefly describe the Euclidean version of QCD on a four-dimensional lattice, named lattice QCD (LQCD), used to adress the non-perturbative domain of QCD. The discussion is based on Ref. [17].

The basic idea is to separate the field operators by discretizing Euclidean space-time into hypercubes with the side of length a (Fig.1.14).

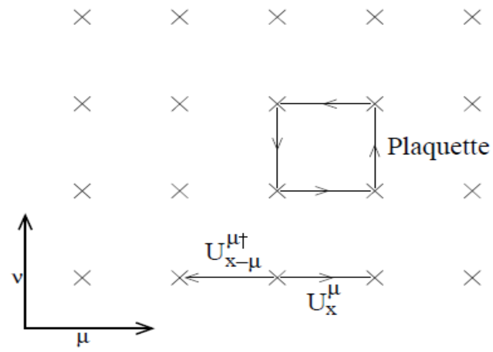

Figure 1.14: Quark and gluon fields on a space-time lattice.

By doing this, full Lorentz invariance is reduced to hypercubic symmetry, but the lattice version of the theory preserves gauge invariance. The lattice spacing provides an ultraviolet cut-off of order π/a on all momenta so that ultraviolet divergencies are absent. As long as the lattice spacing a is small compared to the size of hadrons that one is studying, the lattice version of the theory should be an adequate approximation.

One places the anticommuting quark fields $\psi(x)$ and $\bar{\psi}(x)$ on lattice sites, whereas the gluon fields are represented by the links connecting the sites, see Fig. 1.14 [22]. A directed link from site x in the positive direction $\hat{\mu}$ is associated with the gluon field U^{μ}_{x}, while the link to the site $x-\mu$ in the opposite direction is $(U^{\mu}_{x-\hat{\mu}})^{+}$ (hermitian conjugate). Defining a gauge invariant action S on the lattice, physical predictions are then made by evaluating the integral of e^{-S} over all configurations of the fields. The fermionic part normally appears as a bilinear term and can be integrated out :

$$\begin{aligned} &\int \{dU_{\mu}\} dq d\bar{q} \exp[-S_G(U) + \bar{q}M(U)q] \\ = &\int \{dU_{\mu}\} \det M(U) \exp[-S_G(U)] \end{aligned} \tag{1.30}$$

Here $S_G(U)$ is the action of the pure gauge field theory, which can be found in [17]. The factor $detM(U)$ includes quark dynamics. The above integral is a functional integral which is approximated by integrating over all fields and links on the lattice. The most common technique to do the integration is a Monte Carlo evaluation of the integral, yet the calculation is very costly in time. To simplify, the calculations are often performed in the quenched approximation which replaces the determinant in (1.30) by a constant independent of link variables U.

In the quenched approximation the expectation value of any operator $O(U)$ is:

$$\langle O \rangle = \frac{\int \{dU_\mu\} O(U) \exp[-S_G(U)]}{\int \{dU_\mu\} \exp[-S_G(U)]} \tag{1.31}$$

To be an adequate theory LQCD must satisfy two main conditions:

- The size of the lattice should be large enough, so that the calculated quantity is not affected by finite size effects.

- The lattice spacing must be small enough for the calculated physical quantity to be insensitive to the granularity of the lattice.

One of the main successes of LQCD concerns the calculation of hadron masses. A satisfactory agreement between experiment and theory was obtained while calculating the mass spectrum. The figure 1.15 shows the results of a lattice calculation of hadron masses performed with Wilson fermions in the quenched approximation, compared to the measured hadron masses. The very good

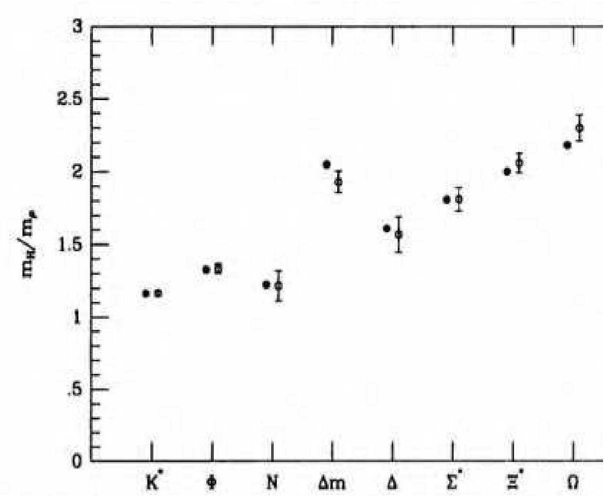

Figure 1.15: Hadron masses in units of ρ mass from the lattice (open points) compared with experiment (solid points), from [17]. The quantity Δm refers to the combination of masses $m_\Xi + m_\Sigma - m_N$.

agreement between theory and experiment indicates that the quenched approximation is reliable for the calculation of hadron masses.

As a second example of the successes of lattice QCD one can mention the calculation of the static $q\bar{q}$ potential, performed in the quenched approximation (see Fig.1.16).

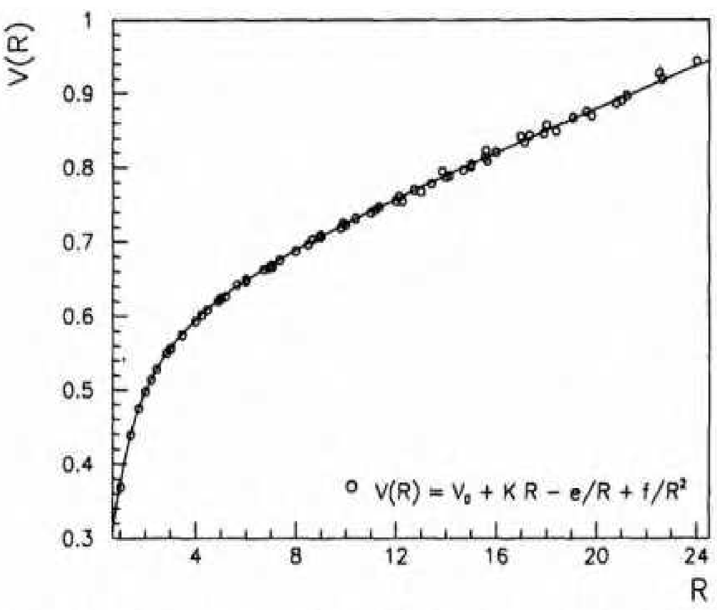

Figure 1.16: QCD potential vs. R (in lattice units) from lattice QCD [17]

As was mentioned in the previous sections, at small distances the potential is expected to be of the form:

$$V(R) \sim -\alpha_s/R \tag{1.32}$$

On the other hand, at large distances we have a linearly rising potential

$$V(R) \sim KR, \tag{1.33}$$

where K is the string tension. The curve in Fig. 1.16 is a fit to the lattice data, respecting the two above limiting forms. As we can observe, the expected small and large distance limits of the potential are well reproduced by lattice QCD.

1.5 Quark-Gluon Plasma

1.5.1 Indications from the lattice

Lattice QCD also allows to do calculations at finite temperature. If the temperature of the system is much larger than the mass of its constituents the relevant energy scale is the temperature. Let's consider a relativistic quantum system. As we know from thermodynamics, the properties of the system in thermal equilibrium can be described by the partition function, since the latter can be related to quantities like total energy, entropy, pressure, etc. We can define an analogous quantity in quantum field theory. In QFT the partition function of a system described by Hamiltonian H is:

$$Z = Tr(e^{-\beta H}) = \sum_{\varphi} \langle\varphi|e^{-\beta H}|\varphi\rangle \tag{1.34}$$

where $\beta = (1/T)$, and $\{|\varphi\rangle\}$ denotes a complete set of thermal states. The calculation of Z is based on a formal analogy between β and imaginary time. If we write:

$$\langle\varphi|e^{-\beta H}|\varphi\rangle = \langle\varphi|e^{-iH(-i\beta)}|\varphi\rangle \tag{1.35}$$

we recognize the evolution operator of the system e^{-iHt}, where $t = -i\beta$. From this we can conclude that we have a probability amplitude for a state $|\varphi\rangle$ at time t_i to find itself in the same state at time $t_i - i\beta$.
The amplitude can be written in the form of a path integral:

$$\langle\varphi|e^{\beta H}|\varphi\rangle = \int_{\phi(t_i)=\phi(t_i-i\beta)=\varphi} D\phi\, e^{i\int_{t_i}^{t_i-i\beta} L(\phi)dt} \tag{1.36}$$

The action S has to be evaluated along a contour which links t_i to $t_i - i\beta$ in the complex-time plane. From (1.34)-(1.36) one can see that Z is an integral of e^{iS} over the periodic path $\phi(t_i) = \phi(t_i - i\beta)$.

One can recall the expression for a classical partition function :

$$Z = \sum_{s} e^{-\beta E_s} \tag{1.37}$$

In the limit $S \gg h$, the expression obtained in QFT is equivalent to the one in thermodynamics. Once we have the partition function, we can calculate the physical quantities of interest such as energy density and pressure. One of the achievements of quenched LQCD is the discovery of a phase transition between hadronic matter and Quark Gluon Plasma (QGP) at a critical temperature $T_c \sim$ 170-190 MeV.

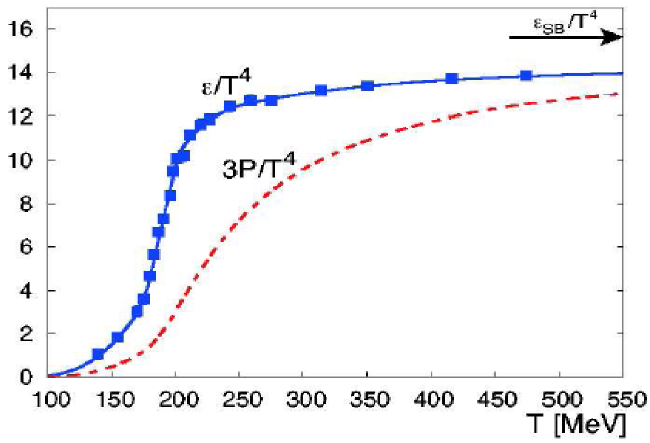

Figure 1.17: Energy density and pressure from lattice, [23]

The expression of the energy density of an ideal gas is :

$$\varepsilon = \frac{\pi^2}{30}\, d\, T^4 \tag{1.38}$$

where d is the number of degrees of freedom. The LQCD results (Fig.1.17) suggest a rapid change of the number of d.o.f., i.e., a phase transition. The order of magnitude of ε/T^4 at large $T > T_c \sim 200$ MeV is moreover consistent with that expected for a quark-gluon plasma

$$d = n_f \times 2 \times 2 \times 3 \times \frac{7}{8} + 2 \times 8 = 16 + \frac{21 n_f}{2} \tag{1.39}$$

In the first term (written for quarks) we take into account $n_f = 3$ flavors, 2 spin states and 2 particle states (corresponding to quark anti-quark). In the second term (written for gluons) we have a factor 2 for the two gluon helicity states, and a factor 8 is for color. Eventually we get:

$$d = \frac{95}{2} = 47.5 \tag{1.40}$$

for $n_f = 3$, giving $\varepsilon/T^4 = d\pi^2/30 \simeq 16$, which is consistent with the lattice data at $T \sim 500$ MeV, see Fig. 1.17.

1.5.2 Bjorken model of $A - A$ collisions

The QGP can be produced in relativistic heavy-ion collisions. This can be understood in the space-time picture of the collision proposed by Bjorken [24].

Let us consider colliding two nuclei and the c.m. frame of the collision, see Fig. 1.18.

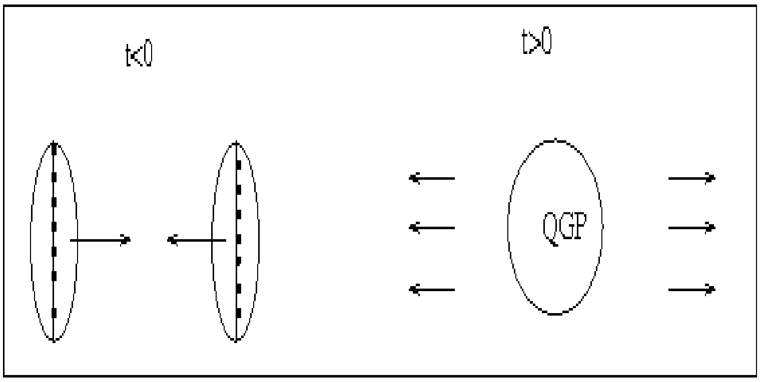

Figure 1.18: Bjorken model of nucleus-nucleus collisions

Apart from valence quarks, each nucleus contains low-momentum partons called wee partons by Bjorken. As a result of Lorentz contraction, the longitudinal (i.e. parallel to beam axis) spread of the valence quark wave function is reduced to $\sim 2R/\gamma$, where R is the nuclear radius and γ the Lorentz factor.

However, no matter how high is the beam energy, the incoming nuclei always contain wee partons with typical momenta $p \sim \Lambda_{QCD}$. As a result, the collision of 2 nuclei can be viewed as the collision of 2 "wee parton clouds" of longitudinal spread $\Lambda_{QCD}^{-1} \simeq 1$ fm. In such a collision, we expect many soft interactions producing a large number of virtual quanta. The energy where the wee parton cloud is broader than the spread of the valence wave function can be easily approximated. Using the condition $2R_A/\gamma < 1$fm and the fact that $\gamma = \sqrt{s}_{NN}/2m_p$, one sees that at energies $\sqrt{s} > 4m_pR_A \simeq 30$ GeV one should expect a collision dominated by the wee partons, and the possible formation of a QGP.

The virtual quanta need a finite time (τ_{dec}) to decohere and turn into real (thermal) quarks and gluons. Here τ_{dec} refers to the rest frame of an individual parton.

Schematically the development of nucleus-nucleus collisions can be seen on Fig. 1.19, where hyperbolas of constant proper time $\tau = \sqrt{t^2 - z^2}$ are shown. All points on a given hyperbola are at the same stage of evolution [22]. Let's define hyperbola 1 as $\tau = \tau_{dec}$. This means that, parton at z undergoes decoherence at time $t = \sqrt{\tau_{dec}^2 + z^2}$. The larger z, the larger the decoherence time.

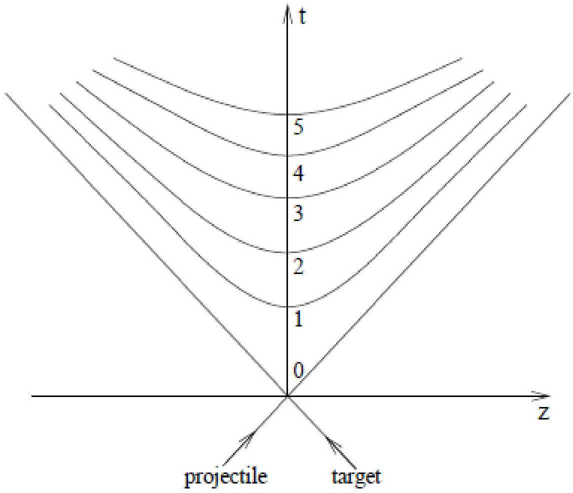

Figure 1.19: Space-time picture of ultrarelativistic nucleus-nucleus collision

Even if QGP is formed, its lifetime will be of order of a few $fm/c \sim O(10^{-23}\mathrm{s})$, and what experimentalists see in the detectors are not quarks and gluons, but the confined hadrons (as well as leptons and photons). It is a highly non-trivial task to infer the QGP formation from the properties of the detected particles.

1.5.3 Some Important QGP signals

QGP can be "observed" only via indirect signatures. A few of them, considered as the most convincing, are sketched below.

Elliptic flow

A fundamental quantity to measure in heavy-ion collisions is elliptic flow [9]. Consider the hot "almond" of the overlap region in a peripheral collision. The momentum and coordinate space representation of this almond is shown in Fig. 1.20. In coordinate space, the overlap region is an ellipse/almond, since it is the overlap of two spherical projections. Once the system evolves, it is easier for particles to move along the direction x of the small size of the almond, hence in the final state (the almond) turns into a sphere.

In momentum space the initial distribution is a sphere, since at the initial stage partons in the overlap region all move isotropically. As the system evolves and fields scatter off one another, particles realize that it is easier to move in the x direction, due to a thinner path to cross. This can also be understood by uncertainty principle, implying that the partons at smaller x

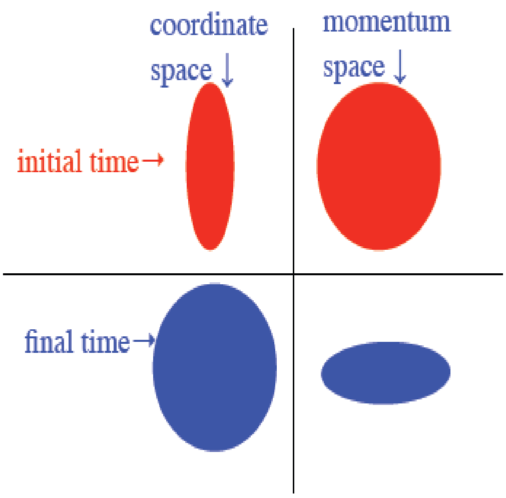

Figure 1.20: Elliptic flow in peripheral collision: evolution in both coordinate and momentum space [9].

have larger p_x. Hence particles acquire more p_x than p_y and the sphere starts to shrink [2]. This is caracterized by the quantity

$$v_2 = \frac{< p_x^2 - p_y^2 >}{< p_x^2 + p_y^2 >} \tag{1.41}$$

This quantity is well defined and can be measured experimentally. The average is done with respect to number of participants. The main problem is determining the x and y axes. The mere existence of elliptic flow tells us that there are significant interactions in $A - A$ collisions.

One way to compute v_2 is to use a hydrodynamic description. For hydrodynamics we need an equation of state, which can be taken from lattice calculations. One also needs to specify transport coefficients of the medium, like bulk and shear viscosity. We will concentrate on shear viscosity.

The simplest way to define shear viscosity is to think of two plates paralel to the (x, z) plane and separated by the distance y. If one plate is fixed, and the other one moves with constant velocity in the direction of x, shear stress is proportional to the viscosity times the gradient of the velocity in y. That is the more viscous is the fluid, the harder it is to move one plate parallel to the other.

Hydrodynamics predicts elliptic flow, and it is found that elliptic flow provides a strong constraint on the ratio of shear viscosity η to the entropy

[2]The latter argument is classical and applies in particular to a large medium and is thus not based on the uncertainty principle.

density s [9]

$$\frac{\eta}{s} \approx 0.1 \pm 0.1(theory) \pm 0.1(experiment) \tag{1.42}$$

The quantity η/s quoted since it enters naturally in hydrodynamics. In Fig 1.21 one can see the comparison of this value for various non-relativistic systems.

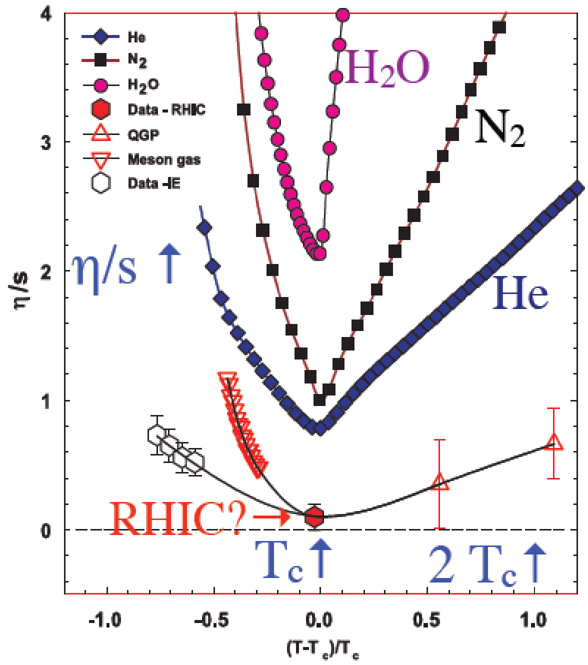

Figure 1.21: Shear viscosity in various non-relativistic systems [9]

Even given the error bars, the value of η/s in (1.42) is quite small. The value for QGP extracted at RHIC is almost an order of magnitude smaller than the value for liquid helium. For this reason it is believed that the state of nuclear matter produced in heavy-ion collisions at RHIC is the "most perfect fluid" ever seen.

Jet quenching

Another important quantity is the nuclear modification factor R_{AA}, which is defined as the ratio of same particle production cross section in $A-A$ and $p-p$ collisions, normalized by the number of binary collisions,

$$R_{AA}(p_T) = \frac{1}{n_{coll}} \frac{d\sigma_{AA}(p_T)/dp_T}{d\sigma_{pp}(p_T)/dp_T} \tag{1.43}$$

If $R_{AA} = 1$, then there would not be any other effect than the scaling in n_{coll} when going from $p - p$ to $A - A$, but $R_{AA} \neq 1$ means that additional nuclear effects must be present. The experiments show that R_{AA} in central collisions is much less than 1, see Fig. 1.22 for the LHC data in $Pb - Pb$ collisions at $\sqrt{s} = 2.76$ TeV.

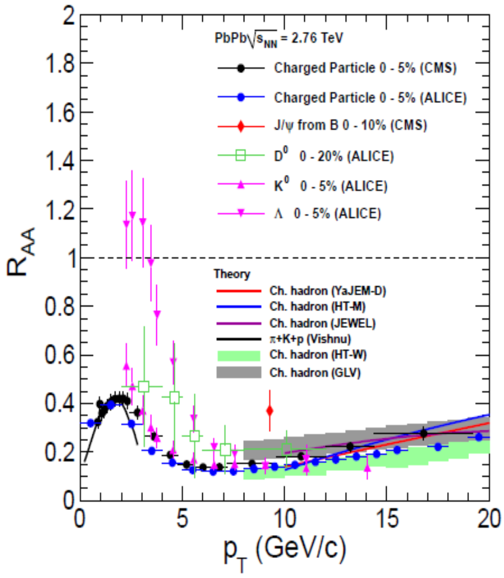

Figure 1.22: Nuclear modification factor measured at LHC for various particles [25].

The strong nuclear attenuation, $R_{AA} \ll 1$, is commonly explained as resulting from jet-quenching, originating from the energy loss of parent partons when crossing the hot medium created in $A-A$ collisions. Schematically, the effect can be described as follows.

The cross section in $p-p$ collisions can be parametrized as (at large enough p_T):

$$\sigma_{pp} \sim \frac{1}{p_T^n} \tag{1.44}$$

with $n \geq 1$. The cross section in $A-A$ can be obtained from the one in $p-p$, but with a shift in p_T that takes into account the energy loss ΔE. Hence, R_{AA} is of the form

$$R_{AA} \sim \frac{d\sigma_{pp}(p_T + \Delta E)/dp_T}{d\sigma_{pp}(p_T)/p_T} \sim \left(\frac{p_T}{p_T + \Delta E}\right)^n \tag{1.45}$$

Naturally at fixed p_T and large ΔE we expect $R_{AA} \ll 1$. At fixed ΔE, we also expect R_{AA} to get closer to 1 when p_T increases.

Anomalous J/ψ suppression

Following the original idea of Matsui and Satz [26], J/ψ is considered as one of the key probes of QGP. Indeed, most of the experiments show a remarkable suppression of J/ψ production in $A-A$ collisions.

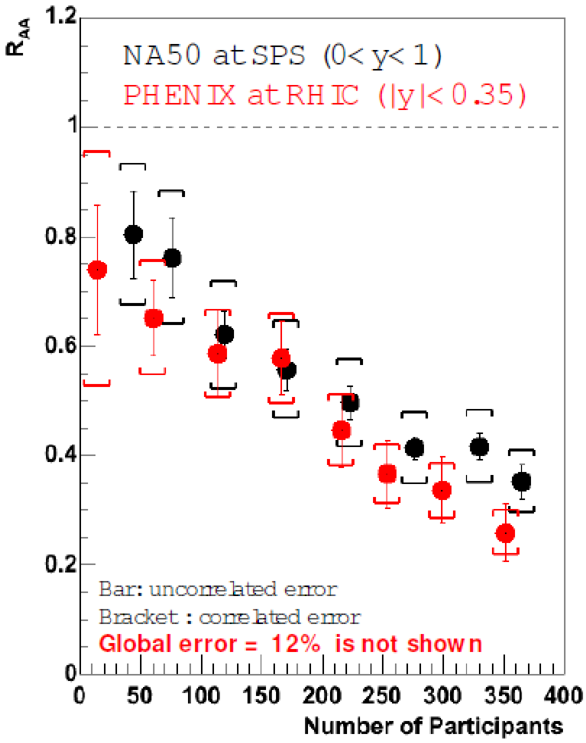

Figure 1.23: NA50 and PHENIX results on J/ψ suppression as a function of number of participants [22].

Although J/ψ production can be calculated via pQCD, studying J/ψ suppression appears to be quite challenging, due to several reasons:

- J/ψ production in $p-p$ collisions is a process that is not very well understood, and is usually described within some models, such as the color evaporation model, color singlet model,... (see Chapter 3). Currently there is no model which is totally satisfactory, neither theoretically nor phenomenologically.
- Several effects, such as absorption, shadowing, energy loss,... (see Chapter 2) can cause the J/ψ suppression already in $p-A$ collisions. Consequently these effects should be also taken into account to understand the suppression in $A-A$.

From now on we will focus on J/ψ production and nuclear suppression. The next Chapters are devoted to present theoretical and phenomenological aspects of those.

CHAPTER 2

Quarkonium production

Contents

2.1 Discovery of quarkonia: brief history

The era of quarkonia has started by the simultaneous discovery of the J/ψ in November 1974 by Ting *et al* at Brookhaven National Laboratory [27] and by Richter *et al* at SLAC [28]. Ting's experiment was based on the high-intensity proton beams of the Alternating Gradient Synchrotron (AGS), which bombarded a fixed target resulting in the production of showers of particles. AGS was working at the energy of 30 GeV. They used a beryllium target and a beam with momentum of 19-20 GeV in the laboratory frame. They detected a strong peak in the energy distribution of the electron-positron pairs at 3.1 GeV. In parallel, Richter's group used an electron-positron storage ring. This group discovered a sharp enhancement of the production cross section in different channels $e^+e^-, \mu^+\mu^-, \pi^+\pi^-$. Richter's group discovered another resonant state with a mass 3.6 GeV which was called ψ'. It was also promptly established that the quantum numbers of the J/ψ were the same as those of the photon, i.e., 1^{--} (here the notation is J^{PC}, where J is the total angular momentum, P is the parity and C the charge conjugation). At SLAC other resonances at 3.415, 3.45 and 3.55 GeV ($\chi_{c0}, \chi_{c1}, \chi_{c2}$) were discovered. Later these states were shown to have $C = +1$. All these particles were attributed to the charmonium family (See Fig. 2.1) of $c\bar{c}$ bound states.

A few years later several $b\bar{b}$ bound states, belonging to the so-called bottomoniun family (See Fig. 2.2), were discovered (1977), with the mass of

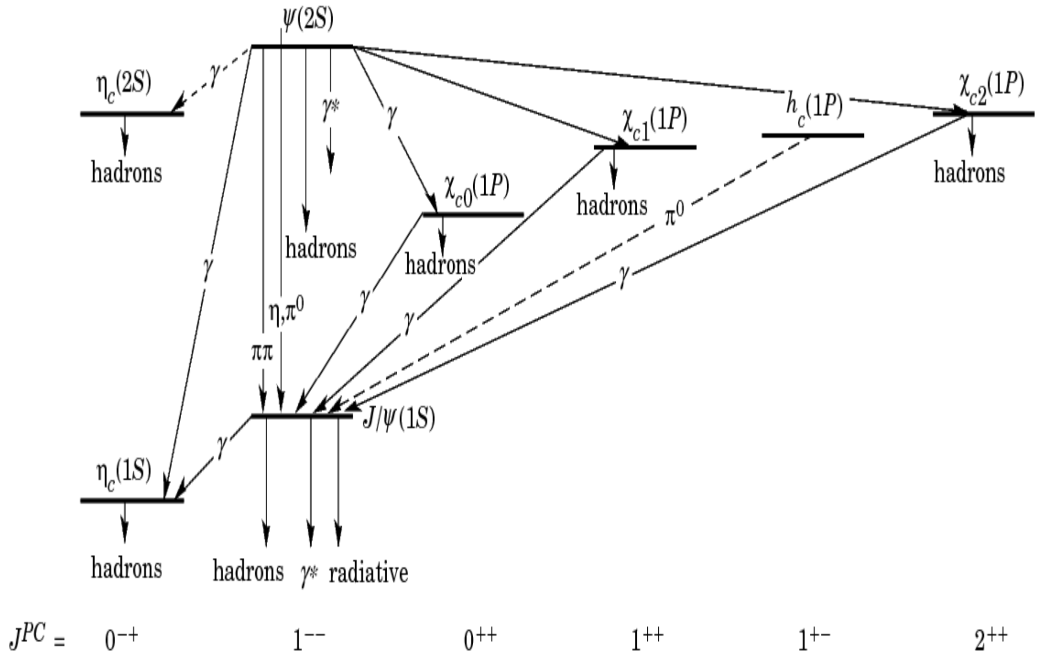

Figure 2.1: Charmonium family.

9.0 GeV ($\Upsilon(1S)$). The first excited state $\Upsilon(2S)$ was directly found thereafter. This was followed by the discovery of $\Upsilon(3S)$ and $\Upsilon(4S)$ states. All of our studies in the coming chapters apply to the J/ψ and $\Upsilon(1S)$ production processes, as well as to the associated excited states (ψ', $\Upsilon(nS)$).

2.2 Quarkonium Production Models

2.2.1 Color Evaporation Model

The color evaporation model (CEM) leads to a similar description of bound and open charm production. According to the CEM, the $c\bar{c}$ pair which will eventually hadronize into the charmonium bound state is produced perturbatively as in open charm production, i.e. via the diagrams shown in Fig. 2.3 (at leading order).

In the CEM, one ignores how the quantum numbers of the quarkoniun bound state are produced. The CEM assumes factorization of the production of the $c\bar{c}$ pair, which is perturbative, and the materialization of this pair into a charmonium state by a mechanism which is non-perturbative [29]. The assumption is reasonable, since the time scales for both processes are different: the time scale for the production of the pair is of order $1/(2m_Q)$, whereas the

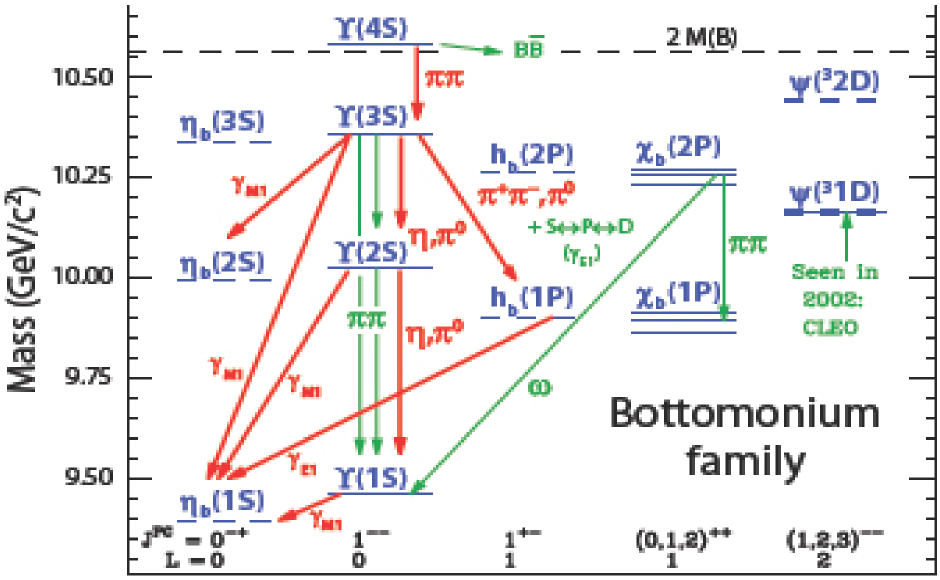

Figure 2.2: Bottomonium family.

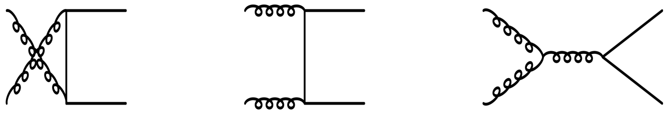

Figure 2.3: Leading order diagrams for quarkonium production in the Color Evaporation Model.

time scale for the formation of the bound state is $1/(M_{\psi'} - M_\psi) \gg 1/(2m_Q)$.

In the CEM, the cross section for charmonium production is calculated as follows:

$$\sigma_{onium} = \frac{1}{9}\int_{2m_c}^{2m_D} dm \frac{d\sigma_{c\bar{c}}}{dm}, \tag{2.1}$$

whereas open charm production is written as

$$\sigma_{open} = \frac{8}{9}\int_{2m_c}^{2m_D} dm \frac{d\sigma_{c\bar{c}}}{dm} + \int_{2m_D}^{\infty} dm \frac{d\sigma_{c\bar{c}}}{dm}. \tag{2.2}$$

Here m is the invariant mass of the $c\bar{c}$ pair. The coefficients $1/9$ and $8/9$ stand for the probability that the $c\bar{c}$ pair is in a color singlet or color octet state. As one can see, the mass of charmonium ranges from $2m_c$ to $2m_D$, where $2m_D$

is the threshold for open charm production. (2.1) is simply interpreted as follows: in the CEM, only those $c\bar{c}$ pairs which are below the threshold and in a color singlet state can hadronize into charmonium. Open charm can arise from an octet $c\bar{c}$ with a mass from $2m_c$ to $2m_D$, and from all $c\bar{c}$ pairs with a mass higher than $2m_D$.

The cross sections given above are calculated perturbatively. (2.1) represents the sum of the cross sections of all charmonia, which is unfortunately difficult to access experimentally, since it requires measuring the cross section for all charmonium bound states at a given energy.

To obtain the production cross section of a given state ψ within the CEM, we need to know the fraction ρ_ψ of $c\bar{c}$ pairs that materializes into the state ψ:

$$\sigma_\psi = \rho_\psi \, \sigma_{onium} \tag{2.3}$$

One should mention that the coefficient ρ_ψ is assumed to be the same for photo and hadro-production. This is due to the fact that ρ_ψ describes the probability for the produced $c\bar{c}$ pair to evolve into a given bound state ψ, and should therefore not depend on the projectile type.

The factorization between the production of the $c\bar{c}$ pair and bound state formation implies that the energy dependence and kinematic distributions of the measured cross sections for different bound states should be similar. Moreover, in the approximation $m_c \approx m_D$ this equivalence extends to the production of open $D\bar{D}$ pairs. In the figure 2.4 one can see the photoproduction data for both open charm and bound state production with common normalization in order to show their identical behaviour. In the Fig.2.4 the data for total production cross sections is taken from Fermilab E687 collaboration [30]. This collaboration studied in detail photoproduction of charmonium and open charm via $\gamma - N$ collisions. The photon beam was initiated by a proton beam of 800 GeV colliding with a berylium target.

Fig.2.5 gives from the results of NA25 experiment [32] for the total cross section in p-N interactions. Incident protons have an energy from 200 to 360 GeV.

Figs. 2.4 and 2.5 show the similarity between the $D\bar{D}$ and the bound state cross sections, which makes the assumption of the CEM reasonable.

2.2.2 Color Singlet Model

This model is the most natural application of QCD to heavy quarkonium production in the high energy limit. The model is inspired by the factorization theorems of QCD.

The main postulates of the model are as follows:

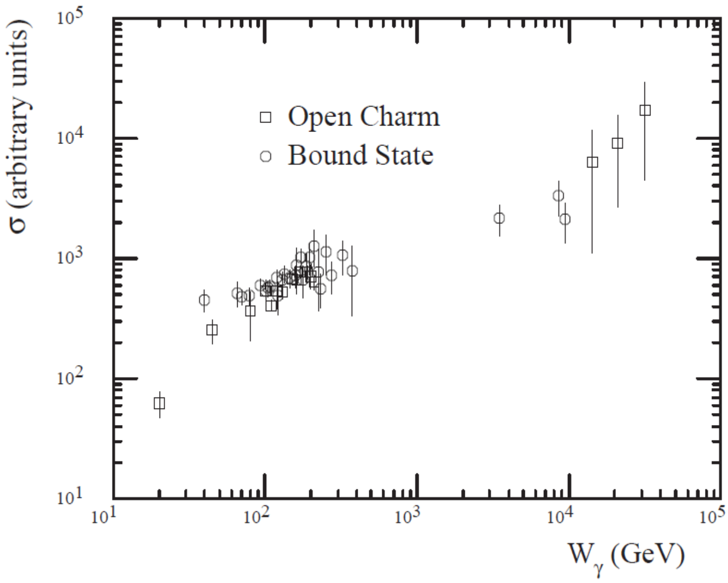

Figure 2.4: Photoproduction data for open charm and bound state production as a function of the photon energy W_γ in the hadron rest frame [30], [31].

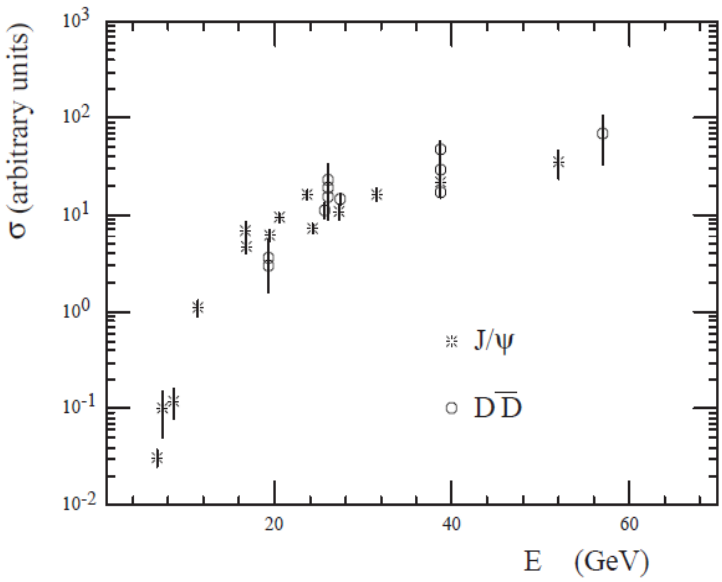

Figure 2.5: Hadroproduction data for $\sigma(D\bar{D})$ and $\sigma(J/\psi)$ as a function of the center-of-mass energy E_{cm} [32], [33].

- Decompose the quarkonium production in 2 steps (as in Fig. 2.6)

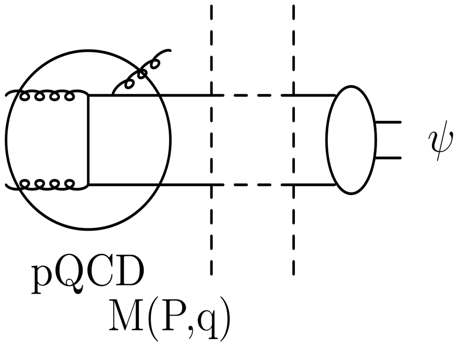

Figure 2.6: Quarkonium production in the CSM.

a) creation of 2 on-shell quasi-collinear heavy quarks (Q and $\bar{Q}$)

b) their binding to make a quarkonium

One postulates the factorization of these two processes.

- The scale of the first process is $\sim O(M)$ where $M \simeq 2m_Q \gg \Lambda$, and is therefore considered as perturbative.
- Since we consider only a bound state of heavy quarks ($c\bar{c}$ or $b\bar{b}$), their relative velocity in the bound state is small.
- The pair is produced perturbatively with the quantum numbers of the final bound state, in particular it is produced in a color-singlet state (hence the name CSM).

The production amplitude of the state with the quantum numbers of J/ψ is given by [34]:

$$A(P) = \int \frac{d^4q}{(2\pi)^4} Tr[M(P,q)\Phi(P,q)] \tag{2.4}$$

Here, $\Phi(P,q)$ is the wave function of the bound state, $M(P,q)$ is the perturbative part of the process (with heavy quark legs cut off). Heavy quark spinors $u(\frac{1}{2}P+q,s)$ and $\bar{v}(\frac{1}{2}P-q,\bar{s})$ are included in $\Phi(P,q)$. P is the four-momentum of the bound state, $2q$ relative momentum and $s(\bar{s})$ spin.

Let us consider a non-relativistic bound state. In this case the relative momentum $|\vec{q}|$ is small compared to the quark mass m_Q. Due to small $|\vec{q}|$ one can decompose the wave function of the bound state with spin S, orbital angular momentum L and total angular momentum J as the following :

$$\Phi(P,q) = 2\pi\delta\left(q^0 - \frac{|q^2|}{2m_Q}\right) \sum_{L_z,S_z} \psi_{LL_z}(\vec{q}) < LL_z; SS_z|JJ_z > P_{ss_t}(P,q) \tag{2.5}$$

Here, P_{ss_t} is a projection operator, defined as :

$$P_{ss_t}(P,q) = \sum_{s\bar{s}} < \frac{1}{2}s_i\frac{1}{2}\bar{s}|ss_t > u\left(\frac{P}{2}+q,s\right)\bar{v}\left(\frac{P}{2}-q,\bar{s}\right) \tag{2.6}$$

If we put the expanded expression of the wave function into the initial expression for the amplitude, we get:

$$A(P) = \sum_{L_z,S_z}\int\frac{d^3q}{(2\pi)^3}\psi_{LL_z}(\vec{q}) < LL_z;SS_z|JJ_z > Tr[M(P,q)P_{ss_t}(P,q)] \tag{2.7}$$

We can expand the latter expression in $\vec{q}$ and keep only non-vanishing terms. For a vector ($S=1$) and S-wave ($L=0$) state like J/ψ we have:

$$A(p) = \frac{1}{\sqrt{4\pi}}R_0\,Tr[M(P,0)P_{ss_t}(P,0)] \tag{2.8}$$

$$\frac{1}{\sqrt{4\pi}}R_0 = \int\frac{d^3q}{(2\pi)^3}\psi_{00}(\vec{q}) \tag{2.9}$$

Here R_0 is the value of the S-wave function at the origin; for P-waves one has to go a step further in the expansion of the trace in (2.7).

Intuitively (2.8) can be understood from the shapes of the wave functions describing the perturbative process and the bound state, see Fig. 2.7. The wave function of a bound state is more narrow and has a width of the order of $\alpha_s m_Q$, whereas the wave function of the perturbative process is broader with a width of order m_Q.

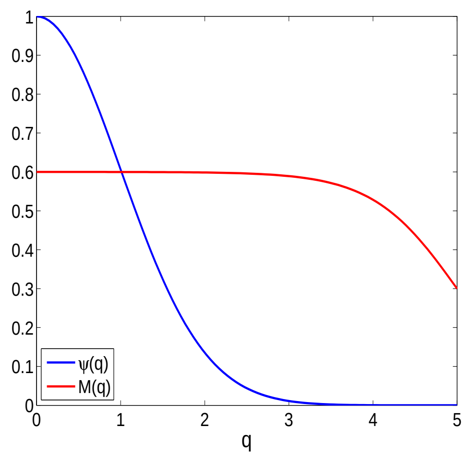

Figure 2.7: The wave functions describing the perturbative part of the process and the bound state.

In Figs. 2.8, 2.9 one can see the prediction done for J/ψ and ψ' production in $p-\bar{p}$ collisions within the CSM model. We see that the CSM underestimates the cross section $d\sigma/p_T$ by more than one order of magnitude.

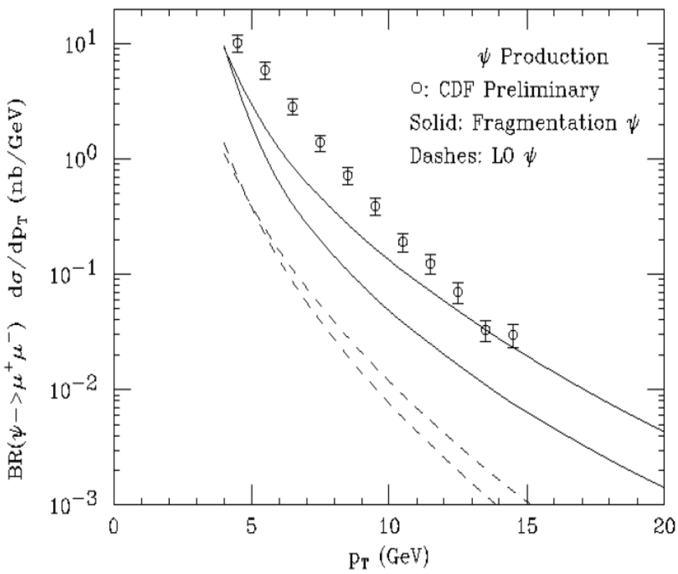

Figure 2.8: J/ψ cross section calculated in the CSM, compared to the CDF data [35].

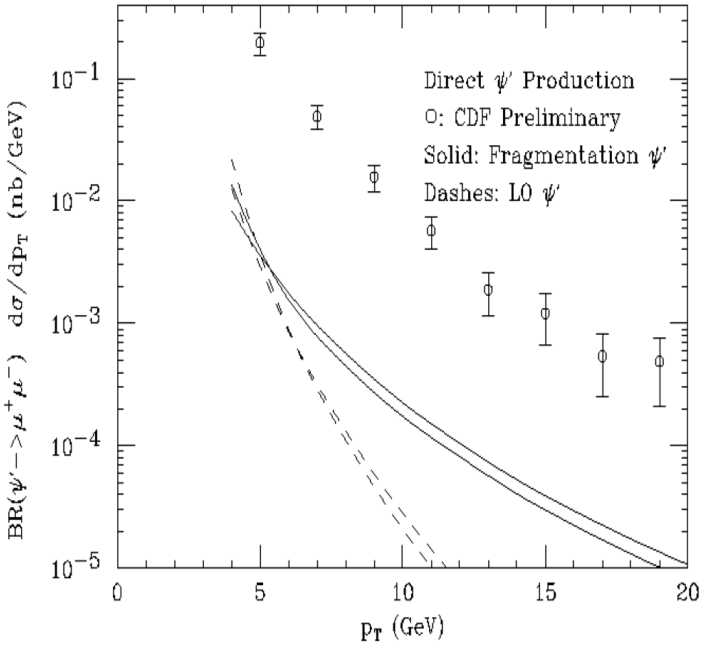

Figure 2.9: ψ' cross section calculated in the CSM, compared to the CDF data [35].

Recently it has been argued that higher order corrections might enhance the J/ψ (or Υ) production rate in the CSM [36]. However we see on Fig. 2.10 that the full NLO CSM rate is still below the data. The NNLO* calculation includes only part of the NNLO contributions: it misses virtual corrections and thus most probably overestimates the true NNLO rate.

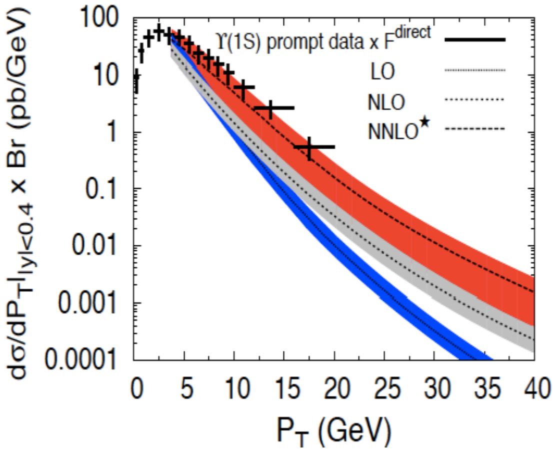

Figure 2.10: Comparison done between different contributions of CSM and experimental data for $\Upsilon(1S)$ production

The polarisation state can be deduced from the angular dependence of its decay into $\mu^+\mu^-$. One needs to measure the normalized angular distribution given by:

$$I(\cos\theta) = \frac{3}{2(\alpha+3)}(1+\alpha\cos^2\theta) \tag{2.10}$$

The angle θ is defined as the angle between the direction of J/ψ in the lab frame and the μ^+ direction in the quarkonium rest frame. In (2.10) the important quantity is:

$$\alpha = \frac{\frac{1}{2}\sigma_T - \sigma_L}{\frac{1}{2}\sigma_T + \sigma_L} \tag{2.11}$$

$\alpha = 0$ means that the quarkonium is unpolarized (i.e., $\sigma_T = 2\sigma_L$), $\alpha = +1$ stands for pure transverse polarization ($\sigma_L = 0$) and $\alpha = -1$ for longitunal ($\sigma_T = 0$).

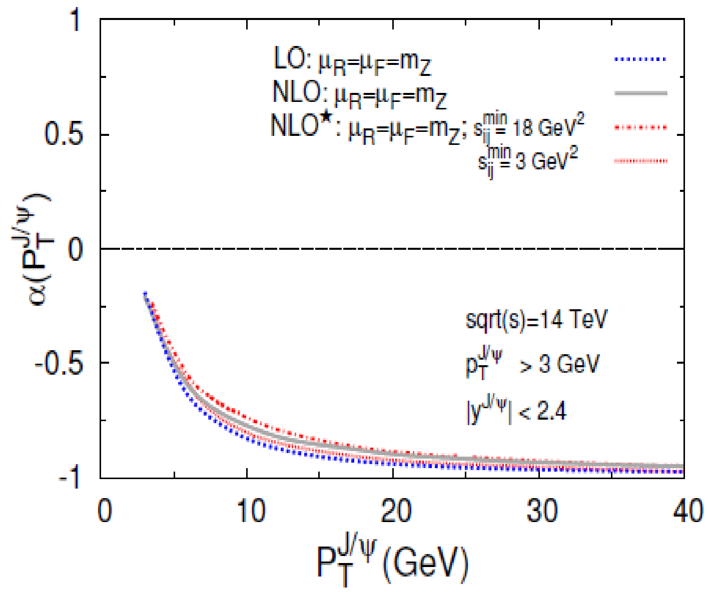

Figure 2.11: p_T dependence of the polarization of direct J/ψ production at LO, NLO, NLO* at $\sqrt{s} = 14$ TeV [35].

The CSM predicts a longitudinal polarization for J/ψ, ψ' (Fig. 2.11) whereas experiment doesn't show any evidence of it (Fig. 2.12).

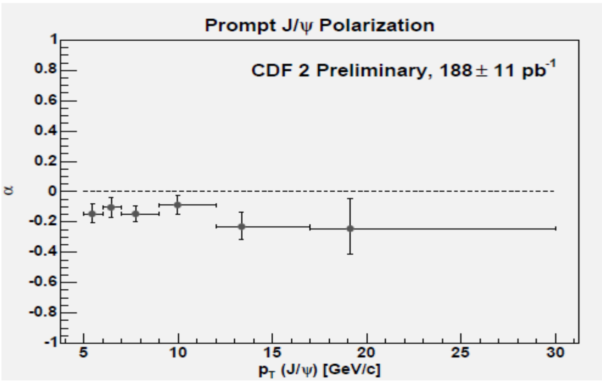

Figure 2.12: Preliminary measurement of the prompt J/ψ polarization as measured by CDF [35].

Although Fig.2.12 includes J/ψ from χ_c decays, it is difficult to imagine how removing this contribution could yield a longitudinal polarization for direct J/ψ, as predicted by the CSM (Fig.2.11).

In summary, the CSM fails to describe quarkonium production, at least at large p_T in $p-p$ collisions. Despite its simplicity the CSM model is not satisfactory.

2.2.3 Color Octet Model

The theoretical evidence for the incompleteness of the color singlet model comes from the presence of infrared divergencies in the production cross sections and decay rates of P-wave quarkonium states calculated in the CSM.

Similarly to the quarkonium production, quarkonium decays can be also used to test various models. As an example, let us consider the decay of χ-states. The problem with the CSM is that singularities are present in certain amplitudes, see Fig. 2.13. This problem is resolved by taking into account the component of the χ state wavefunction consisting of a color octet $c\bar{c}$ pair and a gluon, see Fig.2.14.

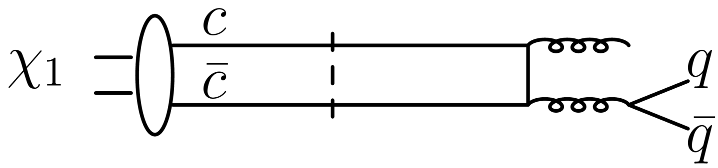

Figure 2.13: χ_1 decay in the Color Singlet Model.

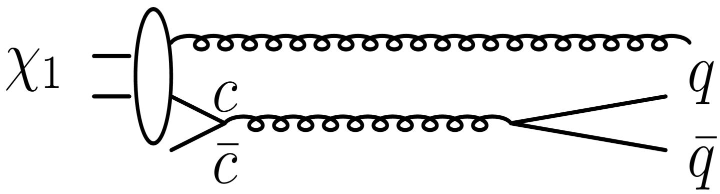

Figure 2.14: Additional contribution to χ_1 decay in the Color Octet Model.

The NRQCD (non-relativistic quantum chromodynamics) formalism implies that so called color octet processes associated with higher Fock components of the quarkonium wave function must contribute to the cross section.

Within the framework of NRQCD, the cross section for producing a quarkonium state H can be expressed as a sum of terms, each of which factors into a short-distance coefficient and a long-distance matrix element [37]:

$$d\sigma(H+X) = \sum_n d\hat{\sigma}(Q\bar{Q}[n]+X)\langle O^H[n]\rangle \tag{2.12}$$

The sum includes all color and angular momentum states of the $Q\bar{Q}$ pair, denoted collectively by n. The short-distance coefficients are proportional to the cross sections for producing a $Q\bar{Q}$ pair in the state n and with a small relative momentum. They can be calculated perturbatively. The term $\langle O^H[n]\rangle$ stands for the non-perturbative transition probability from the $Q\bar{Q}$ state n into the quarkonium H.

The main feature of this model is an introduction of dynamical gluons in the Fock-state decomposition of the physical quarkonium states:

$$|H\rangle = \psi^H_{Q\bar{Q}}|Q\bar{Q}\rangle + \psi^H_{Q\bar{Q}g}|Q\bar{Q}g\rangle + ... \tag{2.13}$$

The dominant component $|Q\bar{Q}\rangle$ consists of a heavy quark pair in a color-singlet state and with quantum numbers ${}^{2S+1}L_J$ consistent with the quantum numbers of the physical quarkonium. The higher Fock states contain dynamical gluons or light $q\bar{q}$ pairs. The heavy quark pair can be in either a color-singlet or a color-octet state with spin $S = 0, 1$ and angular momentum $L = 0, 1, 2, ...$ All higher Fock states have probabilities suppressed by powers of v (the relative velocity of the heavy quarks in the bound state).

The different contributions to the J/ψ transverse momentum distribution are compared to the CDF data in Fig.2.15 [37].

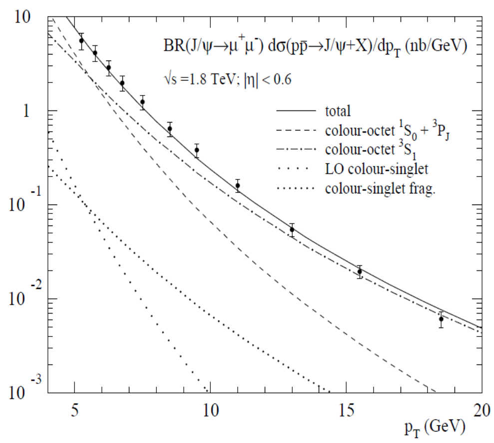

Figure 2.15: Color-singlet and color-octet contributions to direct J/ψ production in $p\bar{p} \to J/\psi + X$ at $\sqrt{s} = 1.8$ TeV [37].

The CDF results can be fitted by including the leading color-octet contributions $c\bar{c}[8, {}^1S_0], c\bar{c}[8, {}^3S_1]$ and $c\bar{c}[8, {}^3P_J]$, and adjusting the corresponding non-perturbative parameters.

The polarization of J/ψ and $\psi(2S)$ at large transverse momentum is one crucial test of the NRQCD approach. The data for J/ψ polarization has been compared to NRQCD predictions, see Fig.2.16.

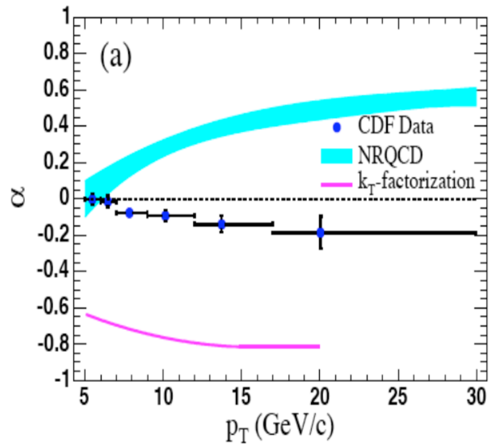

Figure 2.16: The polarization parameter α calculated in NRQCD, and comparison with CDF data [38].

One observes that the NRQCD prediction for polarization fails.

2.2.4 PQCD factorization approach

The following approach was proposed by Nayak, Qiu, Sterman (NQS) [39].

Consider the process $A + B \to H(p_T) + X$ at large $p_T \gg m_c$. To leading power in $m_c/p_T \ll 1$, the production proceeds through gluon fragmentation, and the process factorizes as:

$$d\sigma_{A+B\to H+X}(p_T) = d\hat{\sigma}_{A+B\to g+X}(p_T/z\mu) \otimes D_{H/g}(z, m_c, \mu) + O(m_c^2/p_T^2) \quad (2.14)$$

Here the factorization scale μ is of order p_T. All the information on the initial state is given by $d\hat{\sigma}_{A+B\to g+X}$. If we assume NRQCD factorization,

$$d\sigma_{A+B\to H+X}(p_T) = \sum_n \hat{\sigma}_{A+B\to c\bar{c}[n]+X}(p_T)\langle O_n^H\rangle \quad (2.15)$$

The fragmentation function should be related to the NRQCD operators as the following:

$$D_{H/g}(z, m_c, \mu) = \sum_n d_{g\to c\bar{c}[n]}(z, \mu, m_c)\langle O_n^H\rangle \quad (2.16)$$

where $d_{g\to c\bar{c}[n]}(z, \mu, m_c)$ describes the evolution of the off-shell gluon into a quark pair in state $[n]$, including logarithms of μ/m_c.

The recent works of (NQS) attempt to prove rigorously that the gluon fragmentation function $D_{H/g}$ factorizes as in (2.16), as postulated within the COM. Even if this attempt turns out to be successful, let us stress the "PQCD factorization approach" holds in the large p_T limit, $p_T \gg m_c$.

CHAPTER 3

Phenomenology of J/ψ suppression in $p - A$ collisions

Contents

3.1 Data for J/ψ suppression

Various experiments measured J/ψ suppression in $p - A$ collisions. Before going to the proposed theoretical explanations of this phenomenon, let us mention some of the experiments. I will list the experiments in historical order. For a better understanding of the experimental data, one must introduce the major quantities that will be referred to in this section:

- R_{pA}: nuclear modification factor, defined as the ratio of the cross section measured in p-A collisions and the cross section measured in p-p, normalized by the atomic mass A

$$R_{pA} = \frac{1}{A}\frac{d\sigma_{pA}/dx_F}{d\sigma_{pp}/dx_F} \tag{3.1}$$

- x_F: Feynman x, defined as the ratio of the longitudinal momentum of the detected particle over the longitudinal momentum of the projectile in the center of mass frame:

$$x_F = \frac{p'_{||}}{p'_{p||}} \tag{3.2}$$

  The prime upperscript denotes the momentum in the center of mass frame.

- α: parameter showing the atomic mass number dependence of the cross section measured in $p - A$ collisions:

$$\sigma_A = \sigma_N A^{\alpha} \tag{3.3}$$

- The collision energy $\sqrt{s}$ is related to the projectile energy E_p in the nucleus rest frame as $s \simeq 2m_pE_p$.

3.1.1 J/ψ suppression in NA3 experiment

The NA3 collaboration made measurements as a part of SPS experiment (located at CERN, operated between 1981-1984). Data have been taken with incident $\pi^{\pm}$,$K^{\pm}$ and $p^{\pm}$ on hydrogen and platinum targets at 150, 200, 280 GeV/c [60]. In Fig. 3.1, one can see the results obtained for $\mathrm{p-Pt}$ and $\pi^{-} - \mathrm{Pt}$ collisions at various $\sqrt{s}$.

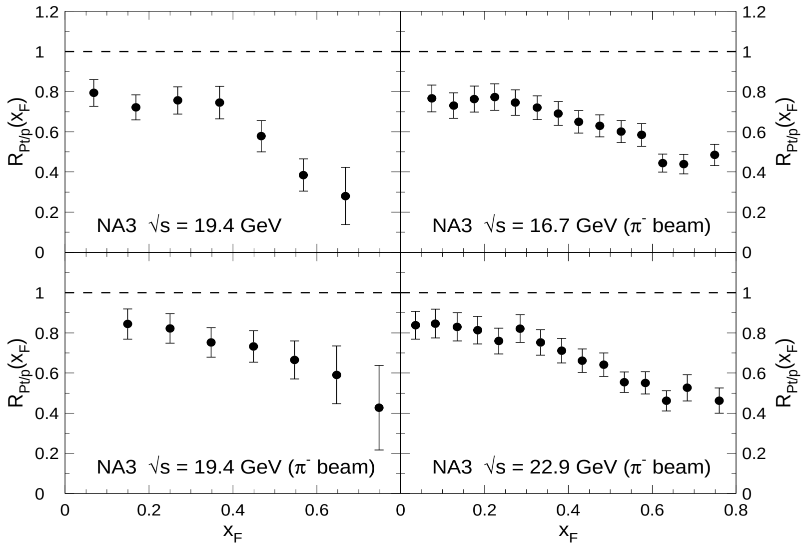

Figure 3.1: J/ψ suppression as a function of x_F in NA3 experiment [60]. The upper left panel is for a proton beam, the other panels for π^- beam.

At that time, people were surprised to observe a suppression at $x_F \to 1$. In [60] it is supposed that it might be either due to interactions in the initial state (diffusion of the π^- or p in the heavy nucleus) or to the interactions in the final state (ψ-nucleon diffusion).

3.1.2 E866

Fermilab E866 experiment is a fixed target experiment where proton beams have been bombarded to various nuclei: B, Fe, W [66]. The measurement of J/ψ suppression in nuclei was made over a broad range in x_F (from -0.10 to 0.93) and p_T (up to 4 GeV). The plots of J/ψ and ψ' suppression in terms of x_F are shown in Figs. 3.2 and 3.3.

As one can see, the coefficient α is largest at values of x_F of 0.25 and below, but strongly decreases at larger values of x_F. For the ψ' α is smaller than for J/ψ for $x_F < 0.2$, it remains relatively constant up to x_F of 0.3-0.4 and then falls to values consistent with those for the J/ψ.

In Fig. 3.2 one also observes a comparison with the data from E772 experiment. This experiment runned at 800 GeV, but had a limited acceptance in p_T which varied with x_F. This manifests itself in the values of α which drop at small x_F below the values obtained in E866.

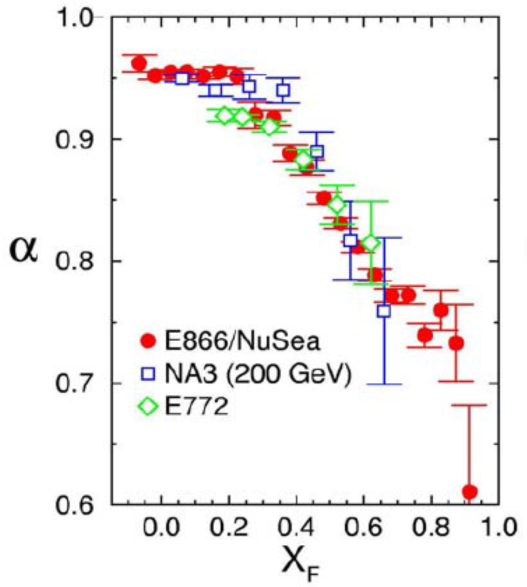

Figure 3.2: J/ψ suppression as a function of x_F. The E866 data is from Ref. [66].

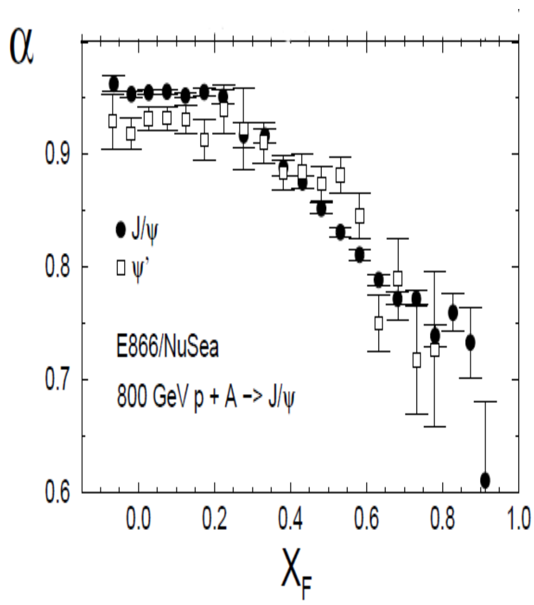

Figure 3.3: ψ' suppression as a function of x_F. The E688 data for ψ' is from Ref. [66].

3.1.3 RHIC

The Relativistic Heavy Ion Collider (RHIC) is operating in Brookhaven. In 2003 RHIC collided deuterium and gold nuclei at $\sqrt{s} = 200$ GeV, corresponding to $E_p \simeq 22$ TeV. The J/ψ was measured from its dielectron (dimuon) decays at forward, backward and mid rapidities. At mid rapidity ($|y| < 0.35$) J/ψ is measured via decay into electrons, at backward ($-2.2 < y < -1.2$) and forward ($1.2 < y < 2.2$) rapidities via decay into muons [42]. The rapidity is related to x_F as follows:

$$x_F = \frac{2M_\perp \sinh y}{\sqrt{s}}, \tag{3.4}$$

where $M_\perp$ is the transverse mass, defined as $M_\perp = \sqrt{M^2 + p_\perp^2}$. From (3.4) one can calculate the range of RHIC in x_F, which is (-0.16, 0.16).

In Fig. 3.4 I show the results obtained for the nuclear modification factor calculated by comparing the J/ψ production cross section measured in d-Au collisions with the one measured in p-p.

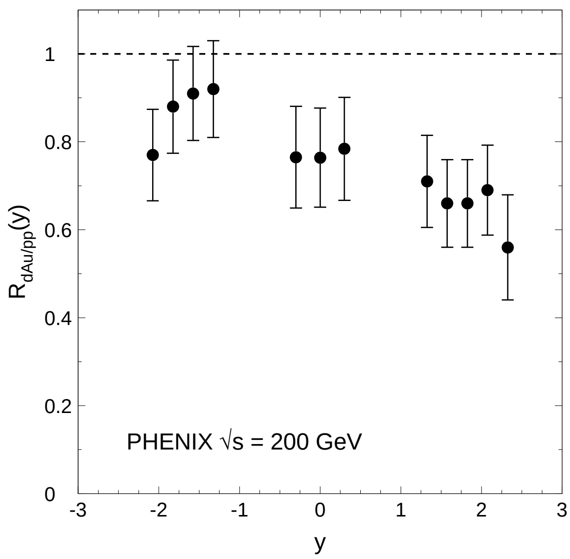

Figure 3.4: J/ψ suppression observed at RHIC by the PHENIX collaboration [68].

The suppression of J/ψ in cold matter is observed as one goes forward in rapidity, in the direction of the deuteron.

3.1.4 LHC

The Large Hadron Collider (LHC) is the world's largest and highest-energy particle accelerator, which lies beneath the Franco-Swiss border, close to Geneva, Switzerland. It is designed to collide two opposite beams of particles up to $\sqrt{s} = 14$ TeV. Three out of four experiments (ALICE, ATLAS and CMS) participate in the LHC nuclear beam program.

Recently the preliminary results of the ALICE experiment have been presented. Quarkonium in ALICE can be measured in two ways, at midrapidity ($|y| < 0.9$) via $J/\psi \to e^+e^-$, and at forward rapidities ($2.5 < y < 4$) via $J/\psi \to \mu^+\mu^-$. Data have been collected for two beam configurations: $p - Pb$, and $Pb - p$, in the range $2.5 < y < 4$. The collision in p-A collisions is $\sqrt{s} = 5.02$ TeV. The preliminary data is shown in Fig. 3.5, with theoretical curves standing for various models .

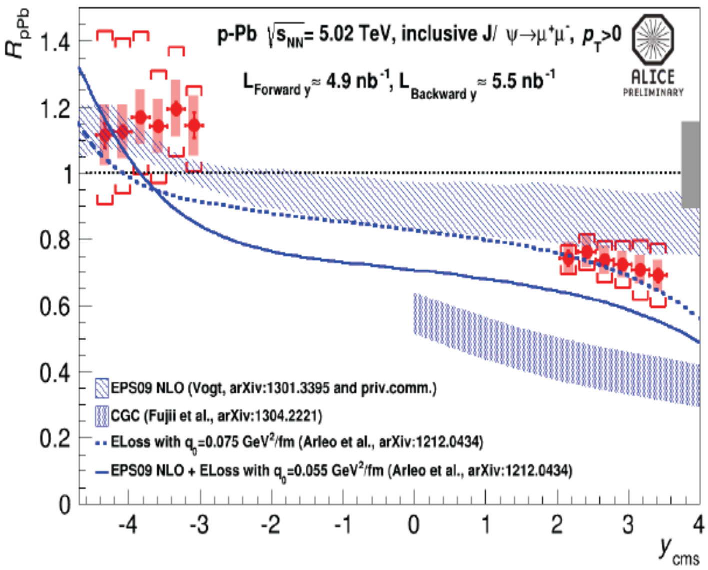

Figure 3.5: Preliminary data for J/ψ suppression at LHC, as measured by the ALICE collaboration

As one can see, a larger suppression of the J/ψ yield is observed for the largest rapidities $2.03 < y_{cms} < 3.53$.

3.2 Various cold nuclear effects

The observed J/ψ suppression initiated studies of various effects. Several mechanisms, like nuclear absorption, shadowing, energy loss, etc., can contribute to J/ψ suppression.

3.2.1 Nuclear Absorption

If the J/ψ is formed in the nucleus it may interact with nucleons and be dissociated before it can escape the target. This happens when the J/ψ hadronization time t_{had} is smaller than the nuclear size $\sim L$ (Fig. 3.6),

$$t_{had} \sim \frac{E}{M} \cdot \tau_{had} \leq L \tag{3.5}$$

i.e., when the J/ψ energy E (in the nucleus rest frame) goes below the critical value.

$$E_{cr} = M \cdot \frac{L}{\tau_{had}} \tag{3.6}$$

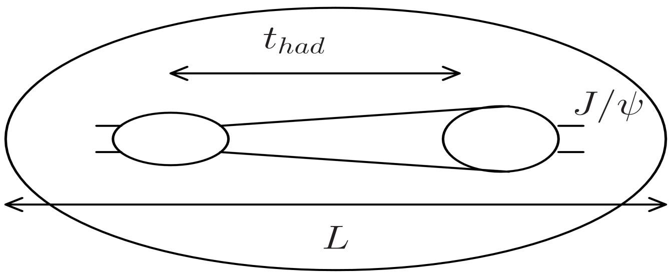

Figure 3.6: J/ψ production inside the nucleus.

The proper hadronization time τ_{had} is given by the mass splitting between $1S$ and $2S$ states,

$$\tau_{\psi} = (M_{\psi} - M_{J/\psi})^{-1} \simeq (0.6\text{GeV})^{-1} = 0.3\text{fm} \tag{3.7}$$

Putting it back to (3.6), with L calculated for tungsten, one obtains 85 GeV for E_{cr}. Knowing $E_{cr}(x_F)$ one can easily calculate the x_F^{crit}, by using the explicit expression for x_F as a function of E,

$$x_F(E) = \frac{E}{E_p} - \frac{E_p}{E}\frac{M_{\perp}^2}{s} \tag{3.8}$$

For $E_p = 800$ GeV, we have $x_F^{crit} = x_F(E_{cr}) \simeq 0.03$. The higher E_p the smaller x_F, thus at very high E_p (or $\sqrt{s}$), the effect of J/ψ nuclear dissociation will play a role only at negative values of x_F.

The effect of nuclear absorption alone on the J/ψ production cross section in $p-A$ can be expressed as [44]:

$$\begin{aligned}\sigma_{pA} &= \sigma_{pN}\int d^2b\int_{-\infty}^{+\infty} dz\rho_A(b,z)S^{abs}(b)\\ &= \sigma_{pN}\int d^2b\int_{-\infty}^{+\infty} dz\rho_A(b,z)exp\{-\int_z^{\infty} dz'\rho_A(b,z')\sigma_{abs}(z'-z)\}\end{aligned} \quad (3.9)$$

Here z is the longitudinal position of the production point, z' the position at which the state is absorbed, b is the impact parameter, S^{abs} the nuclear absorption survival probability defined as $\exp\left\{-\int_z^{\infty} dz'\rho_A(b,z')\sigma_{abs}(z'-z)\right\}$ and σ_{abs} the charmonium nuclear absorption cross section. Nuclear charge distributions from data are used for ρ.

There were attempts to apply the formula above to the case when the J/ψ energy is relatively high, and the J/ψ fragments outside of the nucleus [44], See Fig. 3.7.

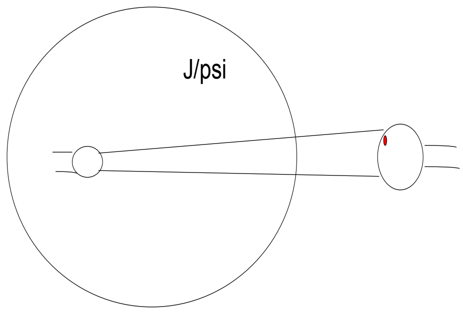

Figure 3.7: J/ψ production outside of the nucleus

In this case (corresponding to $E > E_{cr}$), what travels through the nucleus is a $c\bar{c}$ pair, and the J/ψ absorption cross section σ_{abs} becomes irrelevant. The models using (3.9) in the domain $E > E_{cr}$ thus assume that the $q\bar{q}$ pair at high energies can be "absorbed" in the same way as the J/ψ at low energies. The parameter σ_{abs} is then interpreted as an effective absorption cross section for the $c\bar{c}$ pair. In this case nuclear absorption depends on the production mechanism of the $c\bar{c}$. I will mention the cases of color singlet, color octet and a mixture of color singlet and octet $c\bar{c}$ considered in [44].

In the latter paper, the authors assume that in the color octet model the initial state of $c\bar{c}$ pair is the same for all resonances, hence the absorption probability is the same for all of them. The situation is a little different in the color singlet model. The $c\bar{c}$ pair is produced with the production time $\tau \propto m_c^{-1}$, whereas the proper production time of the final charmonium is considerably longer. The absorption cross section is expected to grow as a function of the proper time, until it saturates at τ_{ψ_i}. More realistically ψ is produced as a combination of singlet and octet states, as in NRQCD. In this case the cross section is calculated like this:

$$\frac{d\sigma_{pA}^{\psi}}{dx_F} = \frac{d\sigma_{pp}^{\psi_{oct}}}{dx_F} \int d^2bdzS_{oct}^{abs}(b) + \frac{d\sigma_{pp}^{\psi_{sing}}}{dx_F} \int d^2bdzS_{sing}^{abs}(b) \tag{3.10}$$

In Fig. 3.8 one can see the predictions done for $E_p = 800$ GeV for color octet and mixed states of ψ and ψ' states. The predictions done by [44] for color

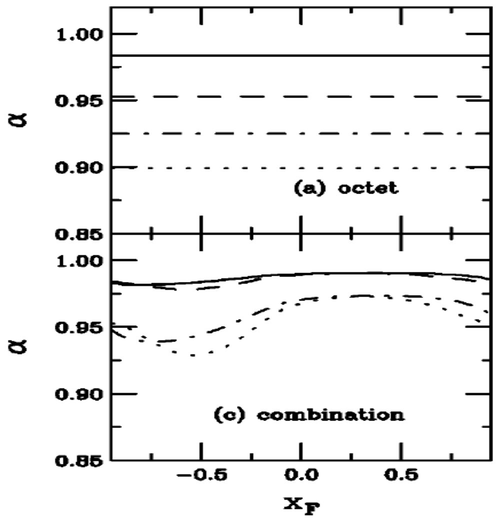

Figure 3.8: The A dependence of nuclear absorption models is given in (a) octet cross sections of 1 mb (solid), 3 mb (dashed), 5 mb (dot-dashed), and 7 mb (dotted) are shown. A combination of octet and singlet production is assumed in (c). The curves represent ψ nucleus suppression due to an effective absorption cross section of the $c\bar{c}$ pair, with $\sigma_{abs}^{oct} = 1$mb and $\sigma_{abs}^{sing} = 1$ mb (solid) and $\sigma_{abs}^{oct} = 3$ and $\sigma_{abs}^{sing} = 5$ mb (dot-dashed). The authors of this model considered the absorption of $c\bar{c}$.

singlet model can be found on Fig.3.9. As one can see the x_F dependence of nuclear suppression appears mostly at negative x_F.

In Figs. 3.8, 3.9 we see that for $x_F > x_F^{crit}$, $\sigma_{abs}^{c\bar{c}}$ gives a moderate suppression and cannot explain, even qualitatively, the strong suppression seen in the data when x_F increases.

3.2.2 Shadowing

Structure functions of nuclei are different from the superposition of those of their constituents. The nuclear structure function F_2 per nucleon divided by

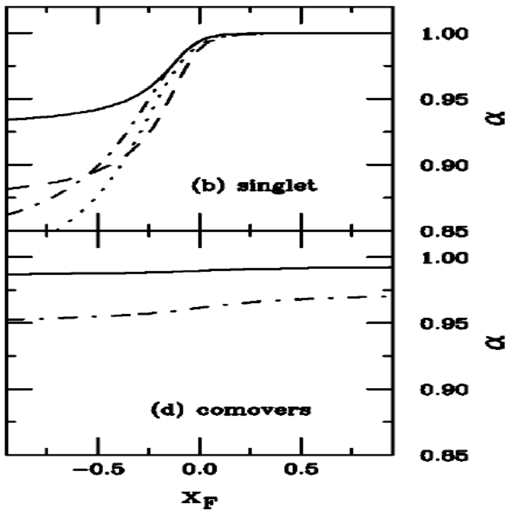

Figure 3.9: Singlet absorption is shown in (b) for cross sections of 5 mb (solid) and 10 mb (dashed).

the nucleon structure function,

$$R^A_{F_2}(x, Q^2) = \frac{F^A_2(x, Q^2)}{AF^{nucleon}_2(x, Q^2)} \tag{3.11}$$

quantifies this difference. x, Q^2 are the standard variables used in DIS. $F^{nucleon}_2$ is usually defined through the measurements of deuterium $F^{nucleon}_2 = F^{deuterium}_2/2$ assuming that nuclear effects are negligible in deuterium. The behaviour of $R^A_{F_2}$ as a function of x is represented schematically in Fig.3.10. The figure

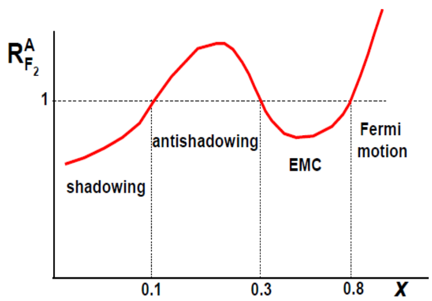

Figure 3.10: Schematic behaviour of $R^A_{F_2}(x, Q^2)$ as a function of x for a given Q^2

3.10 can be divided into four regions [45]:

- $R_{F_2} > 1$ for $x > 0.8$: the Fermi motion region.

- $R^A_{F_2} < 1$ for $0.25 \lesssim x \lesssim 0.8$: the EMC region (European Muon Collaboration)
- $R^A_{F_2} > 1$, $0.1 \lesssim x \lesssim 0.3$-the antishadowing region.
- $R^A_{F_2} < 1$ for $x \lesssim 0.1$ is the shadowing region. Existing data indicates that shadowing increases when x decreases, increases with A, and decreases with increasing Q^2.

In high-energy p-A collisions, cross section are dominated by small values of x_2, i.e., they are sensitive to the shadowing region of the nuclear PDF. We thus focus on this region in the following, sketching the physical origin of shadowing.

Deep inelastic scattering, schematically depicted in Fig.3.11.

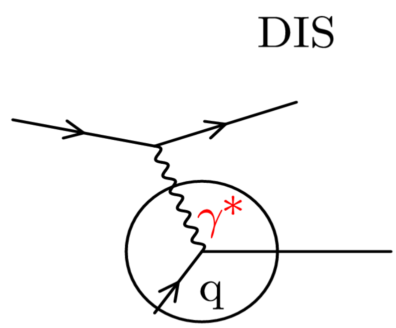

Figure 3.11: Deep inelastic scattering.

In most approaches the origin of the nuclear depletion in the region of small x and moderate Q^2 is related to the fact that the hadronic component of the photon interacts several times with different nucleons of the nucleus. In a partonic language, shadowing can be simply understood as follows. In the nucleus rest frame, the fluctuation $\gamma* \to q\bar{q}$ has a lifetime

$$t_f \sim \frac{\nu}{Q^2} = \frac{1}{2m_N x} \tag{3.12}$$

which becomes large at small x. Before undergoing a hard scattering on a nucleon N_2, the $q\bar{q}$ pair can undergo an elastic scattering on a nucleon N_1. This gives the possibility of an interference such as depicted in Fig. 3.12, which contributes negatively to the DIS cross section. Effectively, the nuclear PDF (normalized by A) is reduced compared to the nuclear PDF.

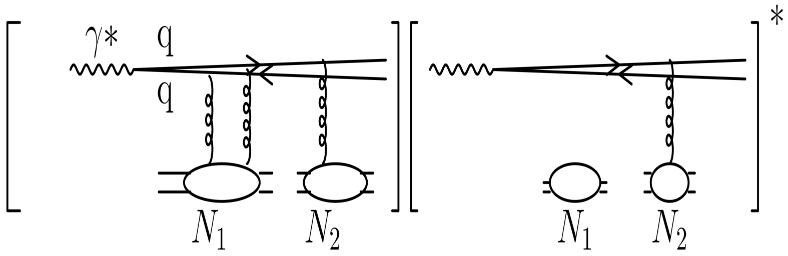

Figure 3.12: $q\bar{q}$ fluctuation of the incoming photon interacting with target nucleons.

Shadowing can be modelled by an A dependent fit to the deep-inelastic scattering data [44]. The most common assumption is that nuclear parton distributions factorize into the nucleon PDF's, independent of A, and a shadowing function that parametrizes the modifications of the nucleon parton densities in the nucleus, which depend on A, x, and Q^2.

$$f_i^A(x, Q^2, A) = S^i(A, x, Q^2) f_i^P(x, Q^2) \tag{3.13}$$

Below I list the plots of one model (see Figs. 3.13, 3.14, 3.15). The prediction was made assuming the shadowing function is the same for quarks, gluons and antiquarks. Also no dependence on Q^2 is taken into account [44]. In Fig. 3.13, the shadowing function was estimated for $A = 184$ and $A = 9$. The antishadowing is rather small. Figures 3.14,3.15 give ψ and DY oroduction respectively. Since the chosen parametrization affects all of the partons equally, the result is independent of the quarkonium production mechanism.

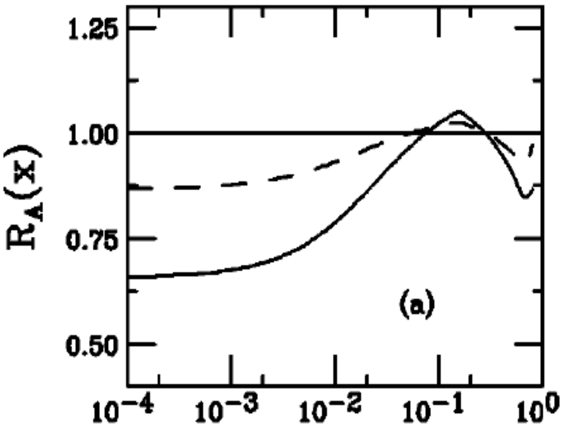

Figure 3.13: Shadowing function as a function of x. Predictions were made for W (solid curve) and Be (dashed curve) [44].

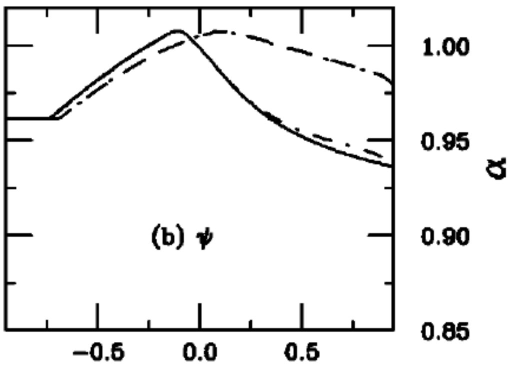

Figure 3.14: Resulting A dependence for ψ production in the CEM. Also NRQCD production at 800 GeV (dot-dashed), 120 GeV(dotted)

Comparing Fig. 3.14 and 3.3, we see that the effect of shadowing taken alone is not enough to explain the quarkonium nuclear suppression at large x_F observed experimentally.

3.2.3 Comover rescattering

Comover rescattering is one effect which could play a role in the A dependence of the J/ψ suppression. Schematically it can be pictured as in Fig. 3.16. To model the effect, we should calculate the comover cross section σ_{co}, which is the cross section of the interaction between the $c\bar{c}$ pair and its comovers. By comovers we mean the spectator partons of the projectile that comove with

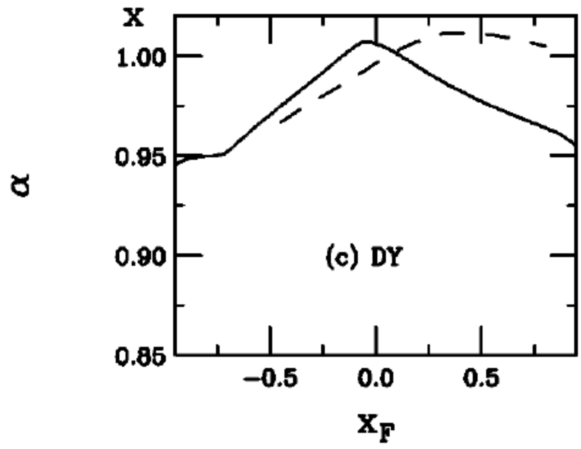

Figure 3.15: Nuclear dependence of DY production 800 GeV (solid line), and 120 GeV (dashed), arising from nuclear shadowing [44]

the $c\bar{c}$ pair, later they can either interact with the $c\bar{c}$ pair or fragment into hadrons. Depending on the model comovers can be either partonic or hadronic see Fig.3.16. Including the comover contribution, the x_F dependent J/ψ cross

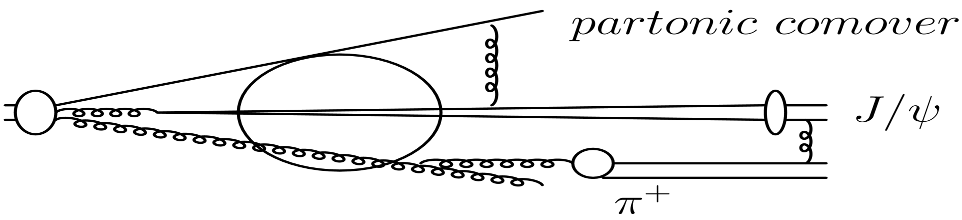

Figure 3.16: Comover rescattering in J/ψ production in $p - A$ collisions: partonic and hadronic comovers.

section can be expressed as [46]:

$$\frac{d\sigma_{pA}}{dx_F} = \frac{d\sigma^{pp}}{dx_F} \int d^2b \int_{-\infty}^{\infty} dz \rho_A(b,z) exp \left\{ - \int_{\tau_0}^{\tau_f} d\tau \sigma_{co}\, v\, n(\tau, b) \right\} \qquad (3.14)$$

Here, ρ_A is the nuclear density profile, τ_0 is the formation time of comovers, τ_f is an effective proper time over which the comovers interact with the $c\bar{c}$ pair, $n(\tau, b)$ is the density of comovers at the proper time τ, b is the impact parameter and v is the relative velocity between the $c\bar{c}$ pair and the comovers.

If comovers interact with the produced heavy quarks Q and $\bar{Q}$ before the quarkonium bound state is formed, one expects that for charmonium production the ($c\bar{c}$)-comover interaction cross section is the same for the J/ψ and ψ' bound states.

It is difficult to determine σ_{co} from the theory, thus in all the models it is a free parameter.

3.2.4 Relative momentum broadening of the $c\bar{c}$ pair

Here I briefly mention an effect proposed in [47]. When the $c\bar{c}$ pair is produced, it will interact with the nuclear medium before escaping it. If we let c and $\bar{c}$ be the parent-quarks of two jets and q^2 the square of the relative momentum between the two jets in their c.m. frame, then due to interactions with the medium q^2 increases. As a result, some of the $c\bar{c}$ pairs might gain enough relative q^2 to be pushed above the threshhold for open charm production, and consequently, the cross section for J/ψ production is reduced in comparison with nucleon-nucleon collisions. If the $c\bar{c}$ pair traverses the nucleus A, the increase of relative momentum is expected to be of the form:

$$q^2 \rightarrow q^2 + \varepsilon^2 L(A) \tag{3.15}$$

Here, $L(A)$ is the effective length of the nuclear medium for the $c\bar{c}$ pair to pass through. ε^2 represents the square of the relative momentum received by the $c\bar{c}$ pair per unit length of the nuclear medium. The value of ε^2 can be estimated from the experiment.

3.2.5 Parton energy loss

Parton energy loss through a hot QGP has been proposed to explain the phenomenon of jet-quenching observed in A-A collisions. Similarly, parton energy loss through cold nuclear matter has been proposed as an explanation for J/ψ suppression in $p-A$ collisions [48]. Here I briefly describe the effect heuristically, since Chapter 4 will be devoted to the energy loss calculation in various situations, and Chapter 5 to the related phenomenology of J/ψ suppression.

Schematically the production cross section of J/ψ in $p-A$ can be parametrized as:

$$\frac{d\sigma_{pp}}{dx_F} = (1 - x_F)^n \tag{3.16}$$

Here n varies depending on the energy of the collision.
We define the nuclear modification factor as:

$$R_{pA} = \frac{1}{A}\frac{d\sigma_{pA}/dx_F}{d\sigma_{pp}/dx_F} \tag{3.17}$$

If the quark pair loses energy due to the interaction with the nuclear medium, one can express the energy loss as a shift in x_F, denoted δx_F. Roughly speaking, producing a J/ψ with x_F in $p-A$ collisions requires producing it with $x_F + \delta x_F$ in an elementary $p-N$ collision. Hence the modification factor is of the form:

$$R_{pA} \simeq \frac{(1-(x_F+\delta x_F))^n}{(1-x_F)^n} \simeq \left(1 - \frac{\delta x_F}{1-x_F}\right)^n < 1 \tag{3.18}$$

3.3 The Gavin-Milana proposal: J/ψ suppression from parton energy loss

One of the first attempts to explain J/ψ nuclear suppression from parton energy loss ΔE in $p-A$ was done by Gavin and Milana. Usually their work is mentioned in the literature as the GM model [48]. Soon after their work has been criticised by Brodsky and Hoyer [49]. I briefly discuss these two studies.

The Gavin-Milana model

In their model GM try to understand the suppression of Drell-Yan (DY) and J/ψ production observed in $E772$ experiment. They assume that initial state multiple scatterings induce initial state energy loss resulting in the depletion of the projectile energy fraction x_1. Both quarks and gluons lose energy before the hard scattering and the loss is assumed to be the same in DY and J/ψ. The dependence is chosen to scale with $x_F \simeq x_1$ (not x_2), namely $\Delta x_1 \propto x_1$. The projectile parton momentum fraction participating in the hard process hence will be $x_1' = x_1 + \Delta x_1$. Here x_1 is the momentum fraction in the absence of rescatterings and Δx_1 is the shift due to energy loss.

In the GM model, Δx_1 is chosen as:

$$\Delta x_1 = k\, x_1\, C_i\, A^{1/3} \left(\frac{Q}{Q_0}\right)^n \tag{3.19}$$

Here i stands either for a quark or a gluon. As one can see from the formula above, the energy loss is chosen to scale with the projectile energy, but without a real justification. As already mentioned, the same formula is used for DY and J/ψ.

The stronger J/ψ suppression observed (compared to DY) in the experiment is explained by various effects:

- Since J/ψ is produced mainly via gluon fusion (at not too high x_F), the energy loss is expected to be larger, due to the color factor which enters the expression for energy loss ($C_g = 3$ for gluons, and $C_q = 4/3$ for quarks).

- At large x_F gluon parton distribution functions are steeper than the ones for quarks. The parametrizations for quarks and gluons are the following : $xq(x) \sim (1-x)^2$, $xg(x) \sim (1-x)^5$.

- Finally, in the GM model it is assumed that the produced $c\bar{c}$ pair travels like a color octet through the nucleus, and consequently loses energy like a gluon, assuming that multiple scatterings do not resolve the $c\bar{c}$ pair. This assumption is really crucial leading to a contribution from final state energy loss in the case of J/ψ.

Below one can see the comparison to data done by Gavin and Milana for DY and J/ψ (Fig.3.17). The same type of prediction was also made for Υ . The

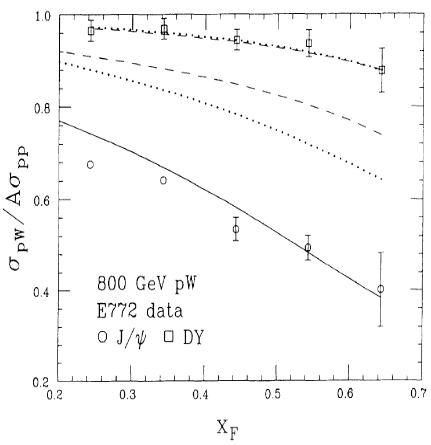

Figure 3.17: J/ψ and DY nuclear suppression in the GM model, in proton-tungsten collisions. The dotted and dashed curves are the expected depletion in J/ψ production arising solely from the initial-state scattering. The squares is the depletion for DY data. The solid curve is the prediction for J/ψ including final-state energy loss (J/ψ data is represented by circles).

GM model allows a satisfactory description of J/ψ nuclear suppression, as observed by the E772 experiment. The crucial feature of the model, $\Delta E \propto E$ (equivalently $\Delta x_1 \propto x_1$) is responsible for the increase of the suppression when x_F increases.

The drawback of the GM model is that $\Delta x \propto x$ is an ad hoc assumption. In Chapter 4, we will see that initial state (as well as final state) energy loss behaves as $\Delta E \propto L^2$ and not $\Delta E \propto E$

The Brodsky-Hoyer bound

After the study of Gavin and Milana, Brodsky and Hoyer [49] argued that the formula for Δx use by GM is against basic quantum mechanical principles, more precisely in contradiction with the uncertainty principle $\Delta L \Delta p_z > 1$. According to BH, some radiation can be released over the length L provided there is large enough longitudinal momentum transfer from the target in the inelastic process: $p_z > \Delta p_z > 1/\Delta L$. This relation sets a bound on the formation time of the radiated gluon. With $p_z \simeq k_\perp^2/(2\omega)$, one finds

$$\Delta L \frac{k_\perp^2}{2\omega} > 1 \Leftrightarrow t_f < \Delta L \tag{3.20}$$

Here, we used $t_f = \frac{\omega}{k_\perp^2}$. This led Brodsky and Hoyer to argue that the energy loss must be bounded, $\Delta E \sim \omega \lesssim \Delta L < k_\perp^2 >$, in contradiction with the GM assumption $\Delta E \propto E$.

In fact, we will see in Chapter 4, that the BH bound applies to the case of a charge suddenly stopped or suddenly accelerated, i.e., it applies to purely initial or purely final energy loss. However, it does not apply to the case of anymptotic charge crossing the medium, as is the case in J/ψ production at large x_F (see Chapter 4).

CHAPTER 4

Parton energy loss in $p - A$ collisions

Contents

4.1 Collisional vs radiative energy loss

There have been many studies dedicated to the calculation of parton energy loss. The average energy loss ΔE can depend on various quantities like the energy E of the radiating particle, its mass M, the temperature T of the medium , the coupling constant of the theory and the distance L the particle travels in the medium. The energy loss has two main contributions: collisional and radiative (see Figs. 4.1). Let us consider an energetic parton produced in a hard process (denoted by the blob in Fig. 4.1), for instance DIS. This energetic parton can undergo elastic scatterings in the nuclear medium, losing the energy $\sum q_i^0$ in such scatterings (Fig. 4.1 left). Such energy loss is currently called collisional energy loss. At next order in the QCD coupling, elastic scatterings can induce gluon radiation. The radiated gluon energy ω contributes to the radiative parton energy loss, see 4.1 (right).

Although radiative energy loss is formally of higher order in α_s than collisional energy loss, it is often dominant due to a different dependence in the parton energy E. It is known to dominate at large enough distances L and high enough energies [51].

Throughout my thesis, I focus on the case where radiative enery loss dominates.

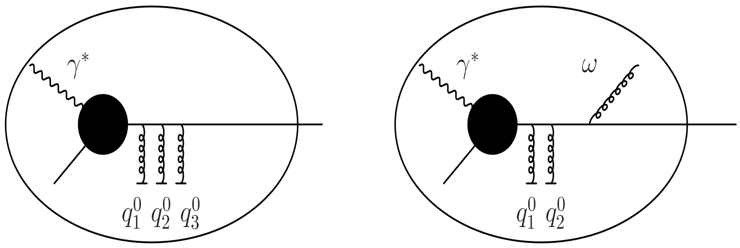

Figure 4.1: Collisional (left) vs radiative (right) energy losses.

4.2 Radiative energy loss: Important Notions

This section relies on a lecture of Y. Dokshitzer [50].

Formation Time

A physical electron can be viewed as a charge surrounded by its proper Coulomb field. This field consists of virtually radiated and later re-absorbed photons. Such virtual processes form a coherent state which is called a physical electron. This coherence is partially destroyed when the charge experiences some scattering, as a result a part of the virtual fluctuations are released as real photon radiation. At the same time, the deflected charge leaves the interaction point "half-dressed", lacking some part of its proper field. In the process of regeneration of a new Coulomb field, a new radiation appears off the deflected charge. Schematically the radiation and the absorption of a virtual photon is pictured in Fig. 4.2.

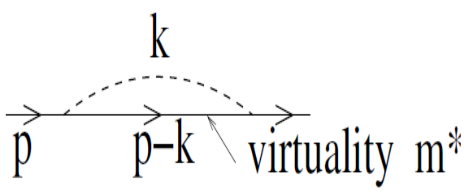

Figure 4.2: Virtual radiation and absorption of a photon.

The typical time between radiation and re-absorption of a photon $k = (\omega, \vec{k}_\perp, k^z)$ by the initial electron p may be estimated by the Lorentz-dilated lifetime of the intermediate virtual electron state (p-k). Using the on-shellness of the radiating parton, the fact that the photon is massless, and $\theta \simeq k_\perp/\omega \ll$

1, we obtain:

$$t_f = \frac{1}{m*}\frac{E}{m*} = \frac{E}{\mid (p-k)^2 - m^2 \mid} = \frac{E}{2pk} \simeq \frac{1}{\omega\theta^2} \simeq \frac{\omega}{k_\perp^2} \tag{4.1}$$

The quantity is usually called the typical photon formation time. An analagous formation time can of course be defined for gluon radiation off a quark (or gluon).

Coherent radiation

Diagrammatically the scattering of an electron off an external field can be shown as in Fig. 4.3:

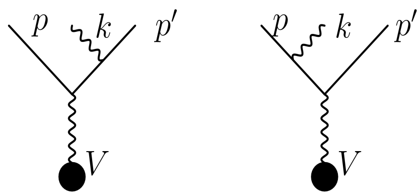

Figure 4.3: Photon bremsstrahlung diagrams for electron scattering off an external field.

Using QED Feynman rules the two contributions give:

$$M^\mu = e\,\bar{u}(p') \left[\gamma^\mu \frac{m + \not{p}' + \not{k}}{m^2 - (p'+k)^2} V + V \frac{m + \not{p} - \not{k}}{m^2 - (p-k)^2} \gamma^\mu \right] u(p) \tag{4.2}$$

where V is the vertex of interaction with the external field. The numerator of (4.2) can be simplified using Dirac equation for the on-shell electron:

$$\bar{u}(p')(m - \not{p}') = (m - \not{p})u(p) = 0 \tag{4.3}$$

and the relation:

$$\not{a}\not{b} = 2a \cdot b - \not{b}\not{a} \tag{4.4}$$

Hence, the bracket in (4.2) can be re-written as:

$$\frac{(2p'^\mu + \gamma^\mu \not{k})V}{m^2 - (p'+k)^2} + \frac{V(2p^\mu - \not{k}\gamma^\mu)}{m^2 - (p-k)^2} \tag{4.5}$$

Simplifyng the denominator by taking into account the on-shellness of the photon, we get

$$V\left[\frac{2p^\mu}{2(pk)} - \frac{2p'^\mu}{2(p'k)}\right] + \left[\frac{-V\not{k}\gamma^\mu}{2(pk)} - \frac{\gamma^\mu\not{k}V}{2(p'k)}\right] \tag{4.6}$$

For soft photon radiation, $k \to 0$, the first term dominates. We define j^μ as:

$$j^\mu(k) = \frac{p^\mu}{(pk)} - \frac{p'^\mu}{(p'k)} \tag{4.7}$$

Once we know the amplitude of the process, we can easily calculate the radiation cross section. For this, we need to square the matrix element, multiply by the phase-space factor and sum over polarization states λ,

$$d\sigma \propto \frac{d^3k}{(2\pi)^3 2\omega} \sum_{\lambda=1,2} \mid M_\mu \varepsilon^\mu_\lambda \mid^2 = \frac{d^3k}{(2\pi)^3 2\omega} M_\mu M^*_\nu \sum_{\lambda=1,2} \varepsilon^\mu_\lambda \varepsilon^{*\nu}_\lambda \tag{4.8}$$

Recall that one can choose a gauge so that, in a frame where $k^\mu = (\omega, 0, 0, \omega)$ we have

$$\varepsilon^1 = (0, 1, 0, 0); \varepsilon^2 = (0, 0, 1, 0)\,. \tag{4.9}$$

If we define $\hat{k} = \frac{k}{\omega^2} = (\omega^{-1}, 0, 0, \omega^{-1})$ one can check that we have a completeness relation (valid in any frame):

$$g_{\mu\nu} = \frac{1}{2}\left(k_\mu \hat{k}_\nu + \hat{k}_\mu k_\nu\right) - \sum_\lambda \varepsilon^\lambda_\mu \varepsilon^{*\lambda}_\nu \tag{4.10}$$

Thus, we have

$$M_\mu M^*_\nu \sum_{\lambda=1,2} \varepsilon^\mu_\lambda \varepsilon^{*\nu}_\lambda = \left[\frac{1}{2}\left(k_\mu \hat{k}_\nu + \hat{k}_\mu k_\nu\right) - g_{\mu\nu}\right] M^\mu M^{*\nu} = -g_{\mu\nu} M^\mu M^{*\nu} \tag{4.11}$$

since $k_\mu M^\mu = k_\mu M^{*\mu} = 0$. The calculation of the cross section is reduced to:

$$d\sigma \propto -M^\mu M_\mu \tag{4.12}$$

The cross section of soft photon radiation is given by the product of the non-radiative scattering cross section and the radiation factor dN:

$$d\sigma = \sigma_{scatt} dN \tag{4.13}$$

$$dN = \frac{\alpha}{4\pi^2} \omega d\omega d\Omega (-j^2_\mu) = \frac{\alpha}{\pi} \frac{d\omega}{\omega} \frac{d\Omega}{4\pi} (-\omega^2) \left[\frac{p^\mu}{(pk)} - \frac{p'^\mu}{(p'k)}\right]^2 \tag{4.14}$$

The expression (4.14) does not provide us with enough information. For example, one cannot say what part of the contribution comes from the initial or from the final charge. In fact, in Feynman gauge, the result is dominated by the interference term between two emitters:

$$dN \propto -\left[\frac{p^\mu}{(pk)} - \frac{p'^\mu}{(p'k)}\right]^2 \approx \frac{2(pp')}{(pk)(p'k)} \tag{4.15}$$

To answer this question, one must go back to (4.8) and do the calculation in the so-called radiative gauge. In this particular gauge, the scalar component of the potential is set to zero, $A_0 \equiv 0$. The photon is then described by 3-vectors orthogonal to each other and to its 3 momentum:

$$(\vec{\varepsilon}_\lambda \cdot \vec{\varepsilon}_{\lambda'}) = \delta_{\lambda\lambda'} \; ; \quad (\vec{\varepsilon}_\lambda \cdot \vec{k}) = 0 \tag{4.16}$$

Summing over polarizations we obtain:

$$dN \propto \sum_{\lambda=1,2} \mid \vec{j}(k)\vec{\varepsilon}_\lambda \mid^2 = \sum_{\alpha,\beta=1\ldots3} j^\alpha(k) \left[\delta_{\alpha\beta} - \frac{k_\alpha k_\beta}{\vec{k}^2}\right] j^{*\beta}(k)\,. \tag{4.17}$$

Two useful relations for further calculations:

$$v_{i\alpha}\left[\delta_{\alpha\beta} - \frac{k_\alpha k_\beta}{\vec{k}^2}\right] v_{i\beta} = v^2 - \frac{(v\cdot k)(k\cdot v)}{\vec{k}^2} = v_i^2 \sin^2\theta_i \tag{4.18}$$

$$v_{1\alpha}\left[\delta_{\alpha\beta} - \frac{k_\alpha k_\beta}{\vec{k}^2}\right] v_{2\beta} = v_1 v_2(\cos\theta_s - \cos\theta\cos\theta') \tag{4.19}$$

Here, $\theta, \theta', \theta_s$ are respectively the angles between the radiated photon and the initial charge, final charge and the angle between the initial and final charge. Using (4.17) and definition (4.7) we obtain:

$$dN = \frac{2\alpha}{\pi}\left[R_1 + R_2 + J\right]\frac{d\omega}{\omega}\frac{d\Omega}{4\pi} \tag{4.20}$$

Here

$$R_i = \frac{1}{2}\frac{v_i^2 \sin^2\theta_i}{(1 - v_i\cos\theta_i)^2} \; ; \quad i = 1, 2, \tag{4.21}$$

$$J \equiv \frac{1}{2}\frac{v_1 v_2(\cos\theta\cos\theta' - \cos\theta_s)}{(1 - v_1\cos\theta)(1 - v_2\cos\theta')} \tag{4.22}$$

Let us assume that we have a single charge accelerated (as in the decay of a muon at rest $\mu^- \to e^- + \nu_\mu + \bar{\nu}_e$). In this case the radiation spectrum is

$$\omega\frac{dN}{d\omega} = \frac{\alpha}{\pi}\frac{d\Omega}{4\pi}\frac{v_1^2\sin^2\theta}{(1 - v_1\cos\theta)^2} \tag{4.23}$$

Here θ is the angle between the electron and radiated photon. The full integration will give us :

$$R(v) \equiv \int \frac{d\Omega}{4\pi} R_1 = \frac{1}{2}\int \frac{d\Omega}{4\pi}\frac{v^2\sin^2\theta}{(1 - v\cos\theta)^2} = \frac{1}{2}\int\frac{d\Omega}{4\pi}\left(\frac{2}{1 - v\cos\theta} - 1 - \frac{1 - v^2}{(1 - v\cos\theta)^2}\right) \tag{4.24}$$

The angular integral over $d\Omega = \sin\theta d\theta d\phi$ reduces to polar angle integration:

$$\int \frac{d\Omega}{4\pi} = \frac{1}{2}\int_{-1}^{+1} d\cos\theta \tag{4.25}$$

Integrating and then summing all three terms of (4.24), we get [52]:

$$R(v) = \frac{1}{2v}\ln\frac{1+v}{1-v} - 1 \tag{4.26}$$

In case of two moving charges, all three terms of (4.20) are at work. The full sum is usually referred to as coherent radiation:

$$R_{coh}(\beta) \equiv R(v) + R(v') + J(v, v, \vec{v}\cdot\vec{v}') \tag{4.27}$$

In terms of velocities the expression for β is :

$$\beta = \sqrt{1 - \frac{(1-v^2)(1-v'^2)}{(1-\vec{v}\vec{v}')^2}} \tag{4.28}$$

One can calculate $R(\beta)$ in the rest frame of the initial charge, since it is Lorentz invariant,

$$\int \frac{d\Omega}{4\pi} R_{coh} = \int \frac{d\Omega}{4\pi} R(v') = I(\beta) \tag{4.29}$$

The velocity β of the final electron in the rest frame of the initial one can be expressed in terms of invariants. $(p\cdot p')$ is an invariant under Lorentz transformation

$$(p\cdot p') = EE' - \vec{p}\vec{p}' \tag{4.30}$$

In the rest frame of the first charge, $\vec{p} = 0$, we have

$$(p\cdot p') = E'm = \frac{m^2}{\sqrt{1-\beta^2}} \Longrightarrow \beta^2 = 1 - \left[\frac{m^2}{(pp')}\right]^2. \tag{4.31}$$

Hence, the energy spectrum reads

$$\omega\frac{dI}{d\omega} = \frac{2\alpha}{\pi}R(\beta) \tag{4.32}$$

This formula has the following interpretation. In the rest frame of the initial electron, the spectrum is given by the square of the emission amplitude off the final electron.

4.3 Large vs. small angle scattering

Let us consider various kinematical situations [52]. In the ultrarelativistic limit, i.e., where $v, v' \to 1$,

$$R(v) \simeq \frac{1}{2} \ln\left(\frac{1}{1-v}\right) \to \infty \tag{4.33}$$

This shows that the squares of initial and final emission amplitudes suffer from a logarithmic collinear singularity. As we learned in the first chapter this kind of singularities in QCD are resumed in the initial (final) distribution (fragmentation) functions.

We can apply the same limit to the interference term, and see that with fixed angle between $\vec{v}$ and $\vec{v'}$, and $\beta \to 1$, we get

$$\begin{aligned} I(v, v', \vec{v}\cdot\vec{v'}) &= \frac{1}{2\beta}\ln\frac{1+\beta}{1-\beta} - 1 - \frac{1}{2v}\ln\frac{1+v}{1-v} + 1 - \frac{1}{2v'}\ln\frac{1+v'}{1-v'} + 1 \\ &= 1 + \frac{1}{2\beta}\ln\frac{(1+\beta)^2}{1-\beta^2} - \frac{1}{2v}\ln\frac{(1+v)^2}{1-v^2} - \frac{1}{2v'}\ln\frac{(1-v')^2}{1-v'^2} \\ &\overset{v,v'\to 1}{\simeq} 1 + \ln\left(\frac{1-\vec{v}\cdot\vec{v'}}{2}\right) \end{aligned} \tag{4.34}$$

This shows no logarithmic enhancement when $\vec{v}\cdot\vec{v'} \ll 1$. Thus, in large angle scattering, the associated radiation is dominated by squares of the amplitudes of the initial and final emission vertices. Hence, the spectra is identified with the radiation of well-defined "partons". The dominance of collinear logarithms implies the dominance of large formation times. This can be easily seen from (4.24). The angular integration of the independent radiation diverges at small θ and the electron mass plays the role of a regulator. The logarithm in (4.33) arises from the angular domain $\theta_m^2 \ll \theta^2 \ll 1$, where $\theta_m^2 = m^2/E^2 = 1 - v^2$. The photon formation time $t_f \sim 1/(\omega\theta^2)$ is thus very large in the ultrarelativistic limit [52].

Let us now discuss the limit of small angle scattering. Recall that θ is the angle between the photon and the incoming charge itself, θ' is the angle between tbe photon and the final charge, and θ_s the scattering angle. We define: $\vec{\theta} = \vec{k_\perp}/\omega$, $\vec{\theta'} = \vec{\theta} - \vec{\theta_s}$, and $\vec{\theta_s} = \vec{q_\perp}/E$. In this case, the radiation spectrum, derived in the first section (4.20) can be re-written as

$$\omega\frac{dI}{d\omega} = \frac{\alpha}{\pi^2}\int\left(\frac{\vec{\theta'}}{\vec{\theta'}^2} - \frac{\vec{\theta}}{\theta^2}\right)^2 d^2\vec{\theta} \tag{4.35}$$

Independent radiation off the initial charge e^- will be:

$$\omega \frac{dI}{d\omega}\Big|_{initial} = \frac{\alpha}{\pi^2}\int \frac{d^2\vec{\theta}}{\theta^2} = \frac{\alpha}{\pi}\int_{\theta_m^2}^{1}\frac{d\theta^2}{\theta^2} \tag{4.36}$$

A broad radiation cone within the angles $\theta_m \ll \theta \ll 1$ develops around the initial charge, see Fig. 4.4.

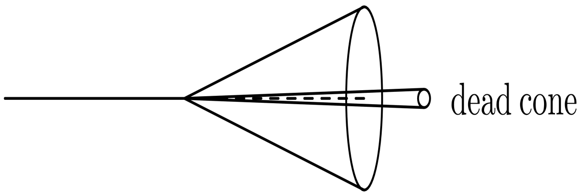

Figure 4.4: Large radiation cone around the initial charge, and small dead cone of opening θ_m.

Both independent terms give:

$$\omega \frac{dI}{d\omega} = \frac{2\alpha}{\pi}\int_{\theta_m^2}^{1}\frac{d\theta^2}{\theta^2} \tag{4.37}$$

For the emission angles smaller than $\theta_m = m/E$, one observes a "dead cone".

In the small angle limit the interference term, will be :

$$interference = \frac{\alpha}{\pi^2}\int d^2\vec{\theta}\frac{(-2\vec{\theta}\vec{\theta}')}{\theta^2\theta'^2} = \frac{-2\alpha}{\pi^2}\int \frac{d\theta^2}{\theta^2}\Theta(\theta^2-\theta_s^2) = \frac{-2\alpha}{\pi}\int_{\theta_s^2}^{1}\frac{d\theta^2}{\theta^2} \tag{4.38}$$

At large angles, when $\theta > \theta_s$, the interference term cancels the independent radiation. We obtain the expression for the total radiation,

$$\omega \frac{dI}{d\omega} = \frac{2\alpha}{\pi}\int_{\theta_m^2}^{\theta_s^2}\frac{d\theta^2}{\theta^2}\,. \tag{4.39}$$

If $\theta_m \to 0$, in this case we have 2 cones of opening θ_s around each of the charges (Fig.4.5). From (4.39) one sees that radiation is restricted to the angles $\theta \leq \theta_s = q_\perp/E$. This can be easily explained from formation time arguments [50]. If the charge scattering angle is θ_s, during the time t_f, the virtual photon γ can be reabsorbed if it does not see the electron's move,

$$\lambda_\perp > \Delta r_\perp(t_f) \Rightarrow \frac{1}{k_\perp} \simeq \frac{1}{\omega\theta} > \theta_s t_f \sim \frac{\theta_s}{\omega\theta^2} \tag{4.40}$$

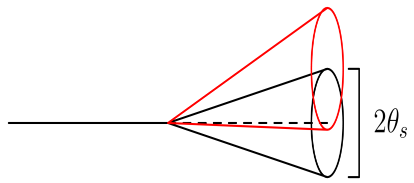

Figure 4.5: Coherent radiation when $\theta_m \to 0$.

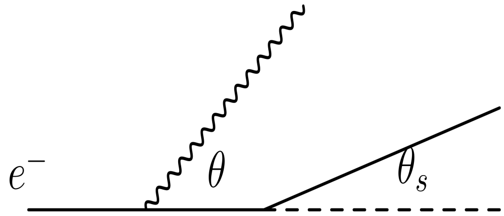

Figure 4.6: Radiation with $\theta > \theta_S$ during the scattering of the electron.

implying $\theta > \theta_s$, see Fig. 4.6.

Thus, by comparing the spatial displacement of the charge to the characteristic size of the photon field, one can see that the radiaton at $\theta > \theta_s$ is suppressed. Only photons with $\theta < \theta_s$ see the electron's move, corresponding to real radiation.

Medium induced photon radiation in large angle scattering

The process of photon radiation can be extended to the case of a finite size target. Suppose that we have a "QGP" of finite size L produced in A-A collisions shortly after the process of Fig. 4.1. We want to discuss the medium-induced radiation spectrum, i.e., the additional radiation in a medium when compared to the radiation without medium. Such medium-induced radiation can arise due to the presence of rescatterings in the medium, see Fig.4.7.

Let us assume that the medium-induced radiation spectrum is dominated by large formation times $t_f \gg L$, i.e., photon radiation does not probe the medium. Then the radiation spectrum depends only on the initial and final electron states (defined by the directions and velocities).

One should note that the final electron undergoes soft rescatterings inside the medium. This can in principle modify the radiation spectrum. But in case of large formation times, the in-medium re-scatterings only affect the direction of the final electron, hence the radiation spectrum in the presence of the medium is given by:

$$\omega \frac{dI}{d\omega} = \frac{2\alpha}{\pi} \left[R(v) + R(v') + I(v, v', \vec{v} \cdot \vec{v}' + \delta\vec{v} \cdot \vec{v}') \right] \tag{4.41}$$

$\delta\vec{v} \cdot \vec{v}'$ stands for the in-medium modification of the direction of the final electron. We have shown above that for $\vec{v} \cdot \vec{v}'$ and $\delta\vec{v} \cdot \vec{v}' \ll 1$ the interference term has no logarithmic enhancement, giving

$$\omega \frac{dI}{d\omega} \simeq \frac{2\alpha}{\pi} \left[R(v) + R(v') \right] \tag{4.42}$$

To estimate the additional radiation, which occurs due to the presence of the medium, one must subtract the spectrum obtained for the vacuum ($p-p$ case), from the one calculated in the presence of the medium. As one can see, the dominant terms cancel out, thus ruling out $t_f \gg L$ in the induced spectrum. One can conclude that the medium-induced radiation associated to large angle scattering must originate from photons with limited formation time $t_f \lesssim L$. We now sketch the derivation of the radiation spectrum, along the lines of [51] and [52].

Now let us consider photon radiation with $t_f \lesssim L$. In this case, radiation can probe the medium size L. For simplicity, one can start with a small medium of size $L \ll \lambda$, with λ the mean free path of the electron in the medium. This way, the scattered electron undergoes at most one elastic scattering. Radiation induced by such a scattering can be calculated from the diagrams of Fig. 4.7.

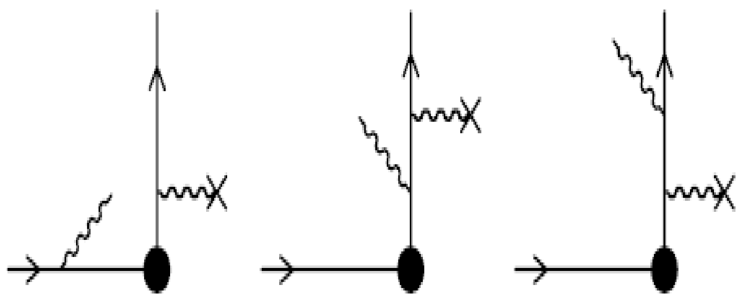

Figure 4.7: Diagrams contributing to medium-induced photon radiation in large angle scattering.

In case of large formation times, the second diagram (diagram where photon is emitted from the internal electron line) is neglected. However, it becomes important in case of small formation times. Squaring the sum of the diagrams of Fig.4.7 and subtracting the vacuum contribution, we find that the square of the emission amplitude off the incoming charge cancels out, and that the interference term of the emission amplitude before and after the hard process is negligible. Thus, while deriving the medium induced radiation spectrum, we can discard the radiation off the initial electron, and concentrate on the radiation occuring after the hard process, see Figs.4.8 and Fig.4.9, To

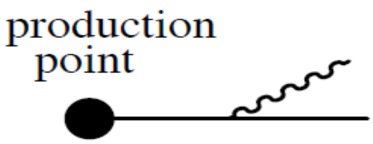

Figure 4.8: Photon radiation in the vacuum off the charge produced at $t = 0$.

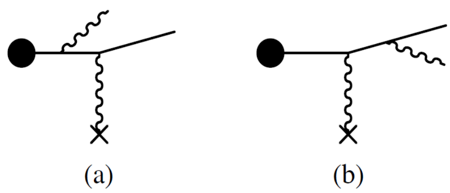

Figure 4.9: Photon radiation in the medium.

calculate explicitly the parametric dependence of the medium-induced spectrum, I will mention the result of Ref. [51] for $L \ll \lambda$ (here λ is the distance between two scattering centers). In vacuum, the radiation spectrum is obtained by squaring the amplitude of Fig.4.8. Neglecting the electron mass, and using (4.35), we get:

$$\omega \frac{dI}{d\omega}\bigg|_{vacuum} = \frac{\alpha}{\pi^2} \int d^2\vec{\theta}' \vec{J}^2_{vac} \tag{4.43}$$

where

$$\vec{J}_{vac} \equiv \frac{\vec{\theta}'}{\theta'^2} \tag{4.44}$$

The vector $\vec{\theta}'$ denotes the "angle" between the radiated photon and the final electron. The amplitude of Fig. 4.9 is given as [51]

$$\vec{J}_{med} = \frac{\vec{\theta}'}{\theta'^2} - \frac{\vec{\theta}}{\theta^2}\left[1 - e^{-i\omega L_0 \theta^2/2}\right] \tag{4.45}$$

L_0 is the distance travelled by the electron between its production point and the scattering. When the electron is produced in the medium we have $L_0 \sim L$. $\vec{\theta}'$ can be written as $\vec{\theta}' = \vec{\theta} - \vec{\theta}_s$, where $\vec{\theta}_s = \vec{q}_\perp/E$ is the electron scattering "angle" and $\vec{q_\perp}$ is the momentum exchange in the elastic scattering. Once we subtract the vacuum spectrum from the one calculated in the medium, and multiply by the single scattering probability $\sim L/\lambda$ we get the medium-induced spectrum:

$$\omega \frac{dI}{d\omega}\bigg|_{ind} \sim \frac{L}{\lambda}\frac{\alpha}{\pi^2}\int d^2\vec{\theta}(\vec{J}^2_{med} - \vec{J}^2_{vac}) \tag{4.46}$$

Using the explicit expressions for $\vec{J}_{vac}$ and $\vec{J}_{med}$, and the fact that

$$\int d^2\vec{\theta}\left[\left|\frac{\vec{\theta}'}{\theta'^2}\right| - \left|\frac{\vec{\theta}}{\theta^2}\right|^2\right] = 0 \tag{4.47}$$

the induced spectrum reads:

$$\omega \frac{dI}{d\omega}\bigg|_{ind} \sim \frac{L}{\lambda}\cdot\frac{2\alpha}{\pi^2}\int d^2\vec{\theta}\frac{\vec{\theta}}{\theta^2}\left(\frac{\vec{\theta}}{\theta^2} - \frac{\vec{\theta}'}{\theta'^2}\right)\left[1 - \cos\frac{\omega L_0 \theta^2}{2}\right] \tag{4.48}$$

(4.47) means that the radiation occurring after the electron scattering is, after integration over angles, identical to the radiation that occurs in vacuum: If we change the integration variable in the first term of (4.47), $\vec{\theta} \to \vec{\theta} + \vec{\theta}_s$, we remove all dependence on the scattering, and thus on the medium. The cancellation of (4.47) can also be viewed as the cancellation of large formation times $t_f \gg L$ in the induced spectrum, leaving only the contribution (4.48) which turns out to be dominated by $t_f \lesssim L$.

Let us simplify (4.48) by averaging over azimuthal direction of $\vec{\theta}_s$ using

$$\int \frac{d\phi}{2\pi}\left(\frac{\vec{\theta}}{\theta^2} - \frac{\vec{\theta} - \vec{\theta}_s}{(\vec{\theta} - \vec{\theta}_s)^2}\right) = \frac{\vec{\theta}}{\theta^2}\Theta(\theta_s^2 - \theta^2). \tag{4.49}$$

We then average over θ_s^2, using the Coulomb scattering probability distribution:

$$P(\theta_s^2) = \frac{\mu^2/E^2}{(\theta_s^2 + \mu^2/E^2)^2}. \tag{4.50}$$

μ is the typical value of the transverse momentum exchange $q_\perp$. Thus (4.48) can be written as

$$\frac{\mu^2}{E^2}\int d\theta^2 \int_{\theta^2}^{\infty} d\theta_s^2 \left|\frac{\vec{\theta}}{\theta^2}\right|^2 \Theta(\theta_s^2 - \theta^2)\left[1 - \cos\frac{\omega L_0 \theta^2}{2}\right]\frac{1}{(\theta_s^2 + \frac{\mu^2}{E^2})^2} \tag{4.51}$$

(4.48) turns into:

$$\omega \frac{dI}{d\omega}\bigg|_{ind} \sim \frac{L}{\lambda}\frac{2\alpha}{\pi}\frac{\mu^2}{E^2}\int_0^\infty d\theta^2 \frac{(1-\cos(\omega L_0\theta^2/2))}{\theta^2(\theta^2+\mu^2/E^2)} \tag{4.52}$$

At high energy we have $\mu^2/E^2 \ll 1/(\omega L_0)$, leaving us with

$$\omega \frac{dI}{d\omega}\bigg|_{ind} \sim \frac{L}{\lambda}\frac{2\alpha}{\pi}\frac{\mu^2}{E^2}\int_0^\infty d\theta^2 \frac{(1-\cos(\omega L_0\theta^2/2))}{\theta^4} \tag{4.53}$$

The angular integral is saturated by $\theta^2 \sim 1/(\omega L_0)$, i.e., by formation times

$$t_f \sim \frac{1}{\omega\theta^2} \sim L_0 \sim L \tag{4.54}$$

The medium induced spectrum reads

$$\omega \frac{dI}{d\omega}\bigg|_{ind} \sim \alpha \frac{\omega}{E^2}\frac{L^2\mu^2}{\lambda} \tag{4.55}$$

Integrating the spectrum up to $\omega \sim E$ yields the medium-induced energy loss

$$\Delta E = \int_0^E d\omega \left(\omega \frac{dI}{d\omega}\right) \sim \alpha \frac{\mu^2}{\lambda} L^2 \tag{4.56}$$

We see that the energy loss is energy independent. This is a direct consequence of the constraint $t_f \leq L$.

To summarize this section, the medium induced energy loss associated to large angle scattering of a charge scales as L^2. It arises from small formation times, since large formation times cancel out.

Medium-induced radiation in small angle scattering

In this section we will consider small angle scattering of an asymptotic charge, as in [52]. In the target rest frame, we can model the process as follows: the incoming energetic charge of momentum $p = (E, \vec{0}_\perp, p_z)$ scatters off a target with a limited momentum exchange q. The associated radiation amplitude is depicted in Fig.4.10. Our discussion applies to the case of a particle of mass m and energy $E \gg m$, which scatters to a particle of mass M, and energy $E' \gg M$. To obtain the radiation spectrum associated to the process, let us assume that the radiation arises from large formation times $t_f \gg L$. The radiation spectrum can be obtained using (4.20) and (4.26). Here $\vec{v}'$ is now the velocity of the outgoing particle. For small angle scattering $\vec{v}\vec{v}' \simeq 1$. If we denote the angle θ_s between $\vec{v}$ and $\vec{v}'$, $\theta_s \ll 1$, and using $\theta_m^2 \equiv m^2/E^2 =$

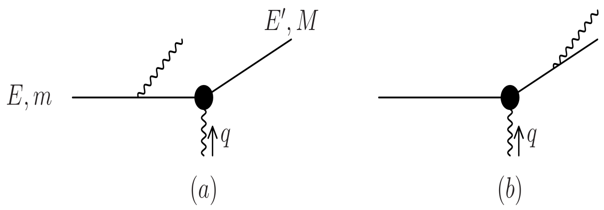

Figure 4.10: Radiation of a photon in small angle scattering. a) radiation off the initial charge, b) radiation off the final charge.

$1 - v^2 \ll 1$ and $\theta_M^2 \equiv M^2/E^2 \simeq 1 - v'^2 \ll 1$, the relative velocity defined in (4.28) can be re-written as:

$$\beta \simeq \sqrt{1 - \frac{4\theta_m^2\theta_M^2}{(\theta_M^2 + \theta_m^2 + \theta_s^2)^2}} \tag{4.57}$$

Here, we used the fact that

$$|\vec{v}'| = \sqrt{1 - \theta_M^2} \simeq 1 - \frac{\theta_M^2}{2} \tag{4.58}$$

$$|\vec{v}| = \sqrt{1 - \theta_m^2} \simeq 1 - \frac{\theta_m^2}{2} \tag{4.59}$$

$$\vec{v}\vec{v}' = |\vec{v}||\vec{v}'|\cos\theta_s \simeq 1 - \frac{\theta_s^2 + \theta_m^2 + \theta_M^2}{2} \tag{4.60}$$

Since $M \gg m$,we have $\beta \to 1$. Using (4.34), we find:

$$I(v, v', \vec{v}\cdot\vec{v}') \underset{\beta\to 1}{\simeq} \ln(1 - \vec{v}\vec{v}') \simeq \ln\left(\frac{\theta_M^2 + \theta_m^2 + \theta_s^2}{2}\right) \tag{4.61}$$

One can see that contrary to large angle scattering, in small angle scattering the interference term is not negligible. For "$p-p$ collisions" the energy spectrum reads,

$$\omega \frac{dI}{d\omega}\bigg|_{pp} \simeq \frac{\alpha}{\pi}\left[\ln\left(\frac{1}{\theta_m^2}\right) + \ln\left(\frac{1}{\theta_M^2}\right) - 2\ln\left(\frac{1}{\theta_M^2 + \theta_s^2|_{pp}}\right)\right] \tag{4.62}$$

The first 2 terms stand for the radiation off the inital and final charges respectively, the third term stand for the interference. One can see that the interference term largely compensates the other terms.

In $p-A$ collisions, the angle between the outgoing parton and incoming one tends to increase, due to transverse momentum broadening in the target nucleus. If we have a target of sufficiently large size $L \gg \lambda$ (with λ the mean free path of the fast charge in the target), then the transverse momentum broadening is given by the random walk estimate

$$\Delta q_\perp^2 \sim \frac{L}{\lambda}\mu^2 \equiv \hat{q}L \tag{4.63}$$

where $\hat{q} \equiv \frac{\mu^2}{\lambda}$ is the transport coefficient giving the rate of transverse momentum broadening per unit length. Thus $\theta_s^2|_{pA} = \theta_s^2|_{pp} + \Delta\theta_s^2$ where $\Delta\theta_s^2 = \Delta q_\perp^2/E^2$ is the angular broadening. The radiation spectrum in $p-A$ is equivalent to that associated to a single effective scattering of transverse exchange $q_\perp^2 = q_\perp^2|_{pp} + \Delta q_\perp^2$. Let us concentrate on the limit where $\Delta q_\perp^2 \ll q_\perp^2|_{pp}$. The

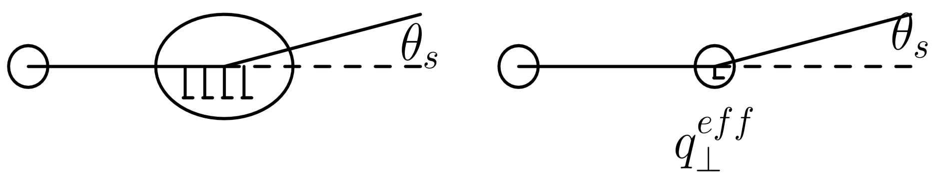

Figure 4.11: Broadening in $p-A$ collisions on the left can be replaced by a single effective scattering (right).

broadening in θ_s brings modification to the $p-p$ spectrum, giving

$$\omega\frac{dI}{d\omega}\bigg|_{pA} \simeq \frac{\alpha}{\pi}\left[\ln\left(\frac{1}{\theta_m^2}\right) + \ln\left(\frac{1}{\theta_M^2}\right) - 2\ln\left(\frac{1}{\theta_M^2 + \theta_s^2|_{pA}}\right)\right] \tag{4.64}$$

The medium-induced spectrum is obtained by subtracting (4.62) from (4.64):

$$\omega\frac{dI}{d\omega}|_{ind} = \frac{2\alpha}{\pi}\ln\frac{\theta_M^2 + \theta_s^2|_{pA}}{\theta_M^2 + \theta_s^2|_{pp}} = \frac{2\alpha}{\pi}\ln\left(1 + \frac{\Delta\theta_s^2}{\theta_M^2 + \theta_s^2|_{pp}}\right) \simeq \frac{2\alpha}{\pi}\frac{\Delta q_\perp^2}{M_\perp^2} \tag{4.65}$$

where $M_\perp = \sqrt{M^2 + q_\perp^2}$ is the transverse mass. At high energies all the angles mentioned in the discussion $(\theta, \theta_M, \theta_m, \theta_s)$ are small. It is interesting to see how (4.65) arises in a less heuristic derivation. The radiation amplitude reads (see Fig. 4.10),

$$\vec{J} = \frac{\vec{\theta}'_{pA}}{\theta'^2_{pA} + \theta_M^2} - \frac{\vec{\theta}}{\theta^2 + \theta_m^2} \tag{4.66}$$

The first term arises from the emission off the final line, the second term stands for the radiation off the initial one. Here, $\vec{\theta}'_{pA} = \vec{\theta} - \vec{\theta}_s|_{pA}$. As before, to compute the medium induced spectrum we subtract the vacuum contribution obtained from $\vec{\theta}^2|_{pA} \to \theta_{pp}^2$. Taking $m \to 0$ we get:

$$\omega \frac{dI}{d\omega}\bigg|_{ind} = \frac{\alpha}{\pi^2} \int d^2\vec{\theta} \left(\vec{J}^2_{med} - \vec{J}^2_{vac} \right) = -\frac{2\alpha}{\pi} \int \frac{d^2\vec{\theta}}{\theta^2 + \theta_M^2} \left[\frac{\vec{\theta} \cdot \vec{\theta}'_{pA}}{\theta'^2_{pA}} - (vac) \right] \tag{4.67}$$

From (4.49) one can deduce

$$\int \frac{d\phi}{2\pi} \frac{\vec{\theta} \cdot \vec{\theta}'}{\theta'^2} = \Theta(\theta^2 - \theta_s^2) \tag{4.68}$$

thus for the medium induced spectrum we get:

$$\omega \frac{dI}{d\omega}\bigg|_{ind} \simeq \frac{2\alpha}{\pi} \int_{\theta_s^2|_{pp}}^{\theta_s^2|_{pA}} \frac{d\theta^2}{\theta^2 + \theta_M^2} \tag{4.69}$$

from which one can recover (4.65). We obtain the confirmation of our initial assumption, that the radiation is associated to large formation times:

$$t_f \sim \frac{1}{\omega(\theta^2 + \theta_M^2)} \simeq \frac{1}{\omega(\theta_s^2|_{pp} + \theta_M^2)} = \frac{E^2}{\omega M_\perp^2} \gg L\,. \tag{4.70}$$

4.4 QCD: radiation spectrum of an asymptotic color charge

Soft scattering

Let us first consider an energetic parton of energy E going through some nuclear target and exchanging a transverse momentum $\ell_\perp$ [67]. As we saw in the previous section, in QED the scattering can induce a radiation provided that $\theta_s \simeq q_\perp/E \neq 0$. In QCD, this is possible even when $\theta_s \to 0$, due to the color rotation of the parton in the scattering. We denote by ω the energy of the radiated gluon, and by $k_\perp$ the transverse momentum. Let us focus on soft ($\omega \ll E$) and small angle ($k_\perp \ll E$) radiation. For an on shell light quark the amplitude of the process reads [54]:

$$\frac{M_{rad}}{M_{el}} \sim \left[T^a T^b \frac{\vec{\theta}}{\theta^2} + \left[T^a, T^b\right] \frac{\vec{\theta}''}{\theta''^2} - T^b T^a \frac{\vec{\theta}'}{\theta'^2} \right] \vec{\varepsilon}_\perp \tag{4.71}$$

where

$$\vec{\theta} = \frac{k_\perp}{\omega}; \quad \vec{\theta}' = \vec{\theta} - \vec{\theta}_s; \quad \vec{\theta}'' = \vec{\theta} - \vec{\theta}_g; \quad \vec{\theta}_s \equiv \frac{\vec{l}_\perp}{E}; \quad \vec{\theta}_g \equiv \frac{\vec{l}_\perp}{\omega} \tag{4.72}$$

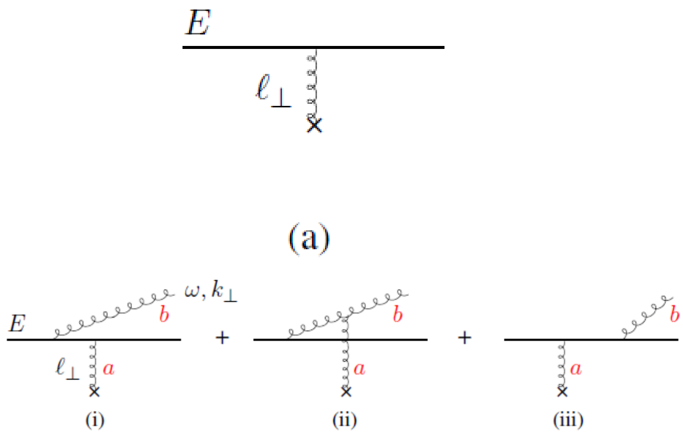

Figure 4.12: Elastic scattering amplitude M_{el}, and induced gluon radiation M_{rad}

and $\vec{\varepsilon}_\perp$ the polarization vector of the radiated gluon. The first two terms of (4.71) correspond to initial state radiation, whereas the last term stands for final state radiation. In the abelian case, the second diagram is absent (see previous section), as well as the color factor, and the radiation spectrum can be re-expressed in terms of $l_\perp$ instead of $q_\perp$ as

$$\omega\frac{dI}{d\omega}|_{QED} = \frac{2\alpha}{\pi}\int_0^{\theta_s^2}\frac{d\theta^2}{\theta^2+\theta_m^2} = \frac{2\alpha}{\pi}\ln\left(1+\frac{\theta_s^2}{\theta_m^2}\right) = \frac{2\alpha}{\pi}\ln\left(1+\frac{l_\perp^2}{m^2}\right) \quad (4.73)$$

where $\theta_m = m/E$. Radiation vanishes when $\theta_s = 0$.

To single out the pure QCD contribution we take $\theta_s \to 0$ in (4.71). If we look at the resulting expression, we notice that it is the same as in QED, with the exception that instead of $\vec{\theta}'$ we get $\vec{\theta}''$

$$[T^a, T^b]\left[\frac{\vec{\theta}}{\theta^2} - \frac{\vec{\theta}-\vec{\theta}_g}{(\vec{\theta}-\vec{\theta}_g)^2}\right] \quad (4.74)$$

Squaring (4.74) we obtain the famous Gunion-Bertsch spectrum (derived in Appendix 1):

$$\omega\frac{dI}{d\omega d^2\vec{k}_\perp} \sim \alpha_s\frac{l_\perp^2}{k_\perp^2(\vec{k}_\perp-\vec{l}_\perp)^2}. \quad (4.75)$$

Color charge resolved in hard scattering

The case of a charge resolved in a hard process is modelled by introducing the hard momentum transfer $q_\perp \gg l_\perp$ (see Fig. 4.13). Here, $l_\perp$ plays the role of nuclear momentum broadening, defined as $l_\perp^2 \equiv \Delta q_\perp^2$. We have seen in the case of QED, that some radiation is released even in the absence of the medium, i.e., when $l_\perp = 0$ due to the presence of hard exchange. The quantity of interest is the medium-induced energy loss, obtained by subtracting the p-p radiation spectrum from the one obtained in p-A.

$$\omega \frac{dI}{d\omega}\bigg|_{ind} \equiv \omega \frac{dI}{d\omega}(q_\perp; l_\perp) - \omega \frac{dI}{d\omega}(q_\perp, l_\perp = 0) \tag{4.76}$$

We focus on soft radiation, $\omega \ll E$, and $k_\perp \ll q_\perp$. We also assume large

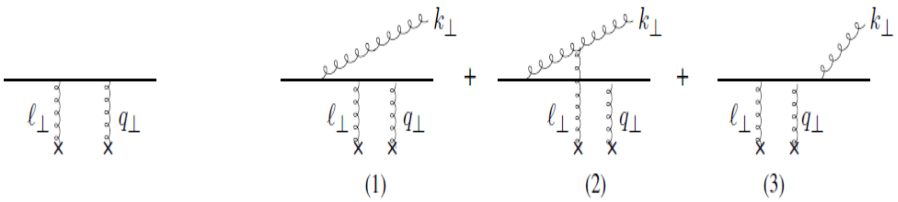

Figure 4.13: Radiation induced by soft scattering of the parton in a hard process (modelled by $q_\perp$).

formation times. This way, the dominant diagrams that contribute to the radiation spectrum are (1),(2),(3) of Fig. 4.13.

The radiation amplitude corresponding the Fig.4.13, as for the case of an asymptotic charge, is given by

$$\frac{M_{rad}}{M_{el}} \sim C_1 \frac{\vec{\theta}}{\theta^2} + C_2 \frac{\vec{\theta}''}{\theta''^2} - C_3 \frac{\vec{\theta}'}{\theta'^2} \tag{4.77}$$

here,

$$\vec{\theta}' = \vec{\theta} - \vec{\theta}_s; \quad \vec{\theta}'' = \vec{\theta} - \vec{\theta}_g; \quad \vec{\theta}_s \equiv \frac{\vec{l_\perp} + q_\perp}{E} \simeq \frac{\vec{q_\perp}}{E}; \quad \vec{\theta}_g \equiv \frac{\vec{l_\perp}}{\omega} \tag{4.78}$$

Since the radiation off the initial and final charges cancel in the medium induced spectrum, the main contribution comes from the interference term, i.e., graph (2) and (3) in the Fig.(4.13). The amplitude for graph (3) is:

$$\frac{M_{final}}{M_{el}} \sim -\frac{\vec{\theta}'}{\theta'^2} \tag{4.79}$$

the radiation off the initial charge:

$$\frac{M_{initial}}{M_{el}} \propto \frac{\vec{\theta}''}{\theta''^2} \tag{4.80}$$

Thus to calculate the medium induced spectrum , we must multiply (4.80) with (4.79), integrate over $d^2\vec{\theta}$ and subtract the vacuum contribution:

$$\omega \frac{dI}{d\omega}\bigg|_{ind} \sim -\alpha_s \int d^2\vec{\theta} \left[\frac{\vec{\theta}-\vec{\theta}_s}{(\theta-\theta_s)^2} \cdot \frac{\vec{\theta}-\vec{\theta}_g}{(\theta-\theta_g)^2} - vac \right] \tag{4.81}$$

Applying the change of variables $\vec{\theta} \to \vec{\theta} + \vec{\theta}_s$, we get:

$$\omega \frac{dI}{d\omega}\bigg|_{ind} \simeq -\alpha_s \int \frac{d^2\vec{\theta}}{\theta^2} \left(\frac{\vec{\theta}(\vec{\theta}+\vec{\theta}_s-\vec{\theta}_g)}{(\theta+\theta_s-\theta_g)^2} - vac \right) \tag{4.82}$$

The latter expression is similar to (4.67) up to the replacement $\vec{\theta}_s \to \vec{\theta}_s - \vec{\theta}_g$. Using (4.68), the angular integration gives:

$$\omega \frac{dI}{d\omega}\bigg|_{ind} \sim \alpha_s \int_{\vec{\theta}_s^2}^{(\vec{\theta}_s-\vec{\theta}_g)^2} \frac{d\theta^2}{\theta^2} \sim \alpha_s \int_{x^2 q_\perp^2}^{(x\vec{q}_\perp - \vec{l}_\perp)^2} \frac{dk_\perp^2}{k_\perp^2} \tag{4.83}$$

In the equation above, we used explicit expressions for θ_s ,θ_g, $x = \omega/E$, and used

$$(\vec{\theta}_s - \vec{\theta}_g)^2 = \left(\frac{\vec{q}_\perp}{E} - \frac{\vec{l}_\perp}{\omega} \right)^2 = \frac{1}{\omega^2}(x\vec{q}_\perp - \vec{l}_\perp)^2; \tag{4.84}$$

$$\vec{\theta}_s^2 \cdot \omega^2 = q_\perp^2 x^2 \tag{4.85}$$

Heuristically,

$$(x\vec{q}_\perp - \vec{l}_\perp)^2 \sim x^2 q_\perp^2 + l_\perp^2 \tag{4.86}$$

We get:

$$\omega \frac{dI}{d\omega}\bigg|_{ind} = \frac{N_c \alpha_s}{\pi} \ln\left(1 + \frac{l_\perp^2 E^2}{q_\perp^2 \omega^2}\right) \tag{4.87}$$

Integrating the spectrum, one obtains the energy loss of a radiating on-shell parton:

$$\Delta E = \int d\omega \left(\omega \frac{dI}{d\omega} \right)_{ind} \sim \alpha_s \frac{l_\perp}{q_\perp} \cdot E \tag{4.88}$$

Just as the spectrum for an asymptotic particle, the spectrum for a particle resolved in a hard process is $\propto E$. Having done the calculation in the massless limit, let us see what happens with a parton mass $M \neq 0$. This easy to do, by going back to (4.83) and modifying the denominator:

$$\omega \frac{dI}{d\omega}\bigg|_{ind} \sim \frac{N_c \alpha_s}{\pi} \int_{\theta_s^2}^{(\vec{\theta}_s-\vec{\theta}_g)^2} \frac{d\theta^2}{\theta^2+\theta_M^2} \sim \ln\left(1+\frac{\hat{\omega}^2}{\omega^2}\right); \quad \hat{\omega} \equiv \frac{\sqrt{l_\perp}}{M_\perp} E \ll E \tag{4.89}$$

where $M_\perp = (M^2 + q_\perp^2)^{\frac{1}{2}}$.

Unlike QED, we observe that the QCD spectrum involves a new scale, above which the spectrum is suppressed as $\sim 1/\omega^2$. Thus, the medium-induced radiated energy arises from gluon energies $\omega \sim \hat{\omega} \ll E$ and thus from gluon formation times $t_f \sim E^2/(\hat{\omega} M_\perp^2) \gg E/M_\perp^2 \gg L$.

Let us single out purely perturbative contribution to our spectrum assuming $k_\perp > \Lambda_{QCD}$. Using $k_\perp \simeq \omega\theta$, the spectrum (4.89) can be re-expressed as

$$\omega \frac{dI}{d\omega}\bigg|_{ind} \sim \frac{N_c \alpha_s}{\pi} \int_{\mathrm{Max}(\mathrm{x}^2\mathrm{q}_\perp^2, \Lambda_{\mathrm{QCD}}^2)}^{x^2 q_\perp^2 + l_\perp^2} \frac{dk_\perp^2}{k_\perp^2 + x^2 M^2} \tag{4.90}$$

Approximating $\mathrm{Max}(\mathrm{x}^2\mathrm{q}_\perp^2, \Lambda_{\mathrm{QCD}}^2) \sim \mathrm{x}^2\mathrm{q}_\perp^2 + \Lambda_{\mathrm{QCD}}^2$, the expression for the spectrum turns into

$$\omega \frac{dI}{d\omega}\bigg|_{ind} \sim \frac{N_c \alpha_s}{\pi} \left\{ \ln\left(1 + \frac{\hat{\omega}^2}{\omega^2}\right) - \ln\left(1 + \frac{\omega_0^2}{\omega^2}\right) \right\} \tag{4.91}$$

where $\omega_0 = \frac{\Lambda_{QCD}}{M_\perp} E < \hat{\omega}$. Expression (4.91) will be used throughout Chapter 5 in the application of the energy loss model to the quarkonium suppression.

4.5 The transport coefficient $\hat{q}$

Nuclear broadening is one of the main ingredients of our model. It controls the amount of medium-induced gluon radiation. By definition,

$$\Delta q_\perp^2(L) = \hat{q} L - \hat{q}_p L_p \tag{4.92}$$

The average path length is given by $L = \frac{3}{2} R_A$ where $R_A = r_0 A^{1/3}$. Thus we see that our model actually depends on $\hat{q}$-the transport coefficient. To quantify this parameter, we need to study it a little more in detail.

The transport coefficient has a non-trivial dependence on momentum fraction x [55],

$$\hat{q} = \frac{4\pi^2 \alpha_s(\hat{q}L) N_c}{N_c^2 - 1} \rho x \mathcal{G}(x, \hat{q}L) \simeq \frac{4\pi^2 \alpha_s N_c}{N_c^2 - 1} \rho x \mathcal{G}(x) \tag{4.93}$$

In the latter, since $\hat{q}L \lesssim 1$ GeV^2, the scale violation in α_s and $\mathcal{G}$ can be neglected. To approximate the typical value of x in $x\mathcal{G}(x)$ we follow the discussion of [55].

Let us consider a quark produced in DIS, and scattering off the target. The generic process is depicted on Fig.4.14. The typical value of x varies depending on the kinematics of the process [67]. The quark p scatters off the nucleon of momentum P, it is chosen to travel along the z direction. In the nucleus rest frame $P = (m_N, \vec{0})$, with m_N the nucleon mass. In light cone

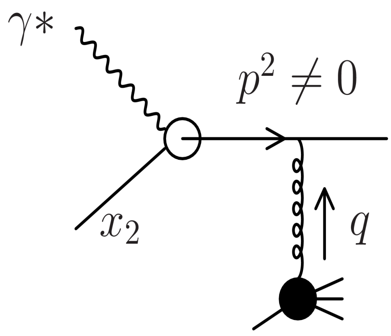

Figure 4.14: Basic quark-nucleon scattering amplitude [55].

coordinates the quark's momentum will be expressed as $p = (p^+, p^-, \vec{0_\perp})$. By definition $p^\pm = p^0 \pm p^z$. The final quark must be on-shell, which leads to,

$$(p+q)^2 = (p^+ + q^+)(p^- + q^-) - q_\perp^2 = 0 \Rightarrow p^+ + q^+ \simeq \frac{q_\perp^2}{p^-} \tag{4.94}$$

q^- can be neglected, since $p^- = p^0 - p^z \simeq 2E \gg q^-$. The following two kinematical conditions can be considered:

- Parton production inside the target: if the hard production time is much less than the size of the medium, $t_{hard} \ll L$, this is equivalent to $x_B \equiv Q^2/(2m_N E) \gg x_0 \equiv 1/(2m_N L)$. With this condition, the parton is produced inside the nucleus (see Fig. 4.15)

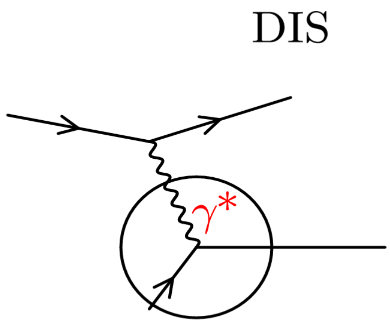

Figure 4.15: Parton production inside the nucleus. Produced quark is off-shell ($p^2 = 0$).

If the rescattering occurs at distance z from the production point, due to the uncertainty principle, the parton momentum before the rescattering is related to the z as $1/|p^+|$. Since $z \leq L$, we obtain $p^+ \gtrsim 1/L$. At large p^-, from (4.94), one can see that $q^+ \simeq |p^+|$. Then the momentum fraction of the rescattering gluon satisfies the following relation,

$$x \equiv \frac{q^+}{P^+} = \frac{q^+}{m_N} \simeq \frac{|p^+|}{m_N} \sim \frac{1}{2m_N L} = x_0. \tag{4.95}$$

- Parton production far before the target: if the production time is larger than the size of the medium, $t_{hard} \gg L \Leftrightarrow x_B \ll x_0$. In this case the quark virtuality is the same as the virtuality of a split virtual photon, i.e., $|p^2| = |p^+p^-| \sim Q^2$, and $|p^+| \sim Q^2/p^-$. It is clear that p^+ is no longer bounded by $1/L$. From (4.94) one gets,

$$x = \frac{q^+}{m_N} \simeq \frac{|p^+|}{m_N} \sim \frac{Q^2}{m_N p^-} = x_B \sim x_2 \tag{4.96}$$

Thus, x parameter is estimated as

$$x = x_0\Theta(x_2 > x_0) + x_2\Theta(x_2 < x_0) = \min(x_0, x_2); \quad x_0 \equiv \frac{1}{2m_N L}. \tag{4.97}$$

4.6 Application to quarkonium production

For our spectrum to be applied to quarkonium production, the partonic process should look like the scattering of a pointlike color charge, at least for a radiated gluon with formation time $t_f \gg L$. Thus the condition is :

$$Max(L, t_{hard}) \ll t_f \ll t_{octet} \quad \text{and} \quad r_\perp(t_f) \ll 1/k_\perp \tag{4.98}$$

here t_{hard} is a hard process time scale, t_{octet} the lifetime of the color octet $Q\bar{Q}$ pair, and t_ψ the quarkonium hadronization time.

We can prove that the typical formation time derived for the energy loss in the last section, satisfies above conditions. For simplicity, let's assume, that $L < t_{hard} \sim E/M_\perp^2$ and $M_\perp \simeq M$ and denote $l_\perp^2 \sim \Delta q_\perp^2$. As already mentioned at the end of previous section, ΔE arises from radiated energies $\omega \sim (l_\perp/M)E \ll E$ and transverse momenta $k_\perp^2 \sim l_\perp^2$. The typical t_f thus satisfies

$$t_{hard} \sim \frac{E}{M^2} \ll t_f \sim \frac{1}{\omega\theta^2} = \frac{\omega}{k_\perp^2} \sim \frac{E}{Ml_\perp} \ll t_\psi \sim \frac{E}{M}\tau_\psi \tag{4.99}$$

Here, nuclear broadening $l_\perp$ is soft compared to M, yet hard compared to the non-perturbative scale τ_ψ^{-1}. Now let us check the second condition. It reads

$$k_\perp r_\perp(t_f) \sim k_\perp v_\perp t_f \sim l_\perp \frac{\alpha_s M}{E} \cdot \frac{E}{Ml_\perp} \sim \alpha_s \ll 1 \tag{4.100}$$

Here we used the fact that $t_f \sim \frac{E}{Ml_\perp}$, and $v_\perp$ is estimated as $v_\perp \sim p_{B\perp}/E$ with p_B the Bohr momentum of the quarkonium state [56].

In the next chapter we will discuss in detail the model, where the energy spectrum derived for QCD can be applied to the calculation of quarkonium suppression in p-A collisions.

CHAPTER 5

Model for J/ψ suppression from parton energy loss.

Contents

5.1 Main assumptions

In this chapter we study the suppression of the quarkonium traversing the nucleus. For the energy loss derived in Chapter 4 to be applicable we need to make a few assumptions. First of all, we assume that the $Q\bar{Q}$ pair of mass M is produced in a compact color octet state and remains octet for a long time. If the production time of the pair is $\tau_{Q\bar{Q}} \sim 1/M$, then $\tau_{octet} \gg \tau_{Q\bar{Q}}$. In the target nucleus rest frame, those proper times are Lorentz-dilated by a factor E/M, where E is the $Q\bar{Q}$ energy in the nucleus rest frame. In this frame our assumption reads

$$t_{hard} \equiv t_{Q\bar{Q}} \sim \frac{E}{M^2} \ll t_{octet} \sim \tau_{octet} \cdot \frac{E}{M} \tag{5.1}$$

Diagrammatically it can be seen on Fig.5.1. In the target rest frame, the pair production looks like gluon splitting. Once created the pair propagates through the nucleus as a compact color octet state, and still lives as a color octet for a long time. Our assumption $t_{octet} \gg t_{hard}$ holds in the CEM, COM, or in any quarkonium production model where color neutralization of the $Q\bar{Q}$ pair is realized late, for instance by rescattering on comovers.

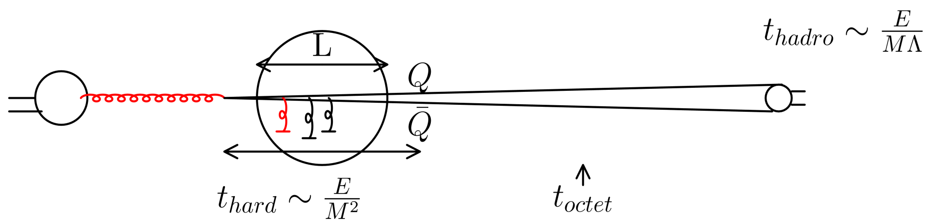

Figure 5.1: Generic process $gg \to Q\bar{Q}$ for quarkonium production in the nucleus rest frame.

Considering the limit $E \gg p_\perp$, quarkonium hadroproduction thus looks like a scattering of an asymptotic color charge. Concentrating on the associated gluon radiation with large formation time $t_{hard} \ll t_f \ll t_{octet}$, the radiation spectrum is thus similar to the spectrum calculated in the previous chapter. And the spectrum in p-A collisions will be the same with the replacement $q_\perp^2 \to \Delta q_\perp^2$.

In quarkonium production models other than the CSM, t_{octet} usually coincides with the hadronization time t_{hadron}, where

$$t_{hadro} = \tau_{hadro} \frac{E}{M} \sim \frac{1}{M_{\psi'} - M_{\psi}} \cdot \frac{E}{M} \tag{5.2}$$

For our partonic description to be valid, we need to restrict to

$$t_{hadro} \geqslant L \Leftrightarrow E \geqslant M \cdot \frac{L}{\tau_{hadro}} \Leftrightarrow x_F \geqslant x_F^{critical} \tag{5.3}$$

where the relation between E and x_F is given in (5.12) below. The model described in the next section applies to $x_F \geqslant x_F^{critical}$. When $x_F \leqslant x_F^{critical}$, nuclear absorption of the fully formed bound state comes into play, as described in Chapter 3.

5.2 Main equation

The initial idea of the model is to express the cross section of the charmonium differential production cross section in $p-A$ collisions simply as that in $p-p$, with a shift in x_F accounting for the energy loss ε occuring due to the propagation of the octet $c\bar{c}$ pair through the nucleus,

$$\frac{1}{A}\frac{d\sigma_{pA}^{\psi}}{dx_F}(x_F, \sqrt{s}) = \int_0^{\varepsilon_{max}} d\varepsilon P(\varepsilon, E)\frac{d\sigma_{pp}^{\psi}}{dx_F}(x_F + \delta x_F(\varepsilon), \sqrt{s}) \tag{5.4}$$

Here $P(\varepsilon, E)$ is a quenching weight, which is described in detail in the next section.

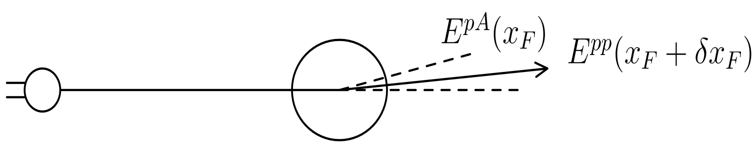

Figure 5.2: Shift in x_F for a particle crossing a nucleus as compared to a proton.

If E is the energy of the J/ψ and $E_p \simeq s/(2m_p)$ is the energy of the projectile proton, then from energy conservation $\varepsilon_{max} = E_p - E$. x_F is the momentum fraction of the projectile proton carried by the charmonium in the c.m. frame of an elementary $p-N$ collision, and is related to the J/ψ transverse mass and rapidity y' in the c.m. frame,

$$x_F \equiv \frac{p'_{||}}{p'_{p||}} = \frac{2M_\perp \sinh y'}{\sqrt{s}}; \quad M_\perp \equiv \sqrt{M^2 + p_\perp^2}; \quad y' \equiv \frac{1}{2}\ln\left(\frac{E'+p'_{||}}{E'-p'_{||}}\right) \tag{5.5}$$

The energy loss ε is more conveniently defined in the nucleus rest frame. Since x_F is defined in the c.m. frame, it is important to obtain kinematical expression relating the two frames. Rapidity is related to energy and momentum as follows:

$$E = M_\perp \cosh y \tag{5.6}$$

$$p^z = M_\perp \sinh y \tag{5.7}$$

Since rapidity is additive under a longitudinal boost: $y = y' + \Delta y$, (5.6) can be re-written as:

$$E = M_\perp \cosh y = M_\perp \cosh(y' + \Delta y) \tag{5.8}$$

Δy can be trivially derived from basic Lorentz transformation. We know that energy and momentum transform as,

$$E' = \gamma(E - \beta p_z) \tag{5.9}$$

$$p'_z = \gamma(p_z - \beta E) \tag{5.10}$$

where β is the velocity of the boost relating the center-of-mass frame and the nucleus rest frame. Putting (5.9) and (5.10) back into (5.5), one obtains,

$$y = y' + \frac{1}{2}\ln\left(\frac{1+\beta}{1-\beta}\right) \Rightarrow \Delta y = \frac{1}{2}\ln\left(\frac{1+\beta}{1-\beta}\right) \tag{5.11}$$

Using (5.8) and $\cosh \Delta y = \frac{\sqrt{s}}{2m_p}$ we get the expression for the energy of the produced particle,

$$E = E(x_F) = E_p\left[\frac{x_F}{2} + \sqrt{\left(\frac{x_F}{2}\right)^2 + \frac{M_\perp^2}{s}}\right]. \tag{5.12}$$

(5.12) can be inverted to

$$x_F = x_F(E) = \frac{E}{E_p} - \frac{E_p}{E}\frac{M_\perp^2}{s}. \tag{5.13}$$

Thus, the shift in x_F appearing (5.4) is defined by

$$x_F(E) + \delta x_F(\varepsilon) \equiv x_F(E+\varepsilon) = \frac{E+\varepsilon}{E_p} - \frac{E_p}{E+\varepsilon}\frac{M_\perp^2}{s} \tag{5.14}$$

At large $x_F \gg M_\perp/\sqrt{s}$, we have $E \simeq x_F E_p$, and $\delta x_F \simeq \varepsilon/E_p$.

5.3 Quenching Weight

The quenching weight $\mathcal{P}(\varepsilon)$ is a crucial quantity in (5.4). It is commonly constructed using the Poisson approximation as follows [58]:

$$\mathcal{P}(\varepsilon, E) = \sum_{n=0}^{\infty} \frac{1}{n!}\left[\prod_{i=1}^{n}\int d\omega_i \frac{dI(\omega_i)}{d\omega}\right] \times \delta\left(\varepsilon - \sum_{i=1}^{n}\omega_i\right) \exp\left\{-\int d\omega \frac{dI}{d\omega}\right\}. \tag{5.15}$$

The Poisson approximation takes into account the radiation of any number of gluons but assumes independent successive emissions. One can easily check that (5.15) satisfies the equation:

$$\frac{\partial \mathcal{P}(\varepsilon, E)}{\partial L} = \int_0^\infty d\omega [\mathcal{P}(\varepsilon-\omega, E) - \mathcal{P}(\varepsilon, E)] \frac{dI}{d\omega dL} \,. \tag{5.16}$$

Here L stands for any parameter that appears in the expression of $dI/d\omega$, thus we can think of it as the size of the medium. (5.16) was originally used in the study of ionization losses [59]. It can be easily proved. If we differentiate (5.15) with respect to L, we get

$$\begin{aligned} \frac{\partial \mathcal{P}(\varepsilon, E)}{\partial L} &= -\int d\omega \frac{dI}{d\omega dL} \mathcal{P}(\varepsilon) + e^{-I} \sum_{n=1}^{\infty} \frac{1}{(n-1)!} \int d\omega \frac{dI(\omega)}{d\omega dL} \\ &\times \prod_{i=1}^{n-1} d\omega_i \frac{dI}{d\omega_i} \delta(\varepsilon - \omega - \sum_{i=1}^{n-1} \omega_i) \end{aligned} \tag{5.17}$$

$$\mathcal{P}(\varepsilon - \omega) \equiv e^{-I} \sum_{n=1}^{\infty} \frac{1}{(n-1)!} \prod_{i=1}^{n-1} d\omega_i \frac{dI}{d\omega_i} \delta(\varepsilon - \omega - \sum_{i=1}^{n-1} \omega_i) \tag{5.18}$$

taking into account (5.18) in (5.17), one easily obtains (5.16).

In our model, we are interested in the radiation with large formation times $t_f(\omega_i) \gg L$. If some radiated gluons have energies of the same order $\omega_i \sim \omega_j$, it implies $t_f(\omega_i) \sim t_f(\omega_j)$, thus emissions are not independent and the Poisson approximation (5.15) is not valid. Therefore, we need to impose a condition for the radiated gluons to be well separated, i.e., in (5.15) we assume

$$\omega_{i_1} \ll \omega_{i_2} \ll \cdots \ll \omega_{i_n} \tag{5.19}$$

With this condition, (5.15) can be re-written as,

$$\mathcal{P}(\varepsilon) = e^{-I} \sum_{n=0}^{\infty} \frac{n}{n!} \left(\prod_{i=1}^{n} \int d\omega_i \frac{dI}{d\omega_i} \right) \delta(\varepsilon - \omega_n) \tag{5.20}$$

This leads to,

$$\begin{aligned} \mathcal{P}(\varepsilon) &= e^{-I} \sum_{n=1}^{\infty} \frac{1}{(n-1)!} \left(\frac{dI}{d\varepsilon} \right) \prod_{i=1}^{n-1} \int_0^\varepsilon d\omega_i \frac{dI(\omega_i)}{d\omega_i} \\ &= \frac{dI}{d\varepsilon} \exp\left\{ -\int_0^\infty d\omega' \frac{dI}{d\omega'} \right\} \exp\left\{ \int_\omega^\infty d\omega' \frac{dI}{d\omega'} \right\} \\ &= \frac{dI}{d\varepsilon} \exp\left\{ -\int_\varepsilon^\infty d\omega' \frac{dI}{d\omega'} \right\} \end{aligned} \tag{5.21}$$

In (5.21) the first factor $dI/d\varepsilon$ stands for the probability to radiate a gluon with $\omega_n = \varepsilon$, the second factor is the probability to have no extra radiation with energies $\omega_j \gtrsim \varepsilon$. It is common to call the second factor a Sudakov factor. Below one can see a plot of $P(\varepsilon)$, see Fig. 5.3.

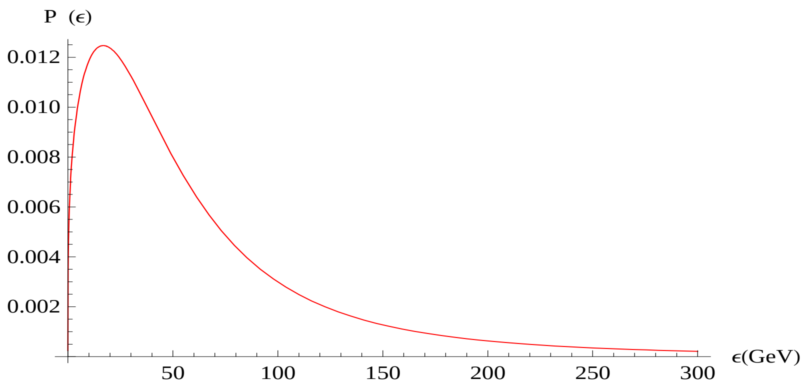

Figure 5.3: $\mathcal{P}(\varepsilon)$ versus the radiated gluon energy ε. Calculations were done with $E_p = 800$ GeV, $M_\perp = 3.25$ GeV, $A = 194$ (tungsten), $\hat{q} = 0.1$.

It can be easily verified that $E\mathcal{P}(\varepsilon, E)$ is a scaling function of ε/E. The crucial quantity that enters (5.21) is $dI/d\omega$, which was discussed in Chapter 4,

$$\begin{aligned}\frac{dI}{d\omega} &= \frac{1}{\omega}\frac{N_c\alpha_s}{\pi}\left\{\ln\left(1+\frac{E^2}{\omega^2}\frac{\Delta q_\perp^2}{M_\perp^2}\right) - \ln\left(1+\frac{E^2\Lambda^2}{\omega^2 M_\perp^2}\right)\right\} \\ &= \frac{1}{\omega} f\left(\frac{\omega}{E}\right)\end{aligned} \tag{5.22}$$

Re-expressing (5.21) in terms of (5.22), we obtain:

$$\mathcal{P}(\varepsilon, E) = \frac{1}{\varepsilon} f\left(\frac{\varepsilon}{E}\right)\exp\left\{-\int_\varepsilon^E \frac{d\omega}{\omega} f\left(\frac{\omega}{E}\right)\right\} \tag{5.23}$$

Introducing the variable $x = \omega/E$ we obtain:

$$E\mathcal{P}(\varepsilon, E) = \frac{E}{\varepsilon} f\left(\frac{\varepsilon}{E}\right)\exp\left\{-\int_{\frac{\varepsilon}{E}}^1 \frac{dx}{x} f(x)\right\} \tag{5.24}$$

which proves that $E\mathcal{P}(\varepsilon, E)$ is a scaling function of the single variable ε/E.

5.4 Fragmentation function

As shown above, $P(\varepsilon)$ has the form

$$\mathcal{P}(\varepsilon, E) = \frac{1}{E}\hat{\mathcal{P}}\left(\frac{\varepsilon}{E}\right) = \frac{1}{E}\hat{\mathcal{P}}\left(\frac{1-z}{z}\right), \tag{5.25}$$

where $z \equiv \frac{E}{E+\varepsilon}$ is interpreted as the "fragmentation variable" of the compact $c\bar{c}$ pair in the energy loss process $E+\varepsilon \to E$. Let us express (5.4) in terms of z. The integration bounds change as follows,

$$\varepsilon = 0 \Rightarrow z = 1 \tag{5.26}$$

$$\varepsilon = \varepsilon_{max} = E_p - E \Rightarrow z = z_{min}\frac{E}{E_p} \simeq x_F \tag{5.27}$$

$$x_F + \delta x_F(\varepsilon) \Rightarrow x_F\left[\frac{E(x_F)}{z}\right] \tag{5.28}$$

The expression (5.4) becomes

$$\frac{1}{A}\frac{d\sigma_{pA}}{dx_F} = \int_{E(x_F)/E_p}^{1}\left|\frac{d\varepsilon}{dz}\right| dz\frac{1}{E}\hat{\mathcal{P}}\left(\frac{1-z}{z}\right)\frac{d\sigma_{pp}}{dx_F}\left(x_F\left[\frac{E(x_F)}{z}\right]\right) \tag{5.29}$$

Using $\varepsilon = E\frac{1-z}{z}$, (5.29) turns into

$$\frac{1}{A}\frac{d\sigma_{pA}^{\psi}}{dx_F} = \int_0^1 dz\mathcal{F}_{loss}(z)\frac{d\sigma_{pp}^{\psi}}{dx_F}\left(x_F\left[\frac{E(x_F)}{z}\right], \sqrt{s}\right), \tag{5.30}$$

where $\mathcal{F}_{loss}(z) = \frac{1}{z^2}\hat{\mathcal{P}}\left(\frac{1-z}{z}\right)$.

In the form (5.30), the energy loss model is simply interpreted as follows: the production of a $c\bar{c}$ pair of energy $E(x_F)$ in p-A collisions proceeds *as if* it is produced in p-p with energy $E(x_F)/z$, followed by "fragmentation" with variable z.

With the energy loss model written in the form (5.30), one can easily verify that the model applies not only to quarkonium production, but also to processes involving non-perturbative fragmentation. To prove that, let us recall that the p-p cross section measured in the experiment is calculated as

$$\frac{d\sigma_{pp}}{dx_F}(x_F) = \int_{E(x_F)/E_p}^{1} dz\,\mathcal{D}(z)\frac{d\hat{\sigma}}{dx_F}\left(x_F\left[\frac{E(x_F)}{z}\right]\right) \tag{5.31}$$

with $D(z)$ a standard non-perturbative fragmentation function. Diagrammatically, the parton production and its fragmentation can be seen Fig. 5.4.

In $p-A$ assuming $t_f \ll t_{hadro}$, medium-induced radiation and hadronization involve separate time scales, suggesting the two processes can be factorized. This leads to the following expression for the $p-A$ cross section,

$$\frac{1}{A}\frac{d\sigma_{pA}}{dx_F}(x_F) = \int_{E(x_F)/E_p}^{1} dzD(z)\int_{E(x_F)/(zE_p)}^{1} dz'\mathcal{F}_{loss}(z')\frac{d\hat{\sigma}}{dx_F}\left(x_F\left[\frac{E(x_F)}{zz'}\right]\right) \tag{5.32}$$

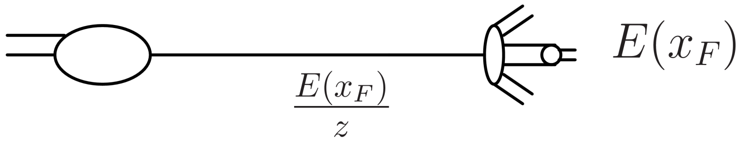

Figure 5.4: $p - p$ production process with non-perturbative fragmentation.

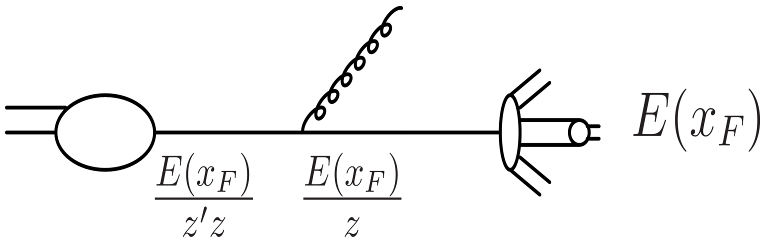

Figure 5.5: Medium-induced radiation followed by non-perturbative fragmentation in $p - A$ collisions.

The schematical description of medium-induced radiation followed by hadronization in $p - A$ collisions is shown in Fig. 5.5. In (5.32) the order of integration can be easily changed, which leads to,

$$\frac{1}{A}\frac{d\sigma_{pA}}{x_F}(x_F) = \int_{E(x_F)/E_p}^{1} dz' \mathcal{F}_{loss}(z') \frac{d\sigma_{pp}}{dx_F}\left(x_F\left[\frac{E(x_F)}{z'}\right]\right) \tag{5.33}$$

We see that (5.33) is identical to (5.30). We conclude that once $d\sigma_{pp}/dx_F$ is given as an input (for instance it can be borrowed from the pp data, see next section), the medium-induced loss is accounted for by the "energy loss fragmentation function" $F_{loss}(z)$, even when the p-p cross section involves non-perturbative fragmentation.

5.5 Cross section

5.5.1 Parametrization

As was mentioned in Chapter 2, there exist many models trying to describe quarkonium production. In our model a crucial ingredient is the single differential cross section $d\sigma^{\psi}_{pp}/dx_F$ of quarkonium production in p-p collisions at a given center-of-mass energy. To remain as model independent as possible, we use the cross section extracted from experiment. We choose to parametrize the $p-p$ cross section as:

$$\frac{d\sigma_{pp}^{\psi}}{dx_F}(x_F) \propto (1-x')^n/x'; \quad x' \equiv \sqrt{x_F^2 + 4M_\perp^2/s} \tag{5.34}$$

Here the exponent n is extracted from the experiment. In a heuristic way, I now explain why such a parametrization might be reasonable.

Consider quarkonium production in a $2 \to 1$ process, namely $gg \to c\bar{c} \to J/\psi$, see Fig. 5.6.

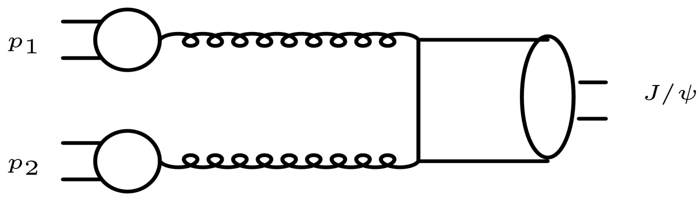

Figure 5.6: J/ψ production in $gg \to c\bar{c} \to J/\psi$.

Due to the kinematics of the process, one can write,

$$(x_1p_1 + x_2p_2)^2 = M^2 \Rightarrow 2x_1x_2p_1p_2 = x_1x_2s = M^2 \Rightarrow x_1x_2 = \frac{M^2}{s} \tag{5.35}$$

Here $x_{1(2)}$ is the momentum fraction of the first (second) gluon,

$$x_1 = \frac{x_F + \sqrt{x_F^2 + \frac{4M_\perp^2}{s}}}{2}; \quad x_2 = \frac{-x_F + \sqrt{x_F^2 + \frac{4M_\perp^2}{s}}}{2}; \quad x_F = x_1 - x_2\ . \tag{5.36}$$

The production cross section of the process described in Fig. 5.6 can be written schematically as

$$\sigma_{pp} \sim \int dx_1 f_{g/p}(x_1) \int x_2 f_{g/p}(x_2)\delta(x_1x_2 - \frac{M_\perp^2}{s})\dots \tag{5.37}$$

The gluon distribution functions $f_{g/p}(x_i)$ typically behave as $\sim (1-x_i)^n/x_i$, which form mimics the behavior of $f_{g/p}(x_i)$, at both $x_i \to 1$ at $x_i \to 0$. Inserting into (5.37) the identity

$$1 = \int dx_F\, \delta(x_1 - x_2 - x_F) \tag{5.38}$$

we obtain:

$$\sigma_{pp} \sim \int dx_F \int dx_1 \int dx_2 \frac{(1-x_1)^n}{x_1}\frac{(1-x_2)^n}{x_2}\delta(x_1x_2 - \frac{M_\perp^2}{s})\delta(x_1 - x_2 - x_F)\dots \tag{5.39}$$

The product of delta functions in (5.39) can be expressed as $\delta(x_2 - \frac{M_\perp^2}{x_1 s})\delta(x_1^2 - x_F x_1 - \frac{M_\perp^2}{s})$. Using now

$$\delta(x_1^2 + x_F x_1 - \frac{M_\perp^2}{s})\delta(f(x_1)) = \frac{\delta(x_1 - r_-)}{|2r_- - x_F|} + \frac{\delta(x_1 - r_+)}{|2r_+ - x_F|} = \\ = \frac{\delta(x_1 - r_-) - \delta(x_1 - r_+)}{\sqrt{x_F^2 + \frac{4M^2}{s}}} \tag{5.40}$$

where

$$r_\pm = \frac{1}{2}\left(x_F \pm \sqrt{x_F^2 + \frac{4M_\perp^2}{s}}\right) \quad , \tag{5.41}$$

we obtain:

$$\frac{d\sigma_{pp}}{dx_F} \sim \frac{(1-r_+)^n(1-r_-)^n}{\sqrt{x_F^2 + \frac{4M_\perp^2}{s}}} \quad . \tag{5.42}$$

Writing now $(1 - r_+)(1 - r_-) = 1 - r_+ - r_- + r_+ r_- \simeq 1 - r_+ - r_-$ we obtain

$$\frac{d\sigma_{pp}}{dx_F} \sim \frac{(1-x')^n}{x'} \quad . \tag{5.43}$$

5.5.2 Fitting the data

The normalization factor in (5.34) is irrelevant in our study, since we are interested in the ratio of cross sections. Using (5.34), the fit to various data for the $p - p$ ($\pi^- - p$) cross section was done. The parameters n obtained for various experiments at different center-of-mass energies are summarized in the Tables 5.1 and 5.2 for J/ψ, and in Table 5.3 for Υ.

Experiment	NA3	E789	HERA-B	PHENIX	ALICE
$\sqrt{s}$(GeV)	19.4	38.7	41.5	200	7000
n	4.3	4.5 ± 0.06	5.7 ± 0.2	8.3 ± 1.1	32.3 ± 7.5

Table 5.1: Values of n extracted from J/ψ production in $p-p$ collisions. Data taken from [60], [61], [62], [63], [64].

One can see that the chosen parametrization agrees quite well with the experimental data, see for example Figs. 5.7 and 5.8.

Experiment	NA3	NA3	NA3
$\sqrt{s}$(GeV)	16.8	19.4	22.9
n	1.4	1.4	1.5

Table 5.2: Values of n extracted from J/ψ production in $\pi^- - p$ collisions [60].

Experiment	E866	PHENIX	LHC-b
$\sqrt{s}$(GeV)	38.7	200	7000
n	3.4 ± 0.2	6.7 ± 1.0	14.2 ± 2.9

Table 5.3: Values of n extracted from Υ production in $p - p$ collisions.

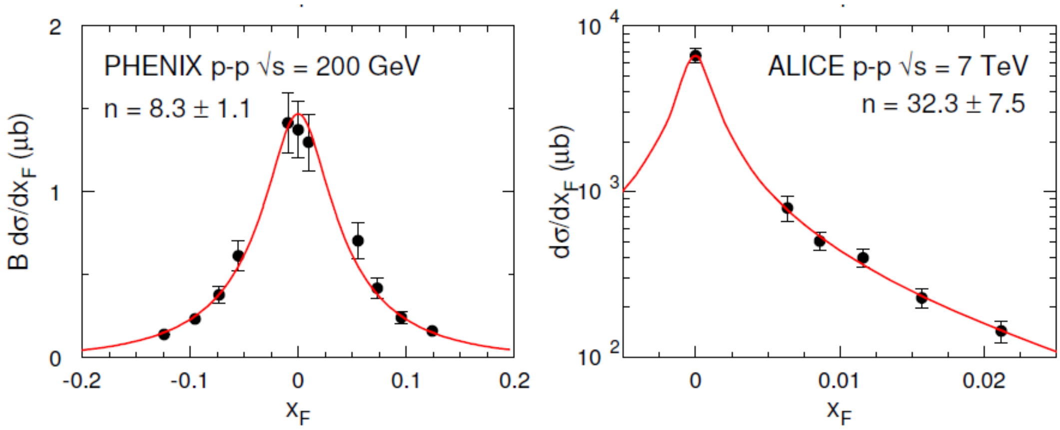

Figure 5.8: Comparison between J/ψ production data in p–p collisions at RHIC and LHC and the fit (5.34), shown by the solid red line. Data taken from [63], [64].

The observed agreement indicates that (5.34) can be safely used to calculate quarkonium suppression.

5.6 Effective length

The effective length travelled by the compact $c\bar{c}$ pair inside the nucleus enters our model through the expression of the nuclear broadening. Below we derive the effective length in the hard sphere approximation and for more realistic nuclear profiles.

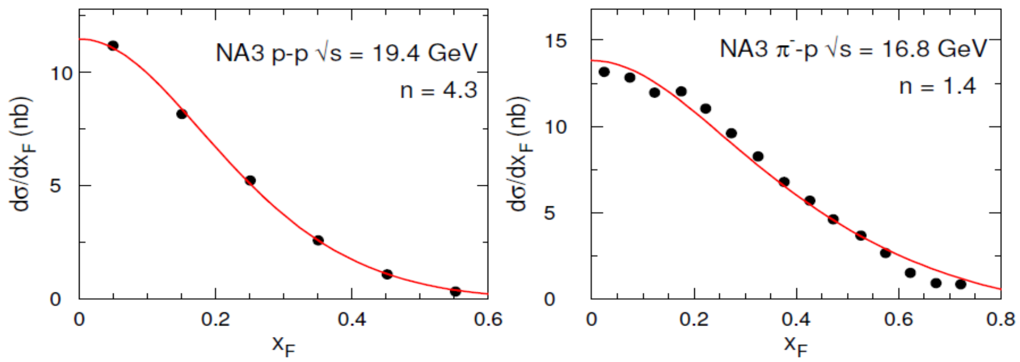

Figure 5.7: Comparison between J/ψ production data in p-p, π^--p collisions and the parametrization (5.34), shown by the solid red line. Data taken from [60].

5.6.1 Hard sphere approximation

Let us model the nucleus by a hard sphere, and consider a proton crossing the nucleus along the direction z, see Fig. 5.9.

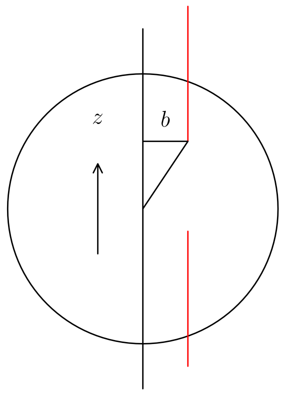

Figure 5.9: $p - A$ collision in the hard sphere approximation.

Here b is the impact parameter. From Fig.5.9 it is obvious that the bounds for z are $\pm\sqrt{R^2 - b^2}$, thus the average of the length crossed by the $c\bar{c}$ can be derived as (defining $L(b) = 2\sqrt{R^2 - b^2}$):

$$< L >= \frac{\int d^2\vec{b}dzL(b)}{d^2\vec{b}dz} = \frac{1}{V}\int 2\pi bdb \int_{-L(b)/2}^{L(b)/2} dzL(b)$$
$$= \frac{4\pi}{V}\left[R^4 - \frac{b^4}{2}\right]\Big|_0^R = \frac{3}{2}R, \tag{5.44}$$

where $V = \frac{4}{3}\pi R^3$ for a hard sphere.

5.6.2 Realistic nuclear profiles

Basics of Glauber model

To calculate the length with realistic nuclear profiles, we need to review some basics of the Glauber model. Let us consider two nuclei colliding as in Figure 5.11. The Glauber model views the interaction of nuclei in terms of the interaction of its constituents. Its main assumption is that all the nucleon-nucleon interactions are considered to be independent of each other. One can then derive important quantities in terms of the basic nucleon-nucleon cross section [65].

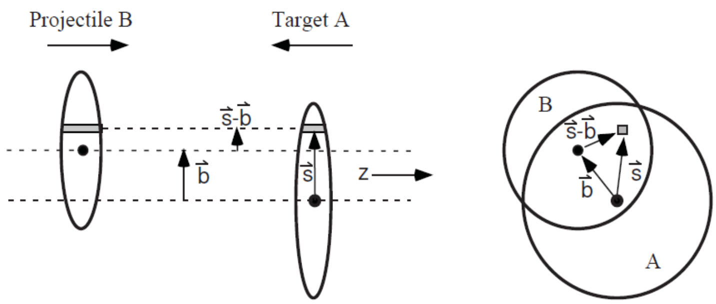

Figure 5.10: Schematic representation of the Glauber Model geometry [65].

Let us consider two heavy ions, "target A" and "projectile B", that are colliding at relativistic speed with impact parameter b. We will focus on the two flux tubes, located at a distance $\vec{s}$ from the center of the target nucleus and at a distance $\vec{s} - \vec{b}$ from the center of the the projectile (Fig.5.11). During the collision these tubes overlap. The probability density to find a nucleon in the target flux tube is called the "the thickness function" is

$$T_A(\vec{s}) = \int \rho_A(\vec{s}, z)dz \tag{5.45}$$

where $\rho_A(\vec{s}, z)$ is the probability per unit volume, normalized to A, for finding the nucleon at location $(\vec{s}, z)$

$$\int d^2\, \vec{s} T_A(\vec{s}) = A. \tag{5.46}$$

For large nuclei, it is common to use two-parameter Wood-Saxon density profile for ρ_A [65],

$$\rho_{WS} = \frac{n_0}{1 + \exp\left[\frac{\sqrt{\vec{s}^2+z^2}-R_A}{d}\right]} \tag{5.47}$$

where $d = 0.54$ fm, $R_A = 1.12 A^{1/3}$, n_0 can be found from the normalization condition for ρ_A, namely $\int dV \rho_A(\vec{s}, z) = A$.

A similar expression to (5.45) can be written for the projectile nucleus B. The product $T_A(\vec{s}) T_B(\vec{s} - \vec{b}) d^2\vec{s}$ is the probability per unit area of nucleons being located in the respective overlapping target and projectile flux tubes of area $d^2\vec{s}$. The product is normalized as

$$T_{AB}(\vec{b}) = \int d^2\vec{s} T_A(\vec{s}) T_B(\vec{s} - \vec{b}); \quad \int d^2\vec{b} T_{AB}(\vec{b}) = A\, B \tag{5.48}$$

In $p - A$ collisions, $\vec{b} \simeq \vec{s}$, (5.48) simplifies to

$$T_{AB}(\vec{b}) = \int d^2\vec{s}\; T_A(\vec{s})\; T_B(\vec{s} - \vec{b}) \underset{B \ll A}{\simeq} \int d^2\vec{s}\; T_A(\vec{b})\; T_B(\vec{s} - \vec{b}) \simeq B T_A(\vec{b}) \tag{5.49}$$

In $p - A$ collisions $B = 1$, thus $T_{AB}(\vec{b}) = T_A(\vec{b})$. The number of binary collisions in $p - A$ is defined as,

$$N_{coll}(b) = T_A(b) \sigma_{in}^{NN} \tag{5.50}$$

Here σ_{in}^{NN} is the nucleon-nucleon inelastic cross section, which is a measured quantity, providing the only non-trivial beam energy dependence for Glauber calculations. From $\sqrt{s} \sim 20$ GeV (CERN, SPS) to $\sqrt{s} = 200$ GeV (RHIC) σ_{in}^{NN} increases from ~ 32 mb to ~ 42 mb.

Derivation of the effective length

In our model, the length enters through the amount of soft rescattering, given by

$$l_\perp^2 = \hat{q} L \tag{5.51}$$

As we already mentioned in Chapter 3, $\hat{q} \propto \rho x G(x)$. We can extract the ρ dependence as follows

$$\hat{q} \equiv \hat{q}(x) \frac{\rho}{\rho_0}, \tag{5.52}$$

where $\hat{q}(x)$ is the value of $\hat{q}$ when $\rho = \rho_0$, with ρ_0 an arbitrary (constant) nuclear number density. Using the fact that $xG(x) \sim x^{-0.3}$, one defines $\hat{q}(x) = \hat{q}_0(\frac{10^{-2}}{x})^{0.3}$, here $\hat{q}_0 = \hat{q}(x = 0.01, \rho = \rho_0)$. Since L appears always in the product $\hat{q}L$,

$$l_\perp^2 = \hat{q}L = \hat{q}(x)\frac{\rho L}{\rho_0} \equiv \hat{q}(x)L_{eff} \tag{5.53}$$

where $L_{eff} = \rho L/\rho_0$. We note that the ρ dependence is absorbed by our definition of the effective length L_{eff}. To derive L_{eff} we use the fact that while going from the hard sphere approximation to realistic nuclear profiles, we have the formal replacement:

$$\frac{\rho L}{\rho_0} \to \frac{1}{\rho_0}\int dz\rho(r) = \frac{1}{\rho_0}\int \frac{dN_{part}}{\sigma_{inel}} = \frac{N_{part}}{\rho_0\sigma_{inel}} \tag{5.54}$$

Note that in $p-A$ collisions, the number of binary collisions equals the number of participants. For minimum bias $p-A$ collisions one will need to calculate the average of the number of participants, i.e.,

$$\frac{\rho L}{\rho_0} \to \frac{< N_{part} >}{\rho_0\sigma_{inel}} \tag{5.55}$$

To find the average number of participants, one has to obtain the average number of participating nucleons in the target nucleus for the events with J/ψ production. The corresponding probability distribution can be found using Bayes theorem for conditional probabilities:

$$P(N_{part}|J/\psi) = \frac{P(J/\psi|N_{part})P(N_{part})}{P(J/\psi)} \tag{5.56}$$

Here $P(J/\psi) = \sum_{N_{part}} P(J/\psi|N_{part})P(N_{part})$. In the numerator, the probability of J/ψ production with a given number of participants is:

$$P(J/\psi|N_{part}) = \frac{\sigma_{J/\psi}}{\sigma_{inel}} \tag{5.57}$$

where $\sigma_{J/\psi}$ is the J/ψ production cross section, assumed to satisfy $\sigma_{J/\psi} \ll \sigma_{inel}$. To derive the probability distribution $P(N_{part})$ of the number of participants in $p-A$ collisions, let us recall that probability for an inelastic collision to take place is

$$\frac{N_{bin}^{NA}(b)}{A} = \frac{T_A(b)\sigma_{inel}^{NN}}{A} = \frac{N_{part}(b)}{A} \tag{5.58}$$

The probability of no inelastic collision in A events read

$$p_0(b) = \left(1 - \frac{1}{A}T_A(b)\sigma_{inel}^{NN}\right)^A \overset{A\gg 1}{\simeq} e^{-T_A(b)\sigma_{inel}^{NN}} \tag{5.59}$$

The probability to have at least one inelastic collision is

$$1 - p_0(b) = P(N_{coll} \geq 1) = 1 - e^{-T_A(b)\sigma_{inel}^{NN}} \simeq T_A(\mathbf{b})\sigma_{inel}^{NN} \tag{5.60}$$

Thus the probability distribution for the number of participants is given by,

$$P(N_{part}) = \frac{\int d^2b\binom{A}{N}(\sigma_{in}T_A(\mathbf{b}))^N(1-\sigma_{in}T_A(\mathbf{b}))^{A-N}}{\int d^2\mathbf{b}(1-(1-\sigma_{in}T_A(\mathbf{b}))^A)} \tag{5.61}$$

Here the denominator fixes the right normalization and corresponds to taking into account only events with particle production. Taking into account (5.57),

$$P(J/\psi) = \sum_{N_{part}} \frac{N_p\frac{\sigma_{J/\psi}}{\sigma_{inel}}\int d^2\mathbf{b}\binom{A}{N}(\sigma_{in}T(\mathbf{b})^N)(1-\sigma_{in}T(\mathbf{b}))^{A-N}}{\int d^2\mathbf{b}(1-(1-\sigma_{in}T_A(\mathbf{b}))^A)} \tag{5.62}$$

Using the equality

$$\sum_{N=1}^{A} N\binom{A}{N}p^N(1-p)^{A-N} = Ap, \tag{5.63}$$

one obtains for (5.62),

$$P(J/\psi) = \frac{A\sigma_{J/\psi}}{\int d^2\mathbf{b}(1-(1-\sigma_{in}T(\mathbf{b}))^A)} \tag{5.64}$$

Making all the neccessary substitutions to the initial equation, we get

$$P(N_p|J/\psi) = \frac{N\int d^2\mathbf{b}\binom{A}{N}(\sigma_{in}T(\mathbf{b}))^N(1-\sigma_{in}T(\mathbf{b}))^{A-N}}{A\sigma_{inel}} \tag{5.65}$$

With this distribution, the average number of the number of participants is

$$< N_{part} >_{J/\psi} = \frac{\int d^2\mathbf{b}\sum N_p^2\binom{A}{N}(\sigma_{in}T(\mathbf{b}))^N(1-\sigma_{in}T(\mathbf{b}))^{A-N}}{A\sigma_{inel}} \tag{5.66}$$

If we take into account in (5.66) the following equality

$$\sum_{N=1}^{A} N^2\binom{A}{N}p^N(1-p)^{A-N} = Ap + A(A-1)p^2 \tag{5.67}$$

the expression for the average of the number of participating nucleons is then,

$$< N_{part} >_{J/\psi} = 1 + (A-1)\sigma_{inel}\int d^2\mathbf{b}T(\mathbf{b})^2 \tag{5.68}$$

Knowing the average number of participants, the expression for the effective length is

$$\frac{\rho L}{\rho_0} \to \frac{1}{\rho_0\sigma_{inel}} + \frac{A-1}{A^2\rho_0}\int d^2\mathbf{b}T_A(\mathbf{b})^2 \tag{5.69}$$

One can find L_{eff} calculated in hard sphere approximation and with realistic nuclear densities in Table 5.4. Realistic nuclear densities used to calculate the integral in (5.69) were extracted from [57].

Nucleus	W	W	Fe	Cu
Atomic mass	184	186	56	65
L_{eff} (fm)	9.35	9.48	6.62	6.67
L_{HS}(fm)	9.56	9.58	6.43	6.68

Table 5.4: Effective length versus hard sphere (HS) approximation.

5.7 Phenomenology

5.7.1 Extracting the transport coefficient $\hat{q}_0$

In the previous section, we defined the x and ρ dependence of $\hat{q}$ as follows:

$$\hat{q} = \hat{q}(x)\frac{\rho}{\rho_0}; \quad \hat{q} \equiv \hat{q}_0 \left(\frac{10^{-2}}{x}\right)^{0.3}; \quad x = min(x_0, x_2); x_0 \equiv \frac{1}{2m_p L} \tag{5.70}$$

Thus the only free parameter of the model is $\hat{q}_0 \equiv \hat{q}(x = 10^{-2}, \rho = \rho_0)$. As was discussed in Chapter 4, the value of x depends on the kinematics of the process. When $t_{hard} \gg L$ we expect $x \sim x_2$, and assuming $2 \to 1$ subprocess kinematics $x_2 = (-x_F + x')/2$.

$\hat{q}_0$ was extracted from the E866 data, by comparing quarkonium suppression in $p - W$ to $p - Be$ [66]. The choice of the data is explained by the fact that up to now, it is the most precise data we have. The obtained value is $\hat{q}_0 = 0.075 \pm 0.005\,\text{GeV}^2/\text{fm}$. To estimate the uncertainty, the values of x_F were restrained from 0.3 to 0.7. With this restriction, we obtain $\hat{q}_0 \simeq 0.087\,\text{GeV}^2/\text{fm}$. Below, one can see the plot of J/ψ suppression measured in $p-W$ collisions and the theoretical curve calculated with $\hat{q}_0 = 0.075$. A slight disagreement is observed at $x_F \lesssim 0.1$, since in this region, absorption effects might come into play.

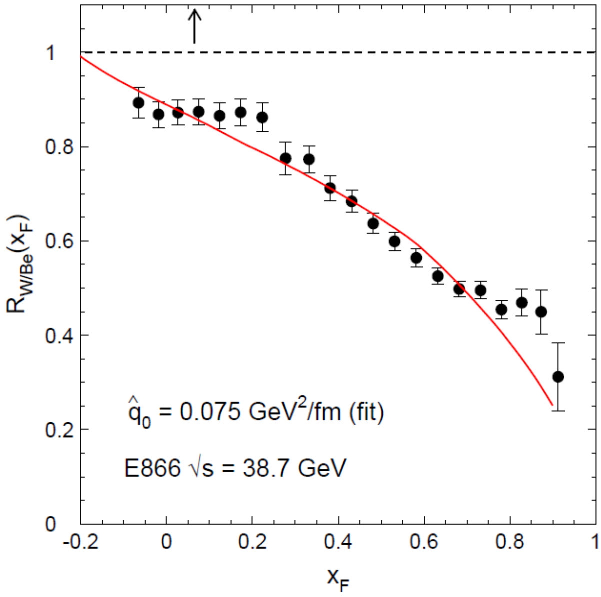

Figure 5.11: J/ψ suppression in $p - W$ collisions and theoretical curve, including energy loss [66].

5.7.2 Comparing the model predictions to J/ψ data

Having defined all the parameters of the model, we are ready to proceed to the predictions of quarkonium suppression. Below are the comparisons between the obtained theoretical curves and the data of various experiments [67].

intermediate energies: E866, NA60, HERA-B

We start by the E866 data and plot J/ψ suppression expected in an iron target, see Fig. 5.12.

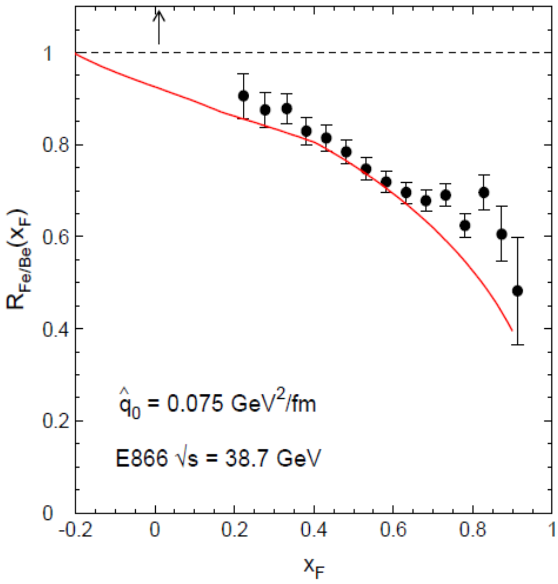

Figure 5.12: J/ψ suppression in $p-Fe$ collisions [66] compared to the energy loss model.

The good agreement shows the efficiency of the model. A slight disagreement is seen at small x_F, but as we mentioned in Chapter 3, nuclear absorption might play a role in this region. The model was tested at various energies. One can see the predictions done for the conditions of the NA3 experiment in Fig. 5.13.

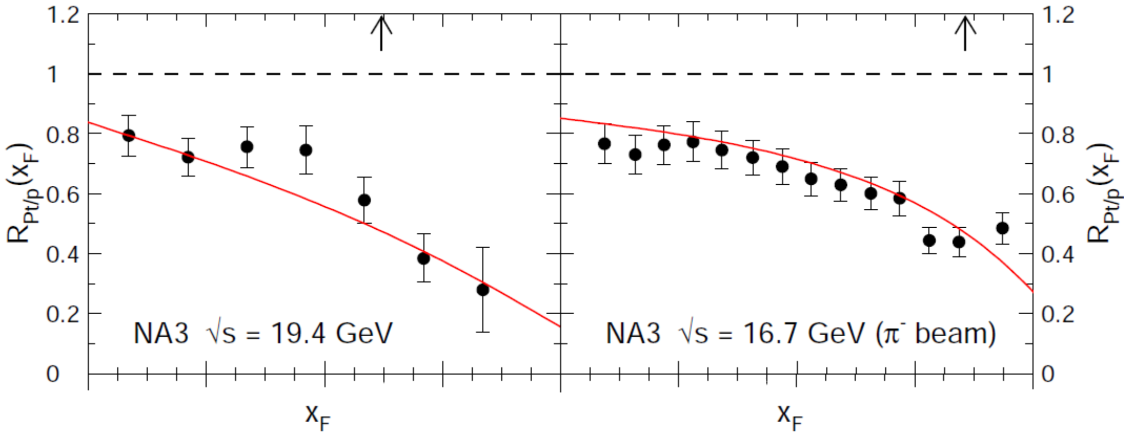

Figure 5.13: NA3 J/ψ suppression data in $p-A$ $(A = Pt)$ and $\pi - A$ collisions compared to the energy loss model [60]. The arrows indicate the x_F^{crit}-the values of x_F corresponding to the hadronization.

It is remarkable, that the model also predicts the J/ψ suppression observed with a π projectile, as can be seen from Fig. 5.13. The smaller suppression in $\pi - A$ can be explained by the flatter shape of the cross section. See the values of n for NA3 in $p-p$ collisions (Table **??**) and in $\pi^- - p$ collisions (Table **??**).

Finally let us show the comparison with HERA-B experiment, see Fig. 5.14.

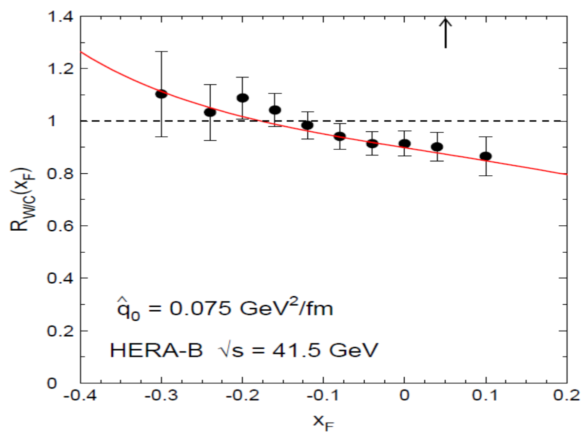

Figure 5.14: HERA-B J/ψ suppression data [62] in $p - A$ collisions compared to the energy loss model.

Due to the small values of x_F probed by HERA-B, one expects J/ψ suppression to be more affected by nuclear absorption (see the location of the arrow on Fig. 5.14). Nevertheless, we still observe a good agreement with data. In particular the enhancement observed at the negative x_F agrees very well with the model.

high energies: RHIC, LHC

The predictions for $d - Au$ collisions at RHIC ($\sqrt{s} = 200$ GeV) are shown in Fig. 5.15. The energy loss model reproduces nicely the J/ψ suppression in a broad rapidity range.

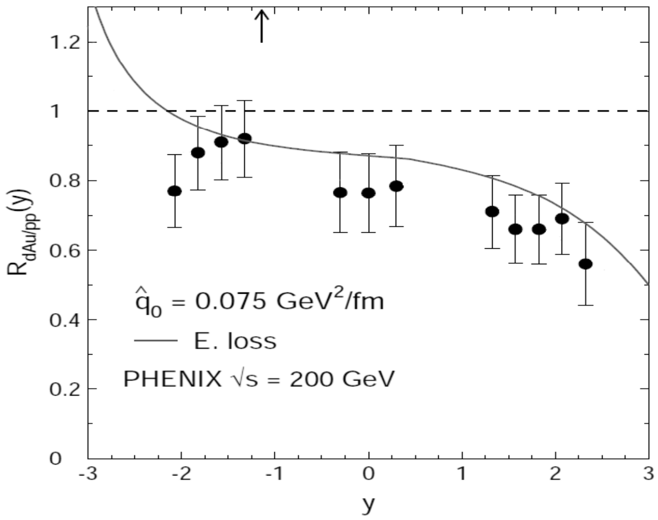

Figure 5.15: PHENIX J/ψ suppression data [68] in $d-Au$ collisions compared to the energy loss model.

Predictions for J/ψ suppression in $p - Pb$ collisions at the LHC ($\sqrt{s}$ = 5TeV) are shown in Fig. 5.16. J/ψ production is significantly suppressed at large positive rapidity. In the target fragmentation region ($y < 0$) the suppression is moderate.

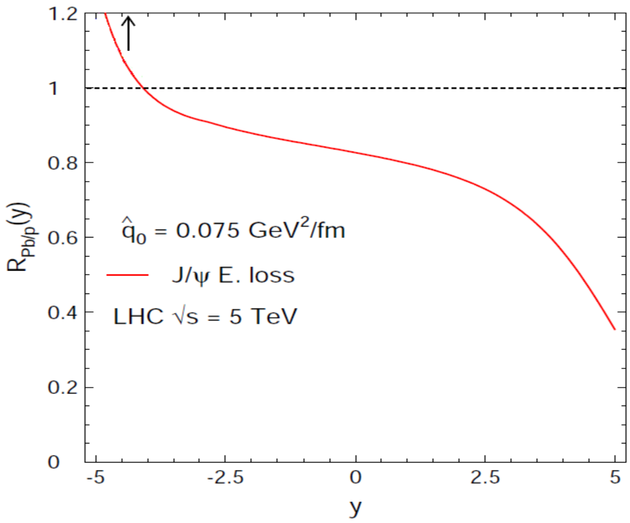

Figure 5.16: J/ψ suppression in $p - Pb$ collisions at LHC, as predicted by the energy loss model.

Our predictions have been compared to the data presented by the ALICE collaboration. The measurement was performed at $\sqrt{s_{NN}} = 5.02\,\text{TeV}$. Below one can see in Fig. 5.17 the plot with the obtained data for R_{pPb}, and various theoretical predictions, including that of the parton energy loss model. At large rapidities one observes a very good agreement between the theory and the data.

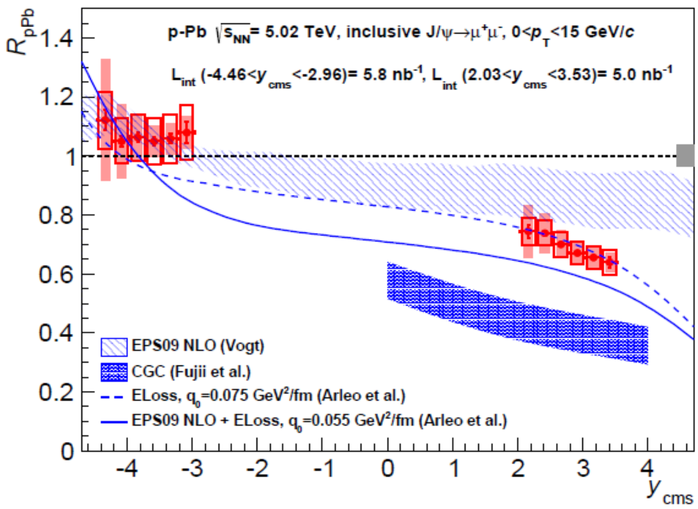

Figure 5.17: The nuclear modification factor for inclusive J/ψ production at $\sqrt{s_{NN}} = 5.02\,\text{TeV}$ in bins of rapidity. The prediction of the parton energy loss model is shown by the dashed blue line [69].

5.7.3 Comparing the model predictions to Υ data

E772

The success of the above predictions supports the energy and length dependence of our model. Let us check whether the mass dependence of the model is also supported by the data, by looking at Υ suppression.

The E772 data for Υ suppression for various nuclear targets (Ca, Fe, W) is shown in Fig. 5.18. A good agreement is found for $x_F > x_F^{crit}$ (below the critical value of x_F, the data is below our predictions). Thus the mass dependence $\sim M^{-1}$ of the energy loss derived in Chapter 4 seems to be consistent with the data.

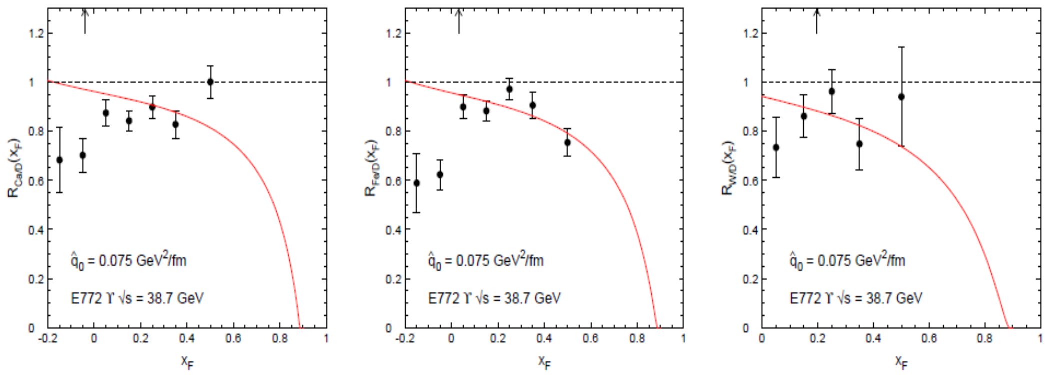

Figure 5.18: E772 Υ suppression data [70] in $p - A$ collisions compared to the energy loss model.

RHIC, LHC

Finally, let us mention the predictions of the energy loss model for Υ at RHIC and LHC. The prediction for the RHIC experiment is shown in Fig. 5.19. As expected, the suppression is less pronounced than for J/ψ production, compare to Fig. 5.15. It is difficult to perform a comparison due to the large uncertainty of the experimental data. Hopefully more precise data will soon allow to see the strength of Υ suppression in cold nuclear matter.

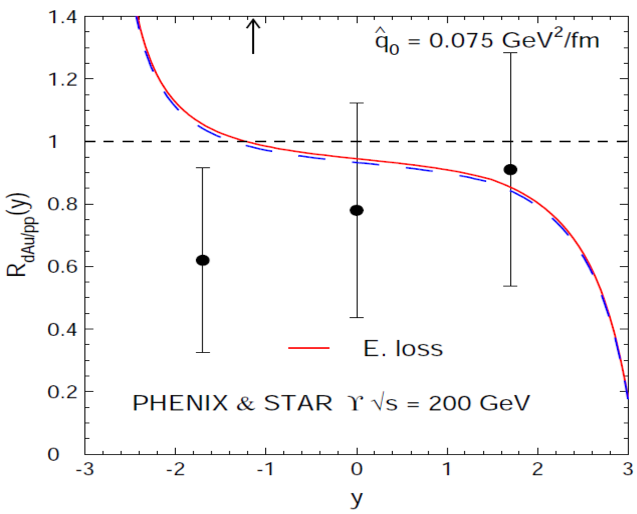

Figure 5.19: PHENIX ($|y|$=1.7) and STAR ($y = 0$) Υ suppression data [71], [72] in $d - Au$ collisions compared to the energy loss model.

In Fig. 5.21 one sees the predictions both for J/ψ and Υ suppression as a function of rapidity. One observes a strong suppression at high y for J/ψ, due to the large center-of-mass energies. The suppression of Υ is less steep due to the mass dependence of energy loss $\sim M^{-1}$. As can be seen from Fig. 5.21, the arrow showing the critical rapidity for J/ψ and Υ is at $y^{crit} \simeq -5$, thus we expect little or no effect of nuclear absorption at LHC.

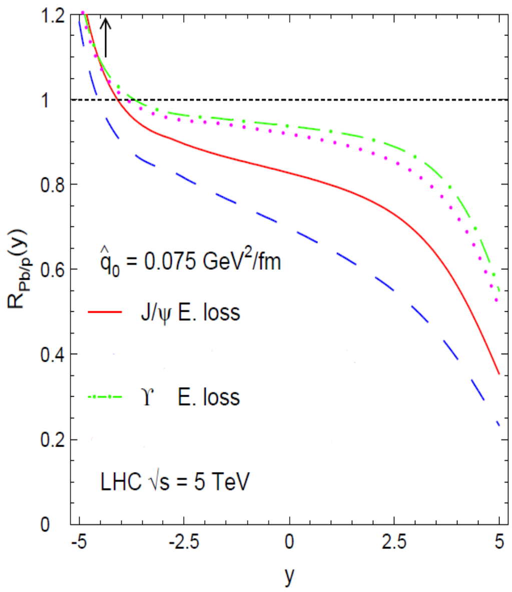

Figure 5.20: Υ and J/ψ suppression from parton energy loss, as predicted for LHC [67].

The comparison between the most recent results presented by the ALICE collaboration and our predictions can be seen in Fig. 5.21. At large rapidity our model underestimates Υ suppression, but as one can see from the large uncertainty of the data no real conclusion can be drawn. Given also the large uncertainty in the global normalization a good agreement with our model is still possible.

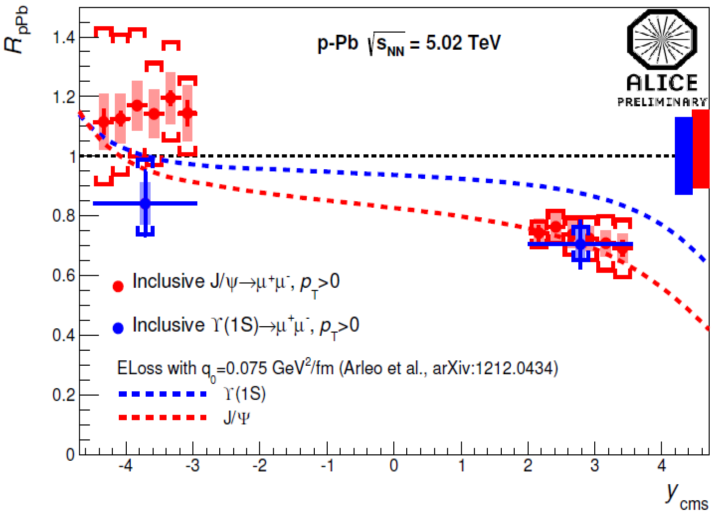

Figure 5.21: Υ and J/ψ suppression versus rapidity. The LHC results versus theoretical curves.

5.8 Suppression as a function of p_T

5.8.1 Preamble: Cronin effect

The Cronin ratio $R(p_T)$ is defined as the ratio of the inclusive differential cross-section $d\sigma/dp_T^2$ for proton scattering on two different targets, normalized to the respective atomic numbers A and B:

$$R(p_T) = \frac{B}{A}\frac{d\sigma_{pA}/dp_T^2}{d\sigma_{pB}/dp_T^2} \tag{5.71}$$

In the absence of nuclear effect one would expect $R(p_T) = 1$, but, for $A > B$ a suppression is observed experimentally at small p_T and an enhancement at moderate p_T, see Fig. 5.23. [1]

[1] In A-A collisions, Cronin effect is considered as one of signals of QGP [73].

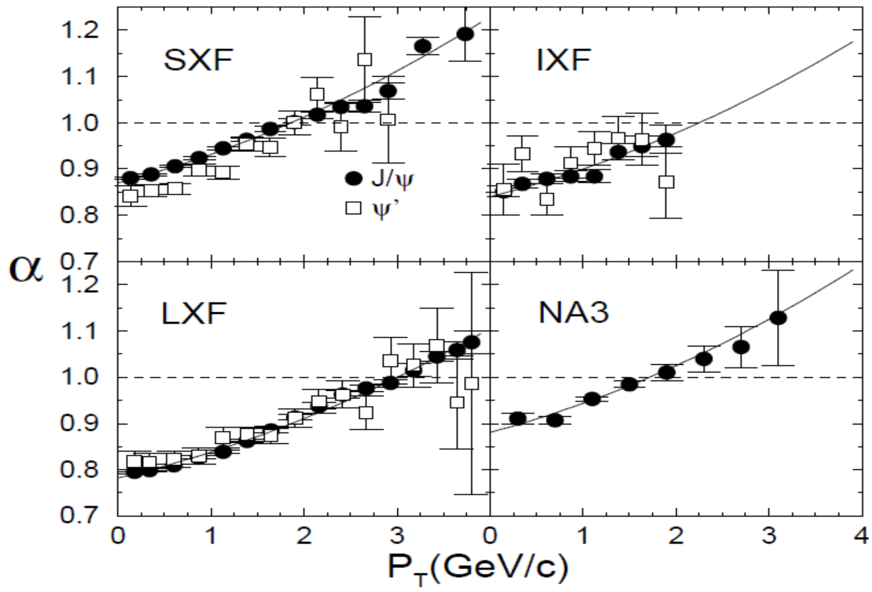

Figure 5.22: Cronin effect observed in $p-A$ collisions, extracted from the E866 experiment [66]. Here, for SXF data α was obtained using Be and W targets, for IXF and LXF data, Be, Fe and W targets were used. The average x_F is respectively $< x_F >= 0.55, 0.308,$ and 0.480. The data from the 200 GeV NA3 experiment is also shown.

As a toy model for the Cronin effect, let us use the $p-p$ cross section as

$$\frac{d\sigma_{pp}}{dp_T^2} \sim \left(\frac{1}{p_T^2}\right)^n \tag{5.72}$$

and the $p-A$ cross section given by:

$$\frac{1}{A}\frac{d\sigma_{pA}}{d^2\vec{p}_T} = \int \frac{d\varphi}{2\pi}\frac{d\sigma_{pp}}{d^2\vec{p}_T}(\vec{p}_T - \Delta\vec{p}_T)\,, \tag{5.73}$$

where $\Delta\vec{p}_T$ is assumed to be uniformly distributed in the transverse (azimuthal) plane, and of fixed modulus of Δp_T. A simple numerical evaluation yields the ratio R_{pA} shown in Fig. 5.23, with all qualitative features of the Cronin effect: $R_{pA} < 1$ at small p_T, $R_{pA} > 1$ at large p_T, and $R_{pA}(p_T) \to 1$ when $p_T \to \infty$.

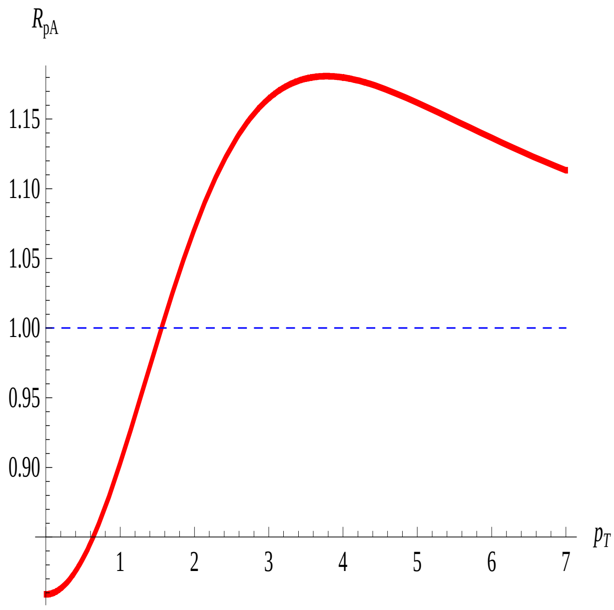

Figure 5.23: Toy model for the description of the Cronin effect, obtained from Eqs. (5.72) and (5.73), using $n = 4$, $\Delta p_T = 0.7\,\text{GeV}$.

In the coming sections, we will implement the Cronin effect in our energy loss model.

5.8.2 Shift in E and p_T

In the following we generalize the model (5.4) by expressing the quarkonium double differential cross section (in p_T and E) in $p-A$ as the one in $p-p$, with a shift E, accounting for the energy loss and with a shift in p_T, standing for the transverse momentum broadening $\Delta\vec{p}_T$. The $p-A$ and $p-p$ cross sections are related as

$$\frac{1}{A}\frac{d\sigma^{\psi}_{pA}}{dEd^2\vec{p}_\perp} = \int_\varphi\int_\varepsilon \mathcal{P}(\varepsilon, E)\frac{d\sigma^{\psi}_{pp}}{dEd^2p_\perp}(E+\varepsilon, \vec{p}_\perp - \Delta\vec{p}_\perp) \tag{5.74}$$

From the previous sections, we know that $\mathcal{P}(\varepsilon, E)$ is the energy loss distribution with the explicit expression given by (5.25). The integral over ε is bounded by $\varepsilon_{max} = min(E_p - E, E)$ where $E_p \simeq s/2m_p$. The additional assumption here is that $\Delta\vec{p}_\perp$ is uniformly distributed in the azimuthal angle φ. The modulus of $\Delta p^2_\perp$ is defined as

$$(\Delta\vec{p}_\perp)^2 = l^2_{\perp A} - l^2_{\perp B} = \hat{q}_A L_A - \hat{q}_B L_B. \tag{5.75}$$

$\hat{q}_A = \hat{q}(x_A) \equiv \hat{q}_0 \left(\frac{10^{-2}}{x_2}\right)^{0.3}$, where $\hat{q}_0$ has been defined in the previous sections of this Chapter, with the value 0.075 GeV^2/fm extracted from the experiment. We will use this value in the current model, which thus will contain no additional free parameter.

(5.74) can be expressed in terms of rapidity, leading to

$$\frac{1}{A}\frac{d\sigma_{pA}^{\psi}}{dyd^2\vec{p}_\perp} = \int_\varphi \int_\varepsilon \mathcal{P}(\varepsilon, E)\left[\frac{E}{E+\varepsilon}\right]\frac{d\sigma_{pp}}{dyd^2\vec{p}_\perp}(E+\varepsilon, \vec{p}_\perp - \Delta\vec{p}_\perp) \tag{5.76}$$

Here we used the fact that

$$y(E, \vec{p}_\perp) = \ln\left(\frac{E}{E_p}\frac{\sqrt{s}}{M_\perp}\right). \tag{5.77}$$

From (5.77), one can find the expression for the energy E of J/ψ:

$$E = E(y, \vec{p}_\perp) = E_p e^y M_\perp/\sqrt{s} \tag{5.78}$$

5.8.3 Parametrization of $p-p$ double differential cross section

Similarly to the previous model, the double differential $p-p$ cross section $d\sigma_{pp}/dyd^2\vec{p}_\perp$ is extracted from experiment in order to remain as model independent as possible. The double cross section of quarkonium production can be parametrized as

$$\frac{d\sigma_{pp}^{\psi}}{dyd^2\vec{p}_\perp} = \mathcal{N}\left(\frac{p_0^2}{p_0^2+p_\perp^2}\right)^m \times \left(1 - \frac{2M_\perp}{\sqrt{s}\cosh y}\right)^n \equiv \mathcal{N} \times \mu(p_\perp) \times \nu(y, p_\perp). \tag{5.79}$$

One can actually check that this form is consistent with the shape used for (5.4). In our previous model, the $p-p$ cross section was parametrized as

$$\frac{d\sigma_{pp}^{\psi}}{dx_F} \propto \frac{(1-x')^n}{x'}. \tag{5.80}$$

To translate (5.80) in rapidity, one performs the change of variable

$$\frac{d\sigma_{pp}^{\psi}}{dy} = \frac{d\sigma_{pp}^{\psi}}{dx_F}\frac{dx_F}{dy} \propto \frac{(1-x')^n}{x'}x' = \left(1 - \frac{2M_\perp}{\sqrt{s}}\cosh y\right)^n = \nu(y, p_\perp), \tag{5.81}$$

where we used the fact that $\partial x_F/\partial y = x'$. In our previous model we used no information on $p_\perp$ distributions, and $p_\perp$ was replaced by some typical value $\bar{p}_\perp = 1$ GeV.

One can easily check that $d\sigma_{pp}/dy$ can be recovered from (5.79) by integrating over $\vec{p}_\perp$,

$$\frac{d\sigma^{\psi}_{pp}}{dy} = \int_{\vec{p}_\perp} \frac{d\sigma^{\psi}_{pp}}{dyd^2\vec{p}_\perp} = \mathcal{N}\int_{\vec{p}_\perp} \mu(p_\perp)\nu(y,p_\perp) \simeq \mathcal{N}\left[\int_{\vec{p}_\perp} \mu(p_\perp)\right]\nu(y,\bar{p}_\perp)\,. \tag{5.82}$$

We used the fact that $\mu(p_\perp)$ decreases much faster than $\nu(y,p_\perp)$ with $p_\perp$. One can see the difference of both functions in Fig 5.24. Thus, the second function can be evaluated at the typical value of $\bar{p}_\perp$. Since (5.82) reproduces (5.81), the double differential parametrization (5.79) is thus consistent with the single differential parametrization used previously in this chapter.

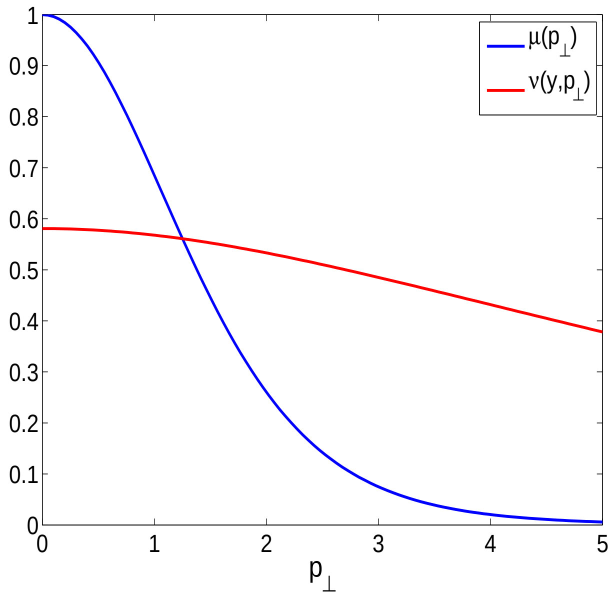

Figure 5.24: p_T dependence of $\mu(p_\perp)$ and $\nu(y,p_\perp)$

The typical value $\bar{p}_\perp$ of $p_\perp$ appearing in (5.82) can be defined as

$$\int_0^{\bar{p}^2_\perp} dp^2_\perp \mu(p_\perp) \equiv \frac{1}{2}\int_0^{\infty} dp^2_\perp \mu(p_\perp) \Rightarrow \bar{p}^2_\perp = \left(2^{\frac{1}{m-1}} - 1\right) p_0^2 \quad (m > 1). \tag{5.83}$$

Extracting the free parameters from the experimental data (see next section), one obtains $\bar{p}_\perp(p_0, m)$ =1.3 - 2.4 GeV.

The values of the parameters p_0, m and n extracted from LHC, RHIC and E789 can be found on Table 5.8.3. At the LHC ($\sqrt{s}$ = 7 TeV) the values of the free parameters were extracted from [63] (Alice), [74] (ATLAS) and [75] (LHCb) for J/ψ, and from [76] for Υ (LHCb).

Quarkonium	$\sqrt{s}$ (GeV)	p_0 (GeV)	n	m
J/ψ	7000	4.2	19.2	3.5
Υ	7000	6.6	13.8	2.8
J/ψ	200	3.3	8.3	4.3
J/ψ	38.7	3.1	4.5	5.3

Table 5.5: Values of the parameters p_0, m, n defining the parametrization (5.79).

Due to the lack of RHIC data for double differential cross sections, to obtain the value of m we had to fix the value of n obtained from the fit of single differential cross section $d\sigma_{pp}^{J/\psi}/dy$. The RHIC data was extracted from [64].

Finally, the fit to the J/ψ E789 ($\sqrt{s} = 38.7$ GeV) data [77] was also performed by fixing the value of $n = 4.5$ obtained from fitting $d\sigma_{pp}^{J/\psi}/dx_F$ to the data (see Section 5.7).

The good agreement between LHC and RHIC J/ψ measurements and the parametrization (5.79) is shown in Figs. 5.25 and 5.26.

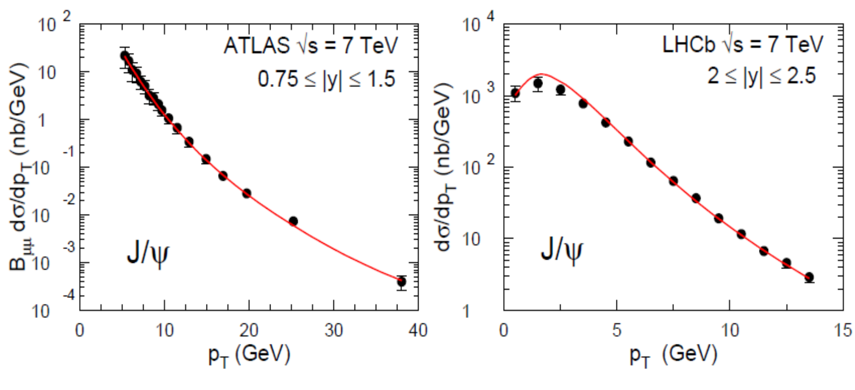

Figure 5.25: Comparison between the J/ψ cross section in $p-p$ collisions at the LHC and the parametrization (5.79) (solid red line).

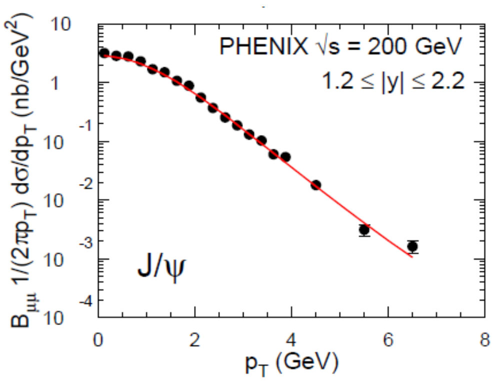

Figure 5.26: Comparison between the J/ψ cross section in $p-p$ collisions at RHIC and the parametrization (5.79) (solid red line).

5.8.4 Approximation for $R^{\psi}_{pA}(y, p_\perp)$

Using (5.74) and (5.79), the attenuation factor reads

$$R^{\psi}_{pA}(y, p_\perp) = \int_\varphi \int_\varepsilon \mathcal{P}(\varepsilon, E) \left[\frac{E}{E+\varepsilon}\right] \frac{\mu(|\vec{p}_\perp - \Delta\vec{p}_\perp|)}{\mu(p_\perp)} \frac{\nu(E+\varepsilon, \vec{p}_\perp - \Delta\vec{p}_\perp)}{\nu(E, p_\perp)} \tag{5.84}$$

Multiplying and dividing by $\nu(E+\varepsilon, p_\perp)$ one gets

$$R^{\psi}_{pA}(y, p_\perp) = \int_\varepsilon \mathcal{P}(\varepsilon, E) \left[\frac{E}{E+\varepsilon}\right] \frac{\nu(E+\varepsilon, p_\perp)}{\nu(E, p_\perp)} \int_\varphi \frac{\mu(|\vec{p}_\perp - \Delta\vec{p}_\perp|)}{\mu(p_\perp)} \frac{\nu(E+\varepsilon, \vec{p}_\perp - \Delta\vec{p}_\perp)}{\nu(E+\varepsilon, p_\perp)} \tag{5.85}$$

From Fig. 5.3, one can see that $\mathcal{P}(\varepsilon, E)$ is peaked at small values ε, thus we can neglect ε in the latter integral. In this approximation, the φ and ε integrals factorize

$$R^{\psi}_{pA}(y, p_\perp) \simeq R^{broad}_{pA}(y, p_\perp) \cdot R^{loss}_{pA}(y, p_\perp), \tag{5.86}$$

where

$$R^{broad}_{pA}(y, p_\perp) \equiv \int_\varphi \frac{\mu(|\vec{p}_\perp - \Delta\vec{p}_\perp|)}{\mu(p_\perp)} \frac{\nu(E, \vec{p}_\perp - \Delta\vec{p}_\perp)}{\nu(E, p_\perp)} \tag{5.87}$$

$$R^{loss}_{pA}(y, p_\perp) \equiv \int_\varepsilon \mathcal{P}(\varepsilon, E) \left[\frac{E}{E+\varepsilon}\right] \frac{\nu(E+\varepsilon, p_\perp)}{\nu(E, p_\perp)} \tag{5.88}$$

The factor $R^{broad}_{pA}(y, p_\perp)$ stands for nuclear modification due to the transverse momentum broadening only, which can be seen if we set $\mathcal{P}(\varepsilon, E) = \delta(\varepsilon)$ in (5.84). The factor R^{loss}_{pA} stands for the nuclear modification due to energy loss only, which can be obtained by setting $\Delta p_\perp = 0$ in (5.84). In our studies, we will use the factorized expression (5.86).

One should note that as in the case of the single cross section $d\sigma^{\psi}/dy$, the nuclear modification R^{ψ}_{pA} studied before can be recovered from (5.84), by performing the integration over $\vec{p}_{\perp}$. In this case, $\nu(y, p_{\perp})$ will be evaluated at a typical value $\bar{p}_{\perp}$. As a result the $p_{\perp}$-inclusive attenuation factor reads $R^{\psi}_{pA} \simeq R^{loss}_{pA}(y, \bar{p}_{\perp})$.

5.8.5 Comparison to data

E866

As was already mentioned, in E866 the J/ψ suppression was measured as a function of p_T for three domains of x_F. Due to the absorption effects appearing at small x_F, the model is compared to the E866 data [66] in the intermediate x_F ($0.2 \leq x_F \leq 0.6$, $< x_F >= 0.30$) and large x_F ($0.3 \leq x_F \leq 0.93$, $< x_F >= 0.48$) domains .

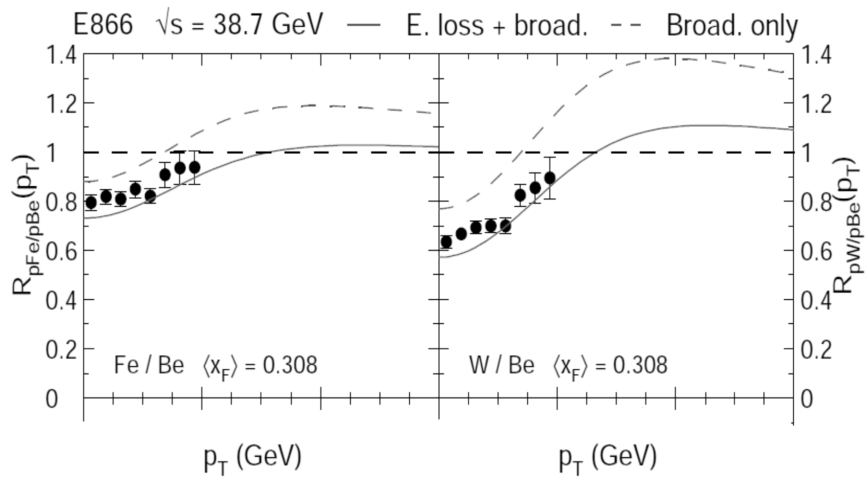

Figure 5.27: Model predictions (solid red curves) for the J/ψ nuclear suppression factor compared to E866 data for Fe/Be (left) and W/Be (right) collisions, in the intermediate x_F domain. The dashed lines indicate the effect of momentum broadening only, $R^{broad}_{pA}(p_{\perp})$.

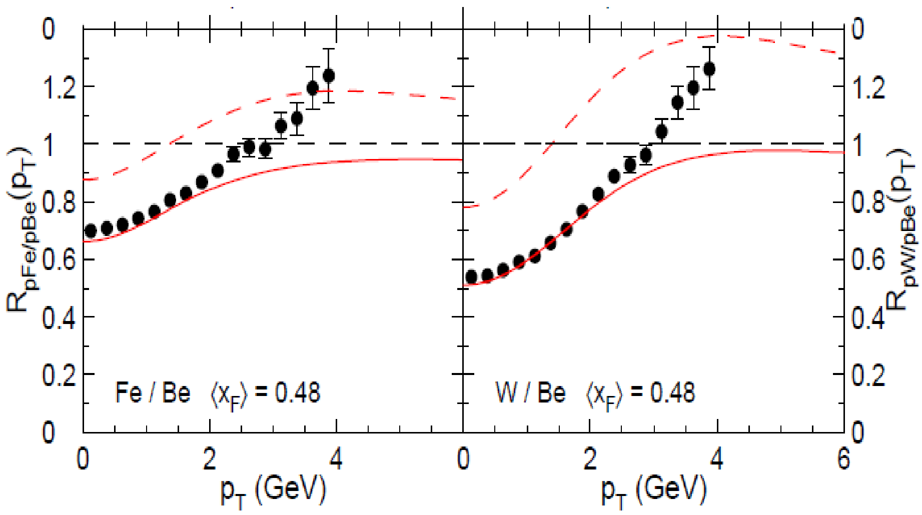

Figure 5.28: Model predictions (solid red curves) for the J/ψ nuclear suppression factor compared to E866 data for Fe/Be (left) and W/Be (right) collisions, in the large-x_F domain.

In Figs. 5.27 and 5.28, one can see the predictions obtained for J/ψ suppression in Fe/Be and W/Be, compared to the experimental data. The ratio $R_{pA}(p_T)$ increases in the whole range with a remarkable suppression at small p_T. The suppression in tungsten is stronger than in Fe (especially at large x_F). In Figs. 5.27 and 5.28 the predictions obtained with the broadening effect alone are shown by the dashed line. One can see that the factor $R_{pA}^{loss}(y, p_\perp)$ is essential to fix the magnitude of R_{pA}, which leads to the excellent agreement between data and the model predictions in the $0 \le p_\perp \le 2$ GeV range. One observes a disagreement between our model and the experimental data at $p_\perp \gtrsim 3$ GeV. As a possible explanation, one can think of the $p-p$ parametrization which was extracted from the data at $x_F = 0$, and which might be no longer appropriate to describe the cross section at large x_F. Putting aside the latter region of large $p_\perp$ and x_F, our model reproduces remarkably the $p_\perp$-dependence of J/ψ suppression. Thus, the same quantity $\hat{q}L$ can equally well describe both energy loss and nuclear broadening effects.

RHIC

Let us do the comparison at higher energies. One can use the data obtained recently from RHIC experiment [78] for backward ($-2.2 \le y \le -1.2$), central ($|y| \le 0.35$) and forward ($1.2 \le y \le 2.2$) rapidities. The predictions of our model were done at $y = -1.7$, 0, $+1.7$ respectively. The comparison between data and our model can be seen in Fig. 5.29.

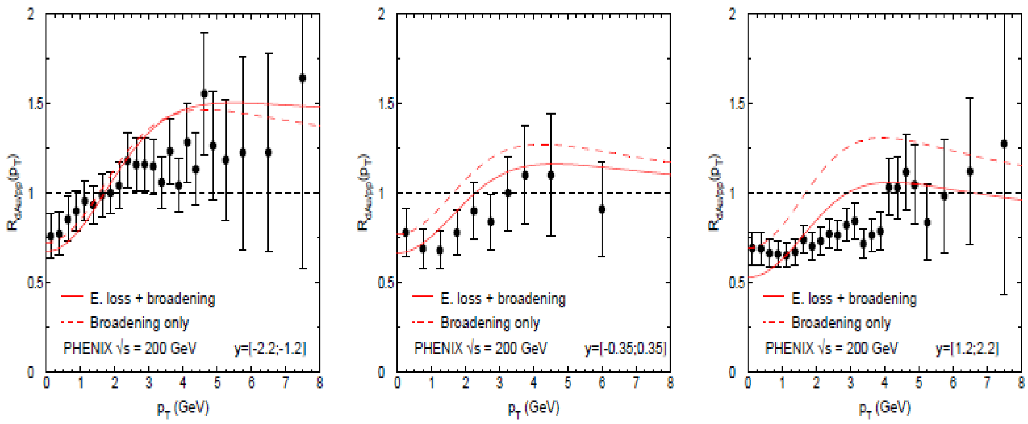

Figure 5.29: Model predictions (solid red curves) for the J/ψ nuclear suppression factor compared to RHIC at backward (left), mid (central) and forward rapidities (right).

As one can see, the model reproduces the increase with $p_\perp$ observed in data. At backward and mid-rapidities, around the values $p_\perp \simeq 4 - 5$ GeV, one obtains $R_{pA}(p_\perp) > 1$. At forward rapidities the suppression due to energy loss is too strong to observe such increase. The curves for R_{pA} obtained from p_T-broadening alone are shown by dashed lines.

Predictions for LHC

Here we present predictions for J/ψ and Υ nuclear production ratios R_{pA} as a function of p_T for LHC energies ($\sqrt{s} = 5$ TeV), for different rapidities ($y = -3.7, 0, 2.8$). In Fig. 5.30 one can see the predictions for J/ψ. A suppression is predicted at $p_T \lesssim 3$ GeV.

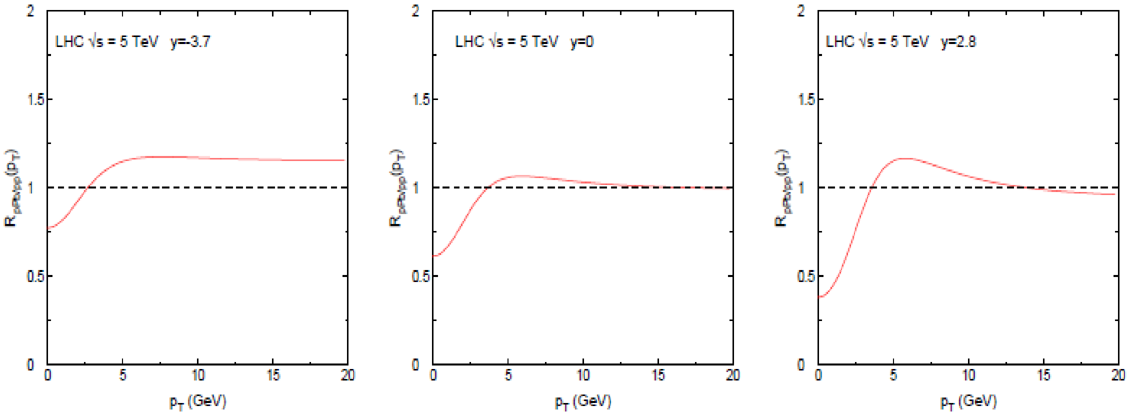

Figure 5.30: Model predictions for the J/ψ nuclear suppression factor for $p-Pb$ collisions at LHC.

The predictions for Υ channel are shown in Fig. 5.31.

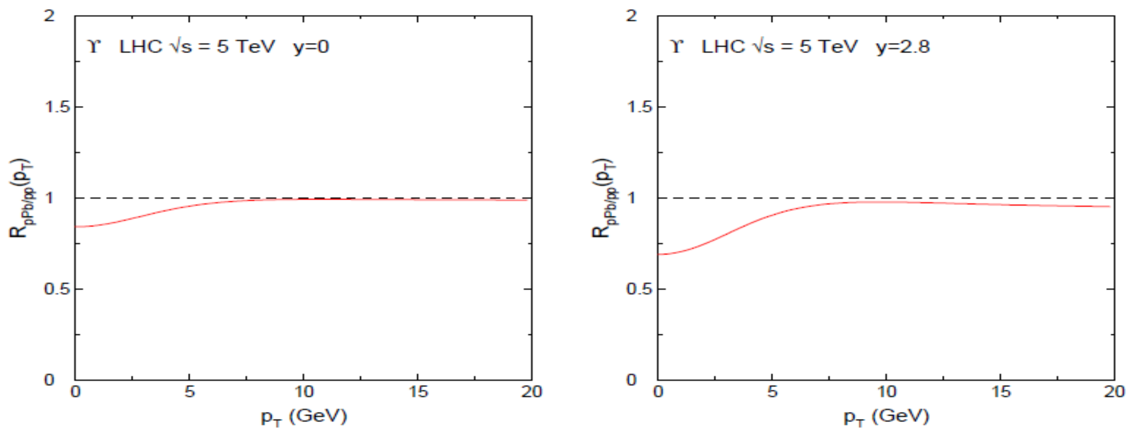

Figure 5.31: Predictions for the Υ nuclear suppression factor $R_{pA}(p_\perp)$ in $p-Pb$ collisions at LHC, for central (left) and forward (right) rapidities.

Due to the mass dependence of the energy loss ($\Delta E \sim M^{-1}$), the suppression for Υ due to ΔE is milder than for J/ψ. "Cronin peak" is less apparent for Υ data for J/ψ, due to the flatter $p_\perp$ spectrum.

Υ suppression $R_{pA}^{\Upsilon} < 1$ is predicted in the range $0 \leq p_\perp \leq 6$ GeV at mid-rapidity, the wider range being due to the value of the p_0 parameter appearing in the $p-p$ cross section, which is $p_0 \simeq 6.6$GeV for Υ and $p_0 \simeq 4.2$GeV for J/ψ, see Table 5.8.3. The maximal suppression observed at $p_\perp = 0$ is $R_{pA}^{\Upsilon} \simeq 0.85$ for $y = 0$ and $R_{pA}^{\Upsilon} \simeq 0.65$ for $y = 2.8$.

The predictions of our model have been compared recently to the LHC data, see Fig. 5.32. Even though our curve shows a steeper suppression at small p_T, the qualitative trend of the data is well reproduced by the model including p_T-broadening and energy loss.

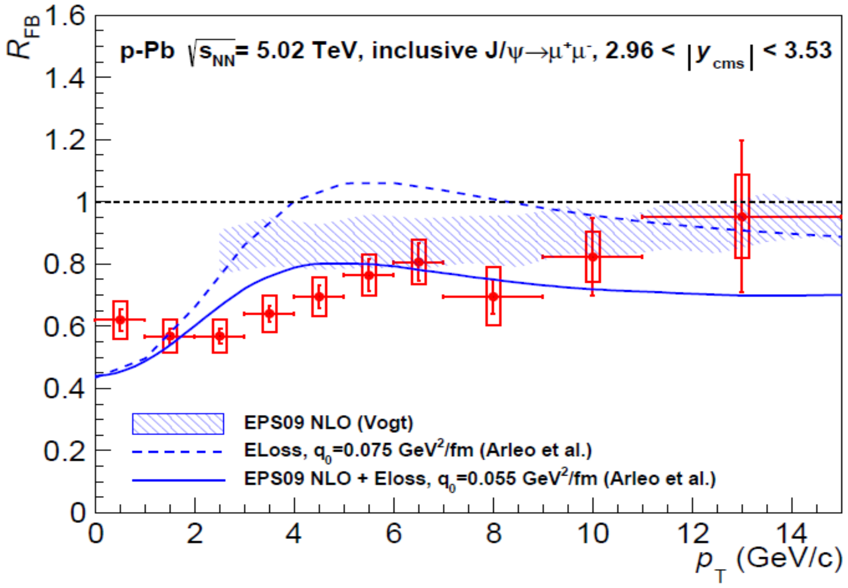

Figure 5.32: The forward to backward ration R_{FB} of the nuclear modification factor for inclusive J/ψ production, as a function of p_T, compared to theoretical models. The energy loss model is shown by the dashed blue line [69].

Conclusion

The observed quarkonium nuclear suppression in p-A collisions has triggered much interest in the last two decades. Various effects, such as shadowing, nuclear absorption, parton energy loss, have been proposed as possible explanations of this phenomenon. However, until today there was no consensus on what could be the dominant effect. The results obtained during my study strongly support parton energy loss as the dominant effect responsible for J/ψ (and Υ) nuclear suppression in cold nuclear matter.

In the first part of Chapter 5 we considered the x_F dependence of J/ψ nuclear suppression. Parton energy loss was implemented by simply expressing the cross section in p-A collisions as the one in p-p, with a shift in x_F to take into account parton energy loss through the nucleus. Since the precise J/ψ production mechanism is not known, one extracts the J/ψ p-p cross section from the experiment. The only free parameter of the model $\hat{q}_0$ is extracted by comparing the model predictions to the E866 data for J/ψ suppression in p-W as compared to p-Be. The obtained value $\hat{q}_0 = 0.075 \pm 0.005 \mathrm{GeV}^2/\mathrm{fm}$ is consistent with current estimates of the rate (per unit length) of transverse momentum broadening in cold nuclear matter.

The predictions of the model are then compared to the experimental data for various nuclei and various collision energies. The good agreement obtained at intermediate energies (E866, NA60, HERA-B), as well as at high energies (RHIC, LHC), supports the validity of the model. Some disagreement is seen when x_F is below some critical value, corresponding to J/ψ hadronization in the nucleus. As mentioned in Chapter 3, in this region the parton energy loss model is not expected to fully apply, since the effect of J/ψ nuclear absorption (or dissociation), might play a role there. To check the mass dependence of the model it was applied to Υ suppression. The model predictions were compared to the E772 and RHIC Υ data. Despite the limited amount of Υ data, the obtained agreement suggests a correct mass dependence of the implemented parton energy loss. Finally, the predictions for both J/ψ and Υ suppression were made for p-Pb collisions at the LHC. Those predictions appear to be in very good agreement with recently published LHC data.

In the second part of Chapter 5, the parton energy loss model was generalized to address the p_T dependence of J/ψ nuclear suppression. This was done by expressing the J/ψ double differential cross section in p-A as the one in p-p, with a double shift: a shift in E, accounting for the energy loss and a shift in p_T, accounting for the transverse momentum broadening $\Delta\vec{p}_T$ suffered by the $c\bar{c}$ pair through the nucleus. Since the value of $\hat{q}_0$ was fixed previously, this version of the model introduces no additional parameter. The double differential p-p cross section is extracted from experiment. Due to the specific shape of the parametrization used for the latter cross section, the expression of the nuclear modification factor factorizes (to a good approximation) into the product of factors accounting respectively for the nuclear broadening and energy loss effects,

$$R_{pA}^{\psi}(y,p_\perp) \simeq R_{pA}^{broad}(y,p_\perp) \cdot R_{pA}^{loss}(y,p_\perp)\,. \tag{5.89}$$

The model was first compared to the E866 data for the p_T dependence of nuclear suppression. The curves presented in Chapter 5 show that the p_T-shape of R_{pA}, in particular the Cronin effect, is well reproduced by the factor $\simeq R_{pA}^{broad}$, whereas the factor R_{pA}^{loss} is essential to fix the magnitude of R_{pA}. An excellent agreement between data and the model is found in the $0 \leq p_\perp \leq 2$ GeV range. Model predictions at RHIC energies were also made and showed a satisfactory agreement. The predictions for the expected p_T dependence of J/ψ and Υ suppression at the LHC, and the preliminary LHC data were presented in the end of Chapter 5.

The very good qualitative and quantitative description, within a consistent framework taking into account the sole effect of parton energy loss, of both the rapidity and transverse momentum dependence of quarkonium suppression at various collision energies, supports parton energy loss as the dominant effect (at large enough x_F) in quarkonium suppression in p-A collisions. This stresses the importance of implementing parton energy loss in cold nuclear matter also in A-A collisions, in order to disentangle truly hot effects when interpreting jet-quenching as a quark-gluon plasma signature.

Appendix A

Appendix A

A.1 Derivation of the Gunion-Bertsch amplitude

To derive the Gunion-Bertsch spectrum, we first start by deriving the elastic scattering amplitude shown in Fig. A.1.

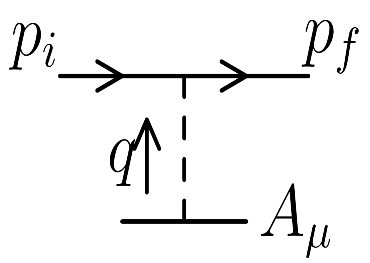

Figure A.1: Elastic scattering of an electron without a radiation.

The whole derivation will be done in the light-cone variables, which are defined as,

$$p^{\pm} = \frac{p^0 \pm p^z}{\sqrt{2}} \tag{A.1}$$

Consequently the 4-vector will be expressed through those new coordinates as

$$p = (p^+, p^-, \vec{p}_\perp); \quad p^{0,z} = \frac{p^+ \pm p^-}{\sqrt{2}} \tag{A.2}$$

The following equalities will be needed in the further calculations:

$$p^2 = 2p^+p^- - p_\perp^2 \tag{A.3}$$

$$p \cdot p' = p^+ p'^- + p^- p'^+ - \vec{p}_\perp \vec{p}'_\perp \tag{A.4}$$

The amplitude for the elastic scattering of scalar quarks is,

$$iM_{el} = ig(p_i + p_f)^\mu A_\mu t^{a1} \tag{A.5}$$

Since we are interested in high energies, we will select a dominant terms in $p_i \to \infty$. We will fix $q^+ = 0$. Then the (A.5) can be written as,

$$M_{el} \simeq g(p_i + p_f)^+ A^- t^{a1} = g(2p_i^+) A^- t^{a1} \tag{A.6}$$

Further we will be interested in terms with A^-, since only this component of A_μ matters.

Now let us consider the main process with a radiation. All contributing diagrams can be see on the Fig. A.2.

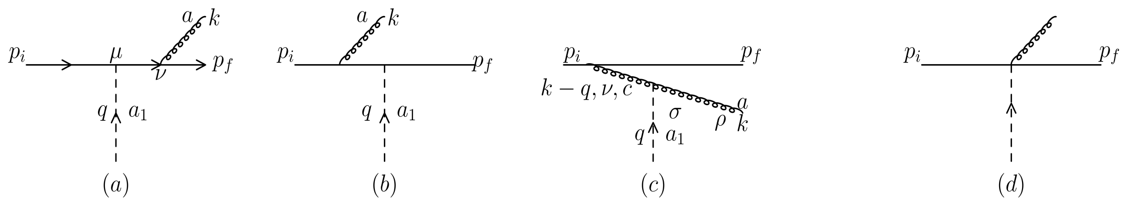

Figure A.2: Elastic scattering and associated radiation.

The momenta of incoming, outgoing quarks and radiating gluon is defined as

$$p_i = \left(p^+, \frac{M^2+Q^2}{2p^+}, \vec{0}_\perp\right) \tag{A.7}$$

$$p_f = \left((1-x)p^+, \frac{(\vec{q}-\vec{k})_\perp^2 + M^2}{2(1-x)p^+}, \vec{q}_\perp - \vec{k}_\perp\right) \tag{A.8}$$

$$k = \left(xp^+, \frac{\vec{k}_\perp^2}{2xp^+}, \vec{k}_\perp\right) \tag{A.9}$$

$$q = \left(0, q^-, \vec{q}_\perp\right); \quad q^- = p_f^- + k^- - p_i^- \tag{A.10}$$

Using (A.7), (A.8), (A.9) and (A.10) we find for q^-

$$q^- = \frac{\vec{k}^2 + x(\vec{q}^2 - 2\vec{k}\vec{q}) + x^2M^2}{2x(1-x)p^+} \tag{A.11}$$

In the following, we will use the light-cone gauge $A^+ = n \cdot A = 0$, where $n = (0, 1, \vec{0}_\perp)$. In this gauge, the propagator is

$$D_{\mu\nu} = -i\frac{d_{\mu\nu}(k)}{k^2 + i\varepsilon}; \quad d_{\mu\nu}(k) = g_{\mu\nu} - \frac{k_\mu n_\nu + k_\nu k_\mu}{k^+}, \tag{A.12}$$

and gluon polarization is

$$\varepsilon = \left(0, \frac{\vec{\varepsilon}\cdot\vec{k}}{xp^+}, \vec{\varepsilon}\right). \tag{A.13}$$

For any 4-vector p, the following property is satisfied:

$$p^\mu d_{\mu\nu}(k) n^\nu = p^\mu \left(g_{\mu\nu} - \frac{k_\mu n_\nu + k_\nu k_\mu}{k^+} \right) n^\nu = (p \cdot n) - p^+ = 0 \tag{A.14}$$

Meaning that, $p^\mu d_\nu(k)$ has no $+$ component.

Now we can now, using Feynman rules of (A.5), go back to Fig. A.2 and write analytical expressions for each of the amplitudes:

$$\begin{aligned} iM_a &= ig(2p_f + k)^\nu ig(2p_i + q)^\mu \frac{i}{(p_f + k)^2 - M^2} \varepsilon_\nu A_\mu t^a t^{a1} = \\ &= -ig^2 t^a t^{a1} \frac{(2p_f + k) \cdot \varepsilon (2p + q) \cdot A}{2p_f k} = -ig^2 \frac{\varepsilon p_f}{k p_f} 2p_i^+ A^- t^a t^{a1} \end{aligned} \tag{A.15}$$

For the diagram (b) the expression is derived in the similar way,

$$iM_b = ig^2 \frac{\varepsilon p_i}{k p_i} 2p_f^+ A^- t^{a1} t^a \tag{A.16}$$

For the (d) diagram we have

$$iM_d \propto g^2 g^{\mu\nu} \varepsilon_\nu A_\mu = g^2 (-\vec{\varepsilon} \vec{A}_\perp) \tag{A.17}$$

$(-\vec{\varepsilon} \vec{A}_\perp)$ is negligible, since at high energies we are interested in terms with p^+ and A^-. For the (c) diagram we use 3-gluon vertex rule:

$$\begin{aligned} iM_c &= ig(p_i + p_f)^\mu \frac{-i}{(p_i - p_f)^2} d_{\mu\nu}(k - q) igif_{a_1 ac} t^c \\ &\cdot \left[(2k - q)^\sigma g^{\nu\rho} + (2q - k)^\rho g^{\nu\sigma} + (-q - k)^\nu g^{\rho\sigma} \right] A_\sigma \varepsilon_\rho \\ &= ig^2 f_{a_1 ac} t^c \frac{(2k^+) A^-}{(p_i - p_f)^2} (p_i + p_f)^\mu \left(g_{\mu\nu} - \frac{(k - q)_\mu n_\nu + (k - q)_\nu n_\mu}{k^+} \right) \varepsilon^\nu \end{aligned} \tag{A.18}$$

In the latter, we used the fact, that the dominant contribution comes from the first term of the 3-gluon vertex. After simplification, (A.18) results into:

$$M_c = g^2 f_{a_1 ac} t^c \frac{2\vec{\varepsilon}(\vec{k} - \vec{q})}{(p_i - p_f)^2} (2p_i^+) A^- \tag{A.19}$$

The sum of (A.15), (A.16) and (A.19) will lead to,

$$M_a + M_b + M_c = -g^2 (2p_i^+) A^- \left\{ t^a t^{a1} \frac{\varepsilon p_f}{k p_f} - t^{a_1} t^a (1 - x) \frac{\varepsilon p_i}{k p_i} - [t^{a1}, t^a] \frac{2\vec{\varepsilon}(\vec{k} - \vec{q})}{(p_i - p_f)^2} \right\} \tag{A.20}$$

To calculate explicitly (A.20) we need to know the expressions of 4-products (this can be done easily using the definitions given by (A.7), (A.8), (A.9), (A.10)):

$$\varepsilon \cdot p_i = p_i^+ \frac{\vec{\varepsilon}\vec{k}}{x p_i^+} = \frac{\vec{\varepsilon}\vec{k}}{x} \tag{A.21}$$

$$k \cdot p_i = \frac{k_\perp^2}{2x} + x\frac{M^2}{2} = \frac{\vec{k}^2 + x^2 M^2}{2x} \tag{A.22}$$

$$\varepsilon \cdot p_f = \frac{\vec{\varepsilon}\vec{k}}{x p^+}(1-x)p^+ - \vec{\varepsilon}(\vec{q}-\vec{k}) = \frac{\varepsilon(\vec{k}-x\vec{q})}{x} \tag{A.23}$$

$$k \cdot p_f = \frac{(1-x)k_\perp^2}{2x} + \frac{x((\vec{q}-\vec{k})^2 + M^2)}{2(1-x)} - \vec{k}^2(\vec{q}-\vec{k}) = \frac{(\vec{k}-x\vec{q})^2 + x^2M^2}{2x(1-x)} \tag{A.24}$$

$$(p_i - p_f)^2 = -\frac{(\vec{q}-\vec{k})^2 + x^2M^2}{1-x} \tag{A.25}$$

Thus the sum (A.20) turns into

$$\begin{aligned} M &= -g^2(2p_i^+)A^- 2(1-x)\cdot \\ &\cdot \left\{ t^a t^{a_1} \frac{\vec{\varepsilon}(\vec{k}-x\vec{q})}{(\vec{k}-x\vec{q})^2 + x^2M^2} - t^{a1}t^a \frac{\vec{\varepsilon}\vec{k}}{\vec{k}^2 + x^2M^2} + [t^{a1}, t^a] \frac{\vec{\varepsilon}(\vec{k}-\vec{q})}{(\vec{q}-\vec{k})^2 + x^2M^2} \right\} \\ &\overset{x\to 0}{\propto} [t^{a_1}, t^a]\vec{\varepsilon}\left[\frac{\vec{k}}{k^2} - \frac{\vec{k}-\vec{q}}{(\vec{q}-\vec{k})^2} \right] \end{aligned} \tag{A.26}$$

Bibliography

[1] W. Heisenberg, Z. Phys. **77** (1932) 1.

[2] C. -N. Yang and R. L. Mills, Phys. Rev. **96**, 191 (1954). (Cited on page 5.)

[3] O. W. Greenberg, Phys. Rev. **139**, B1038 (1965). (Cited on page 5.)

[4] W. Buchmuller and S. H. H. Tye, Phys. Rev. D **24**, 132 (1981). (Cited on page 6.)

[5] Y. L. Dokshitzer, In *Jerusalem 1997, High energy physics* 47-67 [hep-ph/9801372].

[6] Michael E. Peskin, Daniel V. Schroeder, An Introduction to Quantum Field Theory. (Cited on page 7.)

[7]

[7] J. S. Poucher, M. Breidenbach, W. R. Ditzler, J. I. Friedman, H. W. Kendall, E. D. Bloom, R. L. Cottrell and D. H. Coward *et al.*, Phys. Rev. Lett. **32**, 118 (1974). (Cited on page 8.)

[8] J. C. Collins, D. E. Soper and G. F. Sterman, Adv. Ser. Direct. High Energy Phys. **5** (1988) 1 [hep-ph/0409313]. (Cited on pages 10, 13 and 16.)

[9] R. D. Pisarski, PoS LATTICE **2008**, 016 (2008) [arXiv:0810.4585 [hep-ph]]. (Cited on pages 11 and 133.)

(Cited on page 12.)

[10] G. T. Bodwin, Int. J. Mod. Phys. Conf. Ser. **02**, 9 (2011) [arXiv:1012.4215 [hep-ph]]. (Cited on pages 29, 30 and 31.)

(Cited on page 13.)

[11] G. C. Nayak, J. -W. Qiu and G. F. Sterman, Phys. Rev. D **72**, 114012 (2005) [hep-ph/0509021]. (Cited on page 13.)

[12] J. C. Collins, D. E. Soper and G. F. Sterman, Nucl. Phys. B **263**, 37 (1986). (Cited on page 15.)

[13] G. Altarelli and G. Parisi, Nucl. Phys. B **126**, 298 (1977). (Cited on page 17.)

[14] Y. L. Dokshitzer, Sov. Phys. JETP **46**, 641 (1977) [Zh. Eksp. Teor. Fiz. **73**, 1216 (1977)]. (Cited on page 17.)

[15] R. Brock *et al.* [CTEQ Collaboration], (Cited on page 17.)

[16] G. Miller, E. D. Bloom, G. Buschhorn, D. H. Coward, H. C. DeStaebler, J. Drees, C. L. Jordan and L. W. Mo *et al.*, Phys. Rev. D **5**, 528 (1972). (Cited on page 18.)

[17] R. K. Ellis, W. J. Sterling and B. R. Weber, QCD and Collider Physics, (Cited on pages 18, 22, 23, 24 and 25.)

[18] W. H. Smith, P. H. Sandler, F. S. Merritt, M. J. Oreglia, B. A. Schumm, C. Arroyo, K. T. Bachmann and R. E. Blair *et al.*, Nucl. Phys. Proc. Suppl. **19**, 281 (1991). (Cited on page 19.)

[19] S. L. Wu, Phys. Rept. **107**, 59 (1984). (Cited on pages 19 and 20.)

[20] P. L. McGaughey, J. M. Moss and J. C. Peng, Ann. Rev. Nucl. Part. Sci. **49**, 217 (1999) [hep-ph/9905409]. (Cited on page 21.)

[21] C. N. Brown, W. E. Cooper, D. Finley, Y. B. Hsiung, A. M. Jonckheere, H. Jostlein, D. M. Kaplan and L. M. Lederman *et al.*, Phys. Rev. Lett. **63**, 2637 (1989). (Cited on page 22.)

[22] R. S. Bhalerao and R. V. Gavai, arXiv:0812.1619 [hep-ph]. (Cited on pages 23, 28 and 33.)

[23] A. Bazavov, T. Bhattacharya, M. Cheng, N. H. Christ, C. DeTar, S. Ejiri, S. Gottlieb and R. Gupta *et al.*, Phys. Rev. D **80**, 014504 (2009) [arXiv:0903.4379 [hep-lat]]. (Cited on page 27.)

[24] J. D. Bjorken, Phys. Rev. D **27**, 140 (1983). (Cited on page 27.)

[25] B. Muller, J. Schukraft and B. Wyslouch, Ann. Rev. Nucl. Part. Sci. **62**, 361 (2012) [arXiv:1202.3233 [hep-ex]]. (Cited on page 32.)

[26] T. Matsui and H. Satz, Phys. Lett. B **178**, 416 (1986). (Cited on page 33.)

[27] J. J. Aubert *et al.* [E598 Collaboration], Phys. Rev. Lett. **33**, 1404 (1974). (Cited on page 35.)

[28] J. E. Augustin *et al.* [SLAC-SP-017 Collaboration], Phys. Rev. Lett. **33**, 1406 (1974). (Cited on page 35.)

[29] J. F. Amundson, O. J. P. Eboli, E. M. Gregores and F. Halzen, Phys. Lett. B **390**, 323 (1997) [hep-ph/9605295]. (Cited on page 36.)

[30] P. L. Frabetti *et al.* [E687 Collaboration], Phys. Lett. B **316**, 197 (1993). (Cited on pages 38 and 39.)

[31] M. I. Adamovich *et al.* [Photon Emulsion Collaboration], Phys. Lett. B **187**, 437 (1987). (Cited on page 39.)

[32] A. Bamberger *et al.* [Annecy(LAPP)-Brussels-Freiburg Collaboration], Nucl. Phys. B **134**, 1 (1978). (Cited on pages 38 and 39.)

[33] H. Cobbaert, P. R. Hobson, R. Arnold, J. L. Bailly, J. F. Balland, M. Barth, J. H. Bartley and M. Boratav *et al.*, Z. Phys. C **36**, 577 (1987). (Cited on page 39.)

[34] R. Baier and R. Ruckl, Z. Phys. C **19**, 251 (1983). (Cited on page 40.)

[35] J. P. Lansberg, Int. J. Mod. Phys. A **21**, 3857 (2006) [hep-ph/0602091]. (Cited on pages 42, 43 and 45.)

[36] P. Artoisenet, J. M. Campbell, J. P. Lansberg, F. Maltoni and F. Tramontano, Phys. Rev. Lett. **101**, 152001 (2008) [arXiv:0806.3282 [hep-ph]]. (Cited on page 43.)

[37] M. Kramer, 1, Prog. Part. Nucl. Phys. **47**, 141 (2001) [hep-ph/0106120]. (Cited on pages 46 and 47.)

[38] B. Gong, J. -P. Lansberg, C. Lorce and J. Wang, JHEP **1303**, 115 (2013) [arXiv:1210.2430 [hep-ph]]. (Cited on page 48.)

[39] G. C. Nayak, J. -W. Qiu and G. F. Sterman, Phys. Lett. B **613**, 45 (2005) [hep-ph/0501235]. (Cited on page 48.)

[40] J. Badier *et al.* [NA3 Collaboration], Z. Phys. C **20**, 101 (1983). (Cited on pages 50, 51, 100, 101, 102 and 109.)

[41] M. J. Leitch *et al.* [FNAL E866/NuSea Collaboration], Phys. Rev. Lett. **84**, 3256 (2000) [nucl-ex/9909007]. (Cited on pages 51, 52, 107, 108, 109, 116 and 122.)

[42] A. Adare *et al.* [PHENIX Collaboration], Phys. Rev. C **77**, 024912 (2008) [Erratum-ibid. C **79**, 059901 (2009)] [arXiv:0711.3917 [nucl-ex], arXiv:0903.4845 [nucl-ex]]. (Cited on page 53.)

[43] A. Adare *et al.* [PHENIX Collaboration], Phys. Rev. Lett. **107**, 142301 (2011) [arXiv:1010.1246 [nucl-ex]]. (Cited on pages 53 and 111.)

[44] R. Vogt, Phys. Rev. C **61**, 035203 (2000) [hep-ph/9907317]. (Cited on pages 56, 57, 60, 61 and 62.)

[45] N. Armesto, J. Phys. G **32**, R367 (2006) [hep-ph/0604108]. (Cited on page 58.)

[46] W. Q. Chao, C. S. Gao and Y. B. He, Commun. Theor. Phys. **25**, 479 (1996) [hep-ph/9504290]. (Cited on page 62.)

[47] J. -w. Qiu, J. P. Vary and X. -f. Zhang, Phys. Rev. Lett. **88**, 232301 (2002) [hep-ph/9809442]. (Cited on page 63.)

[48] S. Gavin and J. Milana, Phys. Rev. Lett. **68**, 1834 (1992). (Cited on pages 63 and 64.)

[49] S. J. Brodsky and P. Hoyer, Phys. Lett. B **298**, 165 (1993) [hep-ph/9210262]. (Cited on pages 64 and 66.)

[50] Yu. L. Dokshitzer, Perturbative QCD for beginners. (Cited on pages 68 and 74.)

[51] S. Peigne and A. V. Smilga, Phys. Usp. **52**, 659 (2009) [Usp. Fiz. Nauk **179**, 697 (2009)] [arXiv:0810.5702 [hep-ph]]. (Cited on pages 67, 76 and 77.)

[52] F. Arleo, S. Peigne and T. Sami, Phys. Rev. D **83**, 114036 (2011) [arXiv:1006.0818 [hep-ph]]. (Cited on pages 72, 73, 76 and 79.)

[53] F. Arleo and S. Peigne, JHEP **1303**, 122 (2013) [arXiv:1212.0434 [hep-ph]]. (Cited on pages 82, 86, 108 and 114.)

[54] J. F. Gunion and G. Bertsch, Phys. Rev. D **25**, 746 (1982). (Cited on page 82.)

[55] R. Baier, Y. L. Dokshitzer, A. H. Mueller, S. Peigne and D. Schiff, Nucl. Phys. B **484**, 265 (1997) [hep-ph/9608322]. (Cited on pages 86 and 87.)

[56] F. Arleo, R. Kolevatov, S. Peigne and M. Rustamova, JHEP **1305**, 155 (2013) [arXiv:1304.0901 [hep-ph]]. (Cited on page 89.)

[57] H. De Vries, C. W. De Jager and C. De Vries, Atom. Data Nucl. Data Tabl. **36** (1987) 495. (Cited on page 106.)

[58] R. Baier, Y. L. Dokshitzer, A. H. Mueller and D. Schiff, JHEP **0109**, 033 (2001) [hep-ph/0106347]. (Cited on page 94.)

[59] L. Landau, J. Phys. (USSR) **8**, 201 (1944). (Cited on page 95.)

[60] J. Badier *et al.* [NA3 Collaboration], Z. Phys. C **20**, 101 (1983). (Cited on pages 50, 51, 100, 101, 102 and 109.)

[61] M. S. Kowitt, G. Gidal, P. M. Ho, K. B. Luk, D. Pripstein, L. D. Isenhower, M. E. Sadler and R. Schnathorst *et al.*, Phys. Rev. Lett. **72**, 1318 (1994). (Cited on page 100.)

[62] I. Abt *et al.* [HERA-B Collaboration], Eur. Phys. J. C **60**, 525 (2009) [arXiv:0812.0734 [hep-ex]]. (Cited on pages 100 and 110.)

[63] K. Aamodt *et al.* [ALICE Collaboration], Phys. Lett. B **704**, 442 (2011) [Erratum-ibid. B **718**, 692 (2012)] [arXiv:1105.0380 [hep-ex]]. (Cited on pages 100, 101 and 119.)

[64] A. Adare *et al.* [PHENIX Collaboration], Phys. Rev. Lett. **98**, 232002 (2007) [hep-ex/0611020]. (Cited on pages 100, 101 and 120.)

[65] M. L. Miller, K. Reygers, S. J. Sanders and P. Steinberg, Ann. Rev. Nucl. Part. Sci. **57**, 205 (2007) [nucl-ex/0701025]. (Cited on pages 103 and 104.)

[66] M. J. Leitch *et al.* [FNAL E866/NuSea Collaboration], Phys. Rev. Lett. **84**, 3256 (2000) [nucl-ex/9909007]. (Cited on pages 51, 52, 107, 108, 109, 116 and 122.)

[67] F. Arleo and S. Peigne, JHEP **1303**, 122 (2013) [arXiv:1212.0434 [hep-ph]]. (Cited on pages 82, 86, 108 and 114.)

[68] A. Adare *et al.* [PHENIX Collaboration], Phys. Rev. Lett. **107**, 142301 (2011) [arXiv:1010.1246 [nucl-ex]]. (Cited on pages 53 and 111.)

[69] B. B. Abelev *et al.* [ALICE Collaboration], arXiv:1308.6726 [nucl-ex]. (Cited on pages 112 and 126.)

[70] D. M. Alde, H. W. Baer, T. A. Carey, G. T. Garvey, A. Klein, C. Lee, M. J. Leitch and J. W. Lillberg *et al.*, Phys. Rev. Lett. **66**, 2285 (1991). (Cited on page 113.)

[71] A. Adare *et al.* [PHENIX Collaboration], Phys. Rev. Lett. **109**, 242301 (2012) [arXiv:1211.4017 [nucl-ex]]. (Cited on page 113.)

[72] R. Reed [STAR Collaboration], J. Phys. Conf. Ser. **270**, 012026 (2011) [Nucl. Phys. A **855**, 440 (2011)]. (Cited on page 113.)

[73] A. Accardi, hep-ph/0212148. (Cited on page 115.)

[74] G. Aad *et al.* [ATLAS Collaboration], Nucl. Phys. B **850**, 387 (2011) [arXiv:1104.3038 [hep-ex]]. (Cited on page 119.)

[75] R. Aaij *et al.* [LHCb Collaboration], Eur. Phys. J. C **71**, 1645 (2011) [arXiv:1103.0423 [hep-ex]]. (Cited on page 119.)

[76] RAaij *et al.* [LHCb Collaboration], Eur. Phys. J. C **72**, 2025 (2012) [arXiv:1202.6579 [hep-ex]]. (Cited on page 119.)

[77] M. H. Schub *et al.* [E789 Collaboration], Phys. Rev. D **52**, 1307 (1995) [Erratum-ibid. D **53**, 570 (1996)]. (Cited on page 120.)

[78] A. Adare, S. Afanasiev, C. Aidala, N. N. Ajitanand, Y. Akiba, H. Al-Bataineh, J. Alexander and A. Angerami *et al.*, arXiv:1204.0777 [nucl-ex]. (Cited on page 123.)